5-3-2016

The Impacts of Surface Conditions on Sea Breezes over Coastal Connecticut

Eric Zachary Sinsky
eric.sinsky@gmail.com

The Impacts of Surface Conditions on Sea Breezes over Coastal Connecticut

Eric Zachary Sinsky

B.S., Rutgers University, 2014

A Thesis

Submitted in Partial Fulfillment of the

Requirements for the Degree of

Master of Science

At the

University of Connecticut

2016

APPROVAL PAGE

Masters of Science Thesis

The Impacts of Surface Conditions on Sea Breezes over Coastal Connecticut

Presented by

Eric Sinsky, B.S.

Major Advisor_____

Kelly Lombardo

Associate Advisor_____

James Edson

Associate Advisor_____

Michael Whitney

University of Connecticut

2016

Acknowledgements

I would like to thank all those who have contributed to my thesis. Many thanks to my committee for guiding me through my work; major advisor Dr. Kelly Lombardo, associate advisor Dr. James Edson and associate advisor Dr. Michael Whitney. Thanks goes to Mr. Yan Jia for providing the NARR initial condition modification procedure and Dr. Aaron Paget for providing a procedure that removes unwanted radar noise from the composite radar images. Thanks goes to Mr. Todd Fake for providing technical support for the numerical model simulations. This research was sponsored by NASA ROSES (2011) Grant NNX13AE25G.

Table of Contents

Abstract

Sea breezes are mesoscale atmospheric coastal circulations that develop in response to diurnal variations in the land-sea thermal gradient resulting in cooler air temperatures in coastal regions. Accurate numerical model hindcasts and forecasts of sea breezes, used to study and predict these circulations, are important for a variety of communities beyond the atmospheric sciences. For example, sea breezes can influence marine processes such as oceanic upwelling, estuarine circulation, and air-sea fluxes, as well as impact the energy, aviation, and air quality industries. Representations of the coastline and sea surface temperature (SST) in the numerical model can influence simulated sea breezes. In this study, a series of sensitivity experiments are performed to highlight the impact of the horizontal resolution of the numerical coastline and SST on simulated sea breeze dynamics.

The 21 August 2013 and 08 July 2013 coastal CT sea breeze events are simulated using the Weather and Research Forecasting (WRF) model, initialized with the 32 km North American Regional Reanalysis (NARR) for atmospheric conditions. Coastline sensitivity experiments compare simulated sea breeze circulations using a coastline resolved at 32 km (O(NARR)) and 1 km (O(WRF)). Sea surface temperature sensitivity experiments compare a spatially uniform SST (22˚C), NARR (32 km) spatially varying SST, and the G1SST (1km) spatially varying SST.

Coastline sensitivity experiments illustrate the use of a relatively coarse representation of the coastal geography results in the mischaracterization of western Long Island Sound as land, resulting in an inaccurate land-sea temperature gradient and thus an inaccurate sea breeze circulation. Sea breeze circulations are less sensitive to the resolution of the offshore SST, though the inland propagation distance of the sea breeze front varies among the sensitivity experiments. While the surface fluxes respond to the varying SST products, the impact on the overlying air temperature is confined to the lowest 100 m of the marine atmospheric boundary layer due to the relatively high stability limiting vertical mixing.

1. Introduction

1.1 Background

Sea breeze has long been a topic of interest in both the atmospheric and oceanographic communities. In particular, sea breeze is important to the oceanography community because of the effects it has on marine processes. Orton et al. (2010) describes how sea breeze affects the sea-to-air CO_2 flux. They find that a sea breeze can increase the CO_2 flux up to two orders of magnitude (Orton et al. 2010). Geyer (1997) describes how sea breeze affects salinity in a shallow estuary. Geyer (1997) observed a series of sea breeze events in Cape Cod between July 9 and 14 of 1993 and found that the near-surface salinity of the estuary fluctuated with every consecutive sea breeze. Between morning and late afternoon of each sea breeze, the salinity fluctuated by 10 Practical Salinity Units (PSU). This salinity fluctuation occurred in response and in phase to the sea breeze winds (Geyer 1997).

Sea breeze is also important to the energy, aviation, and air quality industries (Novak and Colle 2006). Steele et al. (2015) describes how sea breeze is an important part of the wind climate in the United Kingdom for wind energy industries (Steele et al. 2015). They find that sea breeze onshore flow significantly impacts wind power generation. During the peak of an idealized sea breeze simulation, they found that sea breeze can generate over 4 Mega-Watts of wind power (Steele et al. 2015). Not only is sea breeze important to the wind energy industries, but also utility companies in general. Sea breeze can have numerous impacts on air pollution (Simpson 1994; Yerramilli et al. 2009). In Simpson (1994), it is mentioned that sea breeze wind within cool stable marine air can transport air pollutant particles from coastal factory chimneys to the internal boundary layer, which is an unstable layer that forms as a result of cool sea breeze air moving over a warm land surface. Once air pollutant particles reach the internal boundary

layer, mixing within the internal boundary layer can make these air pollutants reach ground level (Simpson 1994).

Sea breezes also impact other meteorological phenomenon such as convection and coastal fog (Kingsmill 1995; Tang 2012). Kingsmill (1995) discusses how sea breezes can affect a gust front in Florida. It was found that convection associated with a sea breeze front can initiate the inland propagation of a gust front (Kingsmill 1995). In this study, this convection initiated a region of storms which resulted in a gust front. Once the gust front initiated, it moved inland and collided with a sea breeze from the east Floridian coast creating a collision front. Once the sea breeze front collided with the gust front, the gust front speed decreased 1.5 m s^{-1} (Kingsmill 1995).

1.2 Sea Breeze Mechanics

Sea breezes are a mesoscale phenomenon that results from a surface thermal gradient between an ocean and land surface due to radiative heating. The difference in heat capacity between the land and ocean surface is ultimately what allows the radiative heating to drive the sea breeze. The heat capacity of water is about 4000 $J \cdot kg^{-1}K^{-1}$, whereas the heat capacity of land is only about 800 $J \cdot kg^{-1}K^{-1}$, which can vary depending on the type of surface (Cutnell and Johnson 2009). Due to the large difference in these heat capacities between land and ocean, the land heating rate is considerably greater than the ocean heating rate in the presence of insolation. Furthermore, the soil effective depth (6 cm), which is the depth at which the soil is affected by the solar diurnal cycle, is far less than the ocean mixed layer depth (50-100 m; Stull 1988; Simpson and Sharples 2012; Stewart 2008). Therefore, solar radiation mixes through a smaller depth than the ocean mixed layer. The shallow soil effective depth allows heat to be distributed more freely resulting in the land surface to heat up more quickly than the ocean surface. By mid

to late morning, through surface heat fluxes, the air over the land is relatively warmer than the air over the ocean. Through the hydrostatic equation, the relatively cool air column over the ocean results in a high surface pressure and the relatively warm air column over the land results in a relatively low surface pressure (fig. 1; Miller et al. 2003). The difference in surface pressure between the land and ocean drives an onshore wind characterized as the sea breeze, where the wind flows from the high pressure to low pressure. The low pressure over land creates a convergence zone driving upward vertical motion and the high pressure over the ocean creates a divergence zone driving downward vertical motion.

The temperature difference between the ocean and land surface also creates a density current, also known as a sea breeze gravity current. The maximum wind convergence exists at the head of the sea breeze gravity current, which can be identified as the sea breeze front (figure 1). As the sea breeze gravity current continues onshore, the sea breeze front continues to move inland as long as the density of the air within the sea breeze gravity current is greater than that of the land. Several factors can affect the progression of the sea breeze front, including synoptic wind, friction, terrain slope, and the Coriolis force (Crosman and Horel 2010). An opposing synoptic wind can substantially slow down a sea breeze depending on the speed of the opposing wind. If the opposing wind exceeds the speed of the sea breeze density current, the sea breeze may not propagate inland (Miller et al. 2003; Crosman and Horel 2010). If friction were neglected, sea breeze circulation intensity is maximum about 6 hours after the maximum land-sea temperature difference, which is when the land-sea temperature difference becomes zero (Haurowitz 1947). This difference becomes zero because of land surface radiative cooling due to decreasing insolation late in the afternoon. In the presence of friction, however, the sea breeze circulation intensity is maximum 3 hours after the maximum temperature difference between the

land and sea breeze density current (Haurowitz 1947). At about 3 hours after this maximum difference, the land-sea temperature difference becomes small enough that the frictional force dominates the sea breeze, which causes a decrease in the sea breeze circulation intensity (Haurowitz 1947).

A number of studies have shown that Coriolis force can have an effect on the sea breeze progression, but these effects have little impact on the daytime life cycle of a sea breeze because frictional force and solar heating are generally dominant (Crosman and Horel 2010; Yand and Anthes 1987). Six hours after the onset of the sea breeze, however, changes in the direction of the sea breeze propagation due to Coriolis force become evident (Crosman and Horel 2010; Yand and Anthes 1987).

1.3 Numerical Modelling of Sea Breezes

Sea breeze numerical modeling research has focused on both real sea breeze and idealized sea breeze. Real sea breeze case studies predominated idealized sea breeze studies by the end of the twentieth century mainly because of increased access to observation data and increasing computer capabilities (Crosman and Horel 2010). Also, it is important to acknowledge the benefits of numerical sea breeze simulation over analytical sea breeze simulation. Although analytical solutions provide insight into the physics behind sea breeze dynamics and thermodynamics, their direct application to sea breeze forecasting in a real atmosphere is limited (Simpson 1994). Unlike analytical solutions, numerical sea breeze simulations include physical processes that impact sea breeze characteristics, such as surface heat and momentum exchange, impact of friction, sloping terrain and turbulence simultaneously.

Given the impact of sea breezes effects on marine and atmospheric processes as well as coastal industries, it is important to accurately forecast and further understand sea breezes. Many

efforts have been employed to improve the numerical modelling of sea breezes. It is important to appreciate that sea breeze simulations have made dramatic improvements in the last fifty to sixty years with respect to resolution (Crosman and Horel 2010). As the latter half of the twentieth century progressed, the average vertical and horizontal resolution in models simulating sea breeze increased (Crosman and Horel 2010), contributing to improved sea breeze simulations.

Many studies have emphasized the importance of model resolution in mesoscale forecasting cases (Mass et al. 2002; Colby 2004; Ries and Schlunzen 2009). Colby (2004) emphasized the importance of horizontal resolution for sea breeze forecasting in the New England region. This study used the fifth-generation Pennsylvania State University- National Center for Atmospheric Research Mesoscale Model (Penn State-NCAR MM5) on 9 July and 1 August 2001 sea breeze events. These sea breeze events were simulated at 36 km, 12 km and 4 km horizontal resolutions. By increasing the horizontal resolution from 36 km to 4 km, the absolute error for wind speed and temperature in the sea breeze simulations decreased 0.27 m s^{-1}(Colby 2004). The absolute error of wind speed for the seven sea breeze simulations was 1.67 m s^{-1} for the 36 km grid and 1.40 m s^{-1} for the 3 km grid (Colby 2004).

Not only has fine horizontal resolution been beneficial to sea breeze simulations, but also fine vertical resolution (Ries and Schlunzen 2009). Ries and Schlunzen (2009) illustrated the importance of vertical resolution in sea breeze forecasting over the Bay of Valencia, Spain using the Penn State-NCAR MM5. By increasing the vertical resolution from 34 sigma levels to 52 sigma levels, they found that the sea breeze surface wind speed was closer to observations. At 1600 UTC, the low vertical resolution simulation had a wind speed of 4 m s^{-1}, which was 2 m s^{-1} greater than observed, while the high resolution simulation had a wind speed of about 3 m s^{-1}, only 1 m s^{-1} greater than observed. (Ries and Schlunzen 2009).

A fair representation of the atmospheric initial conditions used to initialize the numerical sea breeze simulations has been shown to be important (Zhang et al. 2005; Berri and Paegle 1990). Zhang et al. (2005) ran the nonhydrostatic National Centers for Environmental Prediction (NCEP) Mesoscale Spectral Model initialized with the NCEP-NCAR reanalysis data for several sea breeze events that occurred over Hawaii in June 1978 (Zhang et al. 2005). If the trade winds over northwestern Hawaii are underestimated in the initial conditions by 2-3m s^{-1}, the sea breeze penetrated further inland on the Hawaiian island (Zhang et al. 2005). Berri and Paegle (1990) simulated a sea breeze event that occurred over the La Plata River region in South America using an anelastic-hydrostatic mesoscale numerical model at a 20 km resolution, initialized with the Global Weather Experiment Data from the European Centre for Medium-range Weather Forecasting (ECMWF) reanalysis. In this study, the sensitivity of the model run to the initial wind field is tested. The authors use a statistical approach and compute the root mean square vector difference (RMS) between the wind speed during the model run and the wind speed at the initial time as a way of measuring forecast signal. RMS departure is also calculated to quantify the noise. If the noise exceeds the forecast signal, the forecast is not meaningful. When the authors initialize with a large domain (more initial ECMWF wind data (25x25 data size) thus less initial errors), the uncertainty (RMS difference) in the wind speed is about 2 m s^{-1} and decreases to 0.5 m s^{-1} by the end of the model run, which is well below the forecast signal (4 m s^{-1}; Berri and Paegle 1990). When the authors initialize with a small domain (less initial ECMWF wind data (17x23 data size) thus more initial errors), the wind speed uncertainty is about 1.5 m s^{-1} after the initialization but the uncertainty increases to over 2 m s^{-1} towards the end of the model run, which is close to the forecast signal (3 m s^{-1}) which indicates an almost meaningless forecast (Berri and Paegle 1990). With these results, they ultimately found that the sea breeze circulation

is sensitive to the errors in the initial wind field. It is important to note that the initial errors increase when the domain size is smaller, because of the limited horizontal resolution of the initial wind data from the ECMWF reanalysis product.

A proper representation of the surface conditions has been shown to be important in sea breeze simulations as well (Zhang et al. 2005; Yang and Chen 2005). Zhang et al. (2005) illustrated the sensitivity of sea breezes to an incorrect soil classification of bare soil that was supposed to be lava rock at the land surface in Hawaii using a coupled mesoscale-land surface model. They coupled the NCEP Mesoscale Spectral Model with the modified Oregon State University Land Surface Model. By classifying lava rocks as bare soil in the numerical model, sea breeze wind speeds were underestimated up to 2-3 m s^{-1} and the horizontal penetration of the sea breeze was overestimated (Zhang et al. 2005). The penetration of the sea breeze is overestimated because of the underestimation of the Waimea jet speed, which opposes the sea breeze inland propagation. The Waimea jet speed is underestimated because of the incorrect surface classification. Model errors were due to the underestimation of surface heat fluxes from the lava rocks being represented as bare soil, which means the land-sea temperature gradient is also being underestimated. In a similar study, Yang and Chen (2005) have also shown the importance of surface properties in simulations of Hawaiian sea breezes for multiple events during July and August of 1990. Using the Penn State-NCAR MM5 model, they found that the land-sea temperature gradient was 1-3˚C lower than observed due to the incorrect surface classification of lava rock as bare ground.

In addition to having a realistic land surface, it is also important to accurately represent the coastal waters for sea breeze forecasting applications. Steele et al. (2013) tested the sensitivity of idealized sea breezes to SST magnitude using the Weather and Research

Forecasting (WRF) model in 2 dimensions with 3 km horizontal resolution and with 35 vertical levels. In the onshore environment, the sea breeze front was most affected by changes in SST. When the SST increases, they found that the land-sea temperature gradient decreases and weakens the sea breeze front propagation speed. For offshore sea breeze wind, they found the wind speed is especially affected by changes in SST. By increasing the SST from 280K to 290K, the overlying air becomes less stable because less dense (warm) air influenced by the warmer SST is beneath denser (cool) air. When the surface layer becomes less stable, more mixing occurs which increases sea breeze wind speed 1-2m s^{-1} when the opposing wind is below 4 m s^{-1} (Steele et al. 2013).

In addition to idealized numerical modeling studies, numerical model studies of historical sea breeze events have been performed to explore the sensitivity of sea breezes to SST. LaCasse et al. (2008) demonstrated the importance of accurately representing horizontal SST gradients associated with the Florida current on the overlying marine atmospheric boundary layers. The Advanced Research WRF (WRF-ARW) model in 2 km resolution with 51 vertical levels was initialized with the relatively low resolution (0.5º) Real-time Global Sea Surface Temperature Analysis (RTG) SST product and compared to simulations initialized with the relatively high resolution (1 km) Moderate Resolution Imaging Spectroradiometer (MODIS) SST (LaCasse et al. 2008) for events under westerly and easterly low level flow nocturnal regimes. Nocturnal flow was of interest in this study because it was the period with least synoptic influences. The coarse resolution RTG was unable to resolve the SST gradient associated with the Florida current, whereas the higher-resolution MODIS did resolve this gradient. Using the MODIS SST, sensible heat flux increased over the Florida Current by 12 W m^{-2} and decreased over the Florida-Hatteras shelf by 6 W m^{-2} for easterly flow. Latent heat flux increased over the Florida

current by 60 W m-2 and decreased over the Florida-Hatteras shelf by 20 W m-2 for easterly flow (LaCasse et al. 2008). These changes in surface fluxes indicate that WRF is sensitive to high resolution SST (LaCasse et al. 2008).

1.4 Motivation

The Long Island Sound (LIS) is an estuary located in the northeast United States that has considerable horizontal SST variations. This complication makes it necessary for numerical models to include a realistic and high resolution SST gradient to accurately simulate atmospheric and estuary coastal circulations. Estuarine circulations in Long Island Sound are strongly modulated by tides and input from local rivers, which makes the hydrography complex (Latimer et al. 2013). In the summer, the SST is typically cooler at the mouth of Long Island Sound and relatively warm at the closed end of the estuary. The cool SST at the mouth is mostly due to fast tidal currents of 60 cm s^{-1}, which creates large vertical shear resulting in strong tidal mixing with cool deep water (Bowman and Esaias 1981; Whitney and Garvine 2008; Codiga and Rear 2004). An important contributor to the warm western Long Island Sound is the drainage of warm Hudson River water of 260 $m^3 s^{-1}$ into the western end of the Sound through tidal dispersion at the ocean surface layer (Blumberg and Pritchard 1997; Fribance et al. 2013; Wilson 1976; Ullman and Codiga 2004). This complexity in the estuarine physics which results in a strong horizontal gradient in the SST drives the need for a realistic SST product to be used for sea breeze simulations in the Long Island Sound region, and likely other estuaries with complex horizontal SST gradients.

Long Island Sound is a body of water located in a highly populated region, including New York City, the most populated metropolitan area in the United States (United States Census Bureau). Given the large socioeconomic impacts of accurate coastal circulations, it is crucial to

improve sea breeze simulations in the vicinity of Long Island Sound. For example, sea breeze can help decrease electrical output on power grids, which can ease demands on utility companies (Lombardo et al. 2016). Sea breezes are fairly frequent in the Long Island Sound region during the summer. Novak and Colle (2006) showed that sea breezes are common in the spring and summer in the New York City metropolitan area using observational data available in New York City (Novak and Colle 2006). Given the high frequency of sea breeze events and the socioeconomic impacts sea breeze has on this region, it is imperative to study sea breezes in Long Island Sound.

The benefits of fine horizontal and vertical resolution as well as realistic surface and initial conditions in sea breeze simulations have been documented in past studies (Mass et al. 2002; Colby 2004; Ries and Schlunzen 2009; Zhang et al. 2005; Yang and Chen 2005; Berri and Paegle 1990). Realistic initial conditions are directly related to the importance of properly representing the surface, especially in regions where there are complex coastlines. In order to have a realistic initial condition in sea breeze simulations, the coastline must be properly represented in the initial condition product. For example, an accurate initial sea temperature requires a properly represented surface (Zhang et al. 2005; Yang and Chen 2005). There has been limited work on the importance of a realistic representation of a coastline in the initial conditions for sea breeze simulations in New England (Lombardo et al. 2016). The coastline of Connecticut and Rhode Island is complex, which requires numerical models to use realistic surface properties and initial conditions. Colle et al. (2003) acknowledges the complexity of the coastal geometry of the Long Island Sound region, but does not go into detail on the impacts of the intricate coastline on the sea breeze.

Moreover, there has not been much focus on the effects of the horizontal SST gradient of

sea breeze simulations. Although LaCasse et al. (2008) focused on the impacts of SST resolution on the marine atmospheric boundary layer (MABL) over the Atlantic Ocean, the authors did not focus specifically on sea breeze but instead on low level nocturnal flow that developed in an environment with an SST gradient perpendicular to the coast, rather than parallel to the coast such as in LIS. In order to increase our understanding of Connecticut sea breezes, there needs to be an accurate coastline in the model initialization and relatively high resolution SST products to resolve the complex SST structure that exists in Long Island Sound. The sensitivity of the Connecticut sea breeze circulation and the sea breeze MABL to coastal geography and SST resolution can be further understood if a more realistic coastline and SST in the sea breeze simulations are imposed.

This study will illustrate the importance of a realistic coastline and realistic SST products for sea breeze simulations in the Long Island Sound region. Chapter 2 explains the model framework and experiments. Chapter 3 discusses the numerical experiment results. Features of the Connecticut sea breeze that are found to be particularly sensitive or unexpectedly insensitive to SST will be analyzed in Chapter 4. Chapter 4 will end with concluding remarks.

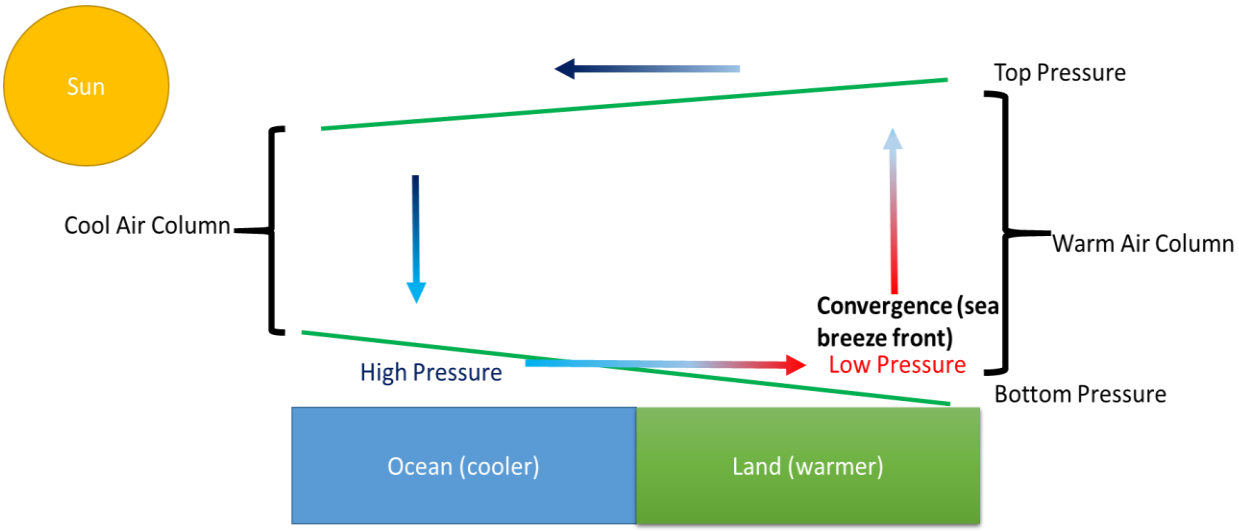

Figure 1. A schematic of the sea breeze circulation. The green lines are isobars and the arrows are wind vectors which illustrate the sea breeze circulation.

2. Methodology

2.1 Model Framework

The WRF-ARW Version 3.6.1 (Skamarock et al. 2008) numerical model is used to simulate two sea breeze events that occurred on 8 July and 21 August 2013 in the Long Island Sound region. WRF is a mesoscale atmospheric model that solves for the fully compressible nonhydrostatic moist Euler Equations in flux form (Skamarock et al. 2008). The Euler Equations are a system of nonlinear partial differential equations which are further modified so that the sphericity of the Earth is considered. These conservative equations include the conservation of momentum, conservation of heat, conservation of mass and conservation of moisture. The nonconservative material derivative of geopotential, the equation of state for a moist ideal atmosphere, and the inverse density diagnostic relation is also included. The model solves the prognostic Euler Equations using a numerical integration scheme called the third-order Runge-Kutta (Skamarock et al. 2008; Klemp et al. 2007) method. A time-split scheme is used to separate the physically significant low frequency modes, with economically larger time steps, from the high frequency, physically insignificant modes, with smaller time steps to maintain stability (Skamarock et al. 2008; Wicker and Skamarock 2002). High frequency horizontally propagating acoustic modes and gravity waves are solved by forward-backward difference integration while the vertically propagating acoustic modes and buoyancy oscillations are solved by a vertically implicit scheme. For spatial discretization, the model solves for the advection terms using second to sixth order upwind-biased and centered schemes.

The WRF uses an Arakawa C-staggering horizontal grid (Arakawa and Lamb 1977), in which u, v and w velocity points are staggered half a grid length from mass points. The mass points contain conserved variables such as potential temperature and moisture. In this study, the

u, v and w velocities are unstaggered using a WRF postprocessor known as NCAR Command Language (NCL) so that the mass points are collocated with the u, v and w points. This allows for the calculation of variables that depend on both velocity and conserved variables (e.g. potential temperature) to be easily computed, such as the Richardson number.

Model domains in this study include a 9 km domain encompassing the eastern United States, a nested 3 km domain over the northeastern United States, and a nested 1 km domain over southern New England (figure 2). The two outer domains are designed to simulate the synoptic and broader mesoscale processes during the events, while the 1 km is designed to capture the sea breeze. Therefore, for the remainder of this study, only the 1 km domain will be discussed.

The vertical resolution is 48 levels on a sigma pressure coordinate system for all 3 domains. This is a terrain-following hydrostatic-pressure coordinate system that is commonly used in weather predication models (Laprise 1992; Skamarock et al. 2008). A sigma coordinate system is used since terrain in two spatial dimensions creates complications for pressure, logarithmic pressure and height coordinate systems near the surface. Sigma coordinates are obtained by subtracting the hydrostatic pressure at a given level by a constant top pressure. This difference is then divided by the difference in the surface pressure at a given location and the constant top pressure (Skamarock et al. 2008). The sigma coordinate system is unitless and has a value of one at the surface, and zero at the top level. The first level is at the surface layer. As discussed in Chapter 1, it is important to have a fine vertical resolution for sea breeze simulations, which is why the vertical resolution is increased from default 30 levels. The lowest level is about 54 meters above the terrain, and the top pressure level is 100 hPa. This setup of the vertical coordinate is the same in all three domains. Of the 48 levels, 10 are within the sea breeze layer.

The various physics schemes in WRF parameterize processes that are too small to be explicitly solved in the model (table 1). The Kain-Fritsch cumulus parameterization scheme is used in the 9 km domain (Kain and Fritsch 1990; Kain 2004). It is important to note that no cumulus parameterization is needed for domains with less than 4 km resolution (Skamarock et al. 2008; Done et al. 2004; Weisman et al. 1997). Therefore, convection is resolved explicitly for the 3 km and 1 km domains. The microphysics scheme being used is the Morrison microphysical scheme (Morrison et al. 2009). This is a two-moment scheme, which has more flexibility in moisture particle size distribution than other microphysics schemes with only one-moment (Morrison et al. 2009). There is more flexibility in this two-moment scheme because the size distribution intercept parameter (N_0) in the particle size distribution equation can vary, whereas in a one-moment scheme this parameter is constant (Morrison et al. 2009). This flexibility in the particle size distribution will benefit if precipitation were to occur in the model simulations. The planetary boundary layer (PBL) scheme used in sea breeze simulations should be carefully considered. Steele et al. (2013) evaluates the impact of the Mellor-Yamada-Nakanishi-Niino Level 2.5 (MYNN; Nakanishi and Niino 2006; Nakanishi and Niino 2009), Yonsei University (YSU; Hong et al. 2006) and Mellor–Yamada–Janjic Scheme (MYJ; Janjic 1994) PBL schemes in numerical sea breeze circulations. The YSU is a first order non-local scheme. This PBL scheme is not suitable for coastal applications since it overestimates wind speed offshore (Steele et al. 2013; Krogsaeter et al. 2011). The MYNN and MYJ are 1.5 order local schemes that use the turbulent kinetic energy equations to resolve turbulence closure (Steele et al. 2013). The MYJ, however, can underestimate the height of the PBL. Given these limitations, the MYNN is the most suitable PBL scheme to use for sea breeze simulations since it most accurately represents the PBL height and gives more realistic wind profiles in a coastal setting. Thus, the

PBL scheme being used in this study will be the MYNN 2.5 scheme. This PBL scheme is supplemented by the MYNN surface layer scheme. The MYNN PBL and surface scheme are major contributors in determining the 2-m temperature, surface latent heat flux, surface sensible heat flux, 10-m wind and the 2-m mixing ratio. The land-surface model used is the Unified Noah Land Surface Model, which is commonly used by the National Center for Atmospheric Prediction (NCEP; Ek et al. 2003). The Unified Noah Land Surface model computes land sea temperature, and impacts the 2-m fields in the MYNN scheme and the model fields.

The 2-m diagnostic variables depend on the surface variables and the first model level (54-m) variables based from the vertically integrated Monin–Obukhov similarity theory (MYNN Surface Physics Module; Jiménez et al. 2012; Stull 1988; Monin and Obukhov 1954). The 2-m potential temperature (θ_{2m}), for example, is calculated from equation (1), where θ_g is the surface potential temperature, θ_a is the first model level (54-m) potential temperature and z_0 is the aerodynamic roughness length. $\psi_h(2/L)$ and $\psi_h(z/L)$ are respectively the 2-m and 54-m integrated similarity functions for heat calculated by the MYNN surface layer scheme, where L is the Obukhov length (Jiménez et al. 2012; Stull 1988). A comprehensive background and derivation of the 2-m diagnostic variables based from the Monin-Obukhov theory can be found in Stull (1988) and Jiménez et al. (2012).

$$(1)\ \theta_{2m} = \theta_g + (\theta_a - \theta_g)\frac{\ln\left(\frac{2}{z_0}\right) - \psi_h\left(\frac{2}{L}\right)}{\ln\left(\frac{z}{z_0}\right) - \psi_h\left(\frac{z}{L}\right)}$$

For this study, the ocean sea temperature will be used as a proxy for SST. Moreover, the terms SST and sea temperature will be used interchangeably in this study since they are set equal in the model. The SST in the WRF simulations will be temporally static in all three domains,

which is conventional in meteorological forecasting operations. This is because diurnal variations in surface temperature of the coastal ocean waters are smaller than over adjacent land. In part of this study, emphasis will be placed on the impact of the horizontal SST gradients in the Long Island Sound on the structure of sea breeze circulations.

The analysis product used to initialize the atmosphere in all simulations is the North American Regional Reanalysis (NARR; Mesinger et al. 2006). The NARR data is made available by the National Oceanographic and Atmospheric Administration's National Climatic Data Center (NOAA NCDC; https://www.ncdc.noaa.gov/data-access/model-data/model-datasets/north-american-regional-reanalysis-narr). This reanalysis product has a 3 hr temporal resolution and a 32 km horizontal spatial resolution on a Northern Hemisphere Lambert Conformal Conic grid according to NOAA Earth System Research Laboratory Physical Science Division (NOAA ESRL PSD; http://www.esrl.noaa.gov/psd/data/gridded/data.narr.html). The NARR data is processed for the WRF model by the WRF Preprocessing System (WPS).

2.2 Coastline Sensitivity Experiments

The relatively coarse 32 km NARR is unable to resolve the complex coastline of Long Island Sound. This results in the designation of water regions as land, and the designation of land regions as water in the numerical model. This can be seen in figure 3a, where the light brown represents land and the purple represents ocean. The grey solid lines are the representation of the coastline in the 1 km WRF domain. As can be seen from this figure, the NARR coastline is very different than the high-resolution WRF coastline. Western Long Island Sound is being represented as land, central coastal Connecticut is being represented as water, and most of Long Island is being represented as water (fig. 3a). Initializing WRF with these discrepancies can have an impact on the forecasting of the sea breeze. Since western Long Island Sound is being

represented as land in the initial conditions, the sea temperature used to initialize the simulation in this water region will be a land value, which can be much higher than the Long Island Sound sea temperature during the day and much lower during the night. In regions where water is initially designated as land, such as western Long Island Sound, the 1 km WRF landmask will not correct the sea temperature due to the static SST. These errors in the ocean sea temperature in western Long Island Sound will remain through the entire sea breeze simulation. In regions where land is initially being designated as water, the sea temperature evolves and fluctuates with the diurnal cycle due to the dynamic nature of land sea temperature in the model.

A method was developed to improve the numerical representation of the complex coastline in the initial conditions (Lombardo et al. 2016). This coastline modification procedure is demonstrated for the August sea breeze event simulation initialized at 0300 UTC in figure 3. The sea temperature at initialization before the coastline modification is shown in figure 3a. The final result of this coastline modification is shown for the landmask proxy in figure 3b and for the sea temperature in figure 3d. This procedure modifies the sea temperature and plant canopy surface water during preprocessing. These are the only two variables modified during preprocessing because they are the only variables related to the misrepresentation of the coastline used during WRF simulations. Plant canopy surface water is used as a proxy for the NARR landmask. The NARR ocean sea temperature is extracted and interpolated to a 1 km grid over the 1 km WRF domain using a triangulation-based linear interpolation (fig. 4c**)**. Similarly, the NARR land sea temperature is extracted and interpolated in a separate 1 km grid over the 1 km WRF domain using the same interpolation scheme (fig. 4b**)**. The landmask designation (land/ocean) defined in the 1 km WRF is extracted used to extract land sea temperature from the interpolated NARR land sea temperature. This extracted interpolated land sea temperature is then

mapped onto the interpolated ocean sea temperature (fig. 4d**)**, resulting in a more accurate representation of the regional coastline. This procedure will be performed for all NARR analyses times, and for all WRF domains (9 km, 3 km, 1 km). The result of this high resolution (HR) coastal correction will be referred to as *HRCoast* going forward. The original representation of the coastline before this correction will be considered the *OrigCoast*.

A series of sensitivity experiments will be performed to quantify the impact of the resolution of the coastline and initialization time on sea breeze circulations (table 2). For the first set of sensitivity experiments, 18 hour WRF simulations initialized at 0300 UTC will be performed. The simulations initialized at night (0300 UTC) will be considered *OrigCoast_night* and *HRCoast_night* since the land at this time is cooler than the ocean. These sensitivity experiments are designed to explore the impacts of initializing with a low resolution coastline, and consequently a misrepresented ocean surface temperature in western Long Island Sound with an anomalously cool sea temperature. For the second set of sensitivity experiments, the coastline modification procedure will be performed for 24 hour WRF simulations initialized at 2100 UTC, a day prior to the sea breeze event. The simulations initialized the previous day (2100 UTC) will be considered *OrigCoast_day* and *HRCoast_day* since the land at this time is warmer than the ocean. This sensitivity experiment is designed to explore the impacts of initializing with a low resolution coastline, and consequently a misrepresented ocean surface in western Long Island Sound with an anomalously warm sea temperature. These two sets of sensitivity experiments will be performed for both the August and July sea breezes; therefore, the coastline modification procedure will be performed twice for each of the two sea breeze events. These experiments have a total of eight cases, four of which are *OrigCoast* cases and four of which are *HRCoast* cases. The culmination of these cases will be referred to as the coastline sensitivity experiments.

2.3 SST Resolution Sensitivity Experiments

A second series of sensitivity experiments will be performed to evaluate the sensitivity of numerical sea breeze circulations to horizontal SST resolution (table 2). In these experiments, the procedure described above will be used for simulations in which the NARR was used for SST initial conditions to ensure accurate representations of the coastline. The impact of three different SST resolutions on the development of numerical sea breeze circulations will be quantified for the August sea breeze (fig. 5) and the July sea breeze (fig. 6). These include a low resolution SST (spatially uniform), moderate resolution SST (32 km) and a high resolution SST (1 km). Using high resolution SST products such as G1SST in short-term mesoscale forecasting may decrease the need to couple ocean models to forecasting models (LaCasse et al. 2008; Lazarus et al. 2007).

A uniform SST was imposed onto the *HRCoast_night* using MATAB for the first WRF simulation of the SST resolution sensitivity experiments. This uniform SST was imposed in all three model domains. The value of the uniform SST is based on the mean daily average of the G1SST in the Long Island Sound, which is about 22˚C for the August sea breeze (fig. 5a**)** and 22.5˚C for the July sea breeze (fig. 6a**)**. This control simulation is considered the least realistic of the SST products being used in the SST resolution sensitivity experiments. Although this SST product is not realistic, this simulation will help determine the importance of a horizontal SST gradient.

The second simulation uses a moderate horizontal resolution SST provided by the 32 km NARR that will be referred as the NARR. The NARR is obtained from the *HRCoast_night*. The NARR is adjusted to the daily G1SST mean so that the Long Island Sound SST mean is the same for all three model simulations in these experiments. This adjustment is performed by setting the

NARR SST at a buoy (44039) in central Long Island Sound from 21.34˚C to the mean G1SST (22.04˚C), where 21.34˚C is the NARR Coast SST at the location of the buoy in the August Sea breeze. The difference between 21.34˚C and 22.04˚C is obtained (0.7˚C) and added to the ocean sea temperature in all three WRF domains. For the July sea breeze, the difference between the NARR coast SST and mean G1SST at the same buoy location is -0.083˚C. As can be seen in figure 5b and figure 6b, a moderate SST gradient in this experiment results from using reanalysis products. The impacts of this SST gradient will be further analyzed in the study.

The third simulation uses the G1SST product, which is the most realistic of the three SST products. The G1SST is a global dataset that is part of the Group for High Resolution SST (GHRSST) project. The G1SST data is made available by the National Aeronautics and Space Administration Jet Propulsion Laboratory Physical Oceanography Distributed Active Archive Center (NASA JPL PODAAC; http://dx.doi.org/10.5067/GHG1S-4FP01). This product assimilates satellite SST data from Aqua's Advanced Microwave Scanning Radiometer EOS (AMSRE), Aqua MODIS, MetOp-A's Advanced Very High Resolution Radiometer 3 (AVHRR-3), the Tropical Rainfall Measuring Mission Microwave Mission (TRMM) imager, Envisat's Advanced Along Track Scanning Radiometer (AATSR) and the Geostationary Operational Environmental Satellite 13 (GOES-13) imager. G1SST also assimilates this satellite data with in situ data from moored and drifting buoys using a variational blending algorithm (Chao et al. 2009). This NASA product has a spatial resolution of 0.01 degrees (O(1 km)). The temporal resolution is daily and the grid structure is rectilinear. The rectilinear G1SST dataset is bilinearly interpolated and converted to a lambert projection which is the projection of the WRF model grid. The dataset is then mapped onto *HRCoast_night* for each model time and for each of the three WRF domains. As figure 5c and figure 6c illustrate, the SST gradient in this product is

relatively large for the August and July sea breeze, especially in east Long Island Sound.

2.4 Observation Sources

The model output from these sensitivity experiments will be validated with available observations. The surface temporal validations are performed at three buoy locations which are shown in figure 6 as circles. The buoy data is obtained from the National Buoy Data Center and operated by University of Connecticut for buoys 44022, 44039 and 44060 (NOAA NDBC; http://www.ndbc.noaa.gov/). As can be seen in figure 7, buoy 44022 is in western Long Island Sound (WLIS buoy), buoy 44039 is in central Long Island Sound (CLIS buoy), and buoy 44060 is in east LIS (ELIS buoy). Unlike the model SST, the buoy SST is dynamic and is quarter-hourly.

In addition to buoy observations, land observations will be used as well (triangles in fig. 7). The hourly land surface observations of 2-m air temperature are from the Iowa Environmental Mesonet (IEM; https://mesonet.agron.iastate.edu/archive/). The sites that will be observed are the Westchester County Airport in Westchester NY (HPN), Sikorsky Memorial Airport in Bridgeport CT (BDR), Tweed-New Haven Airport in New Haven CT (HVN), and the Groton-New London Airport in Groton CT (GON).

Visible satellite images and the radar composite images are obtained from the Mesoscale and Microscale Meteorology Division of the National Center for Atmospheric Research (MMM NCAR; http://www2.mmm.ucar.edu/imagearchive).

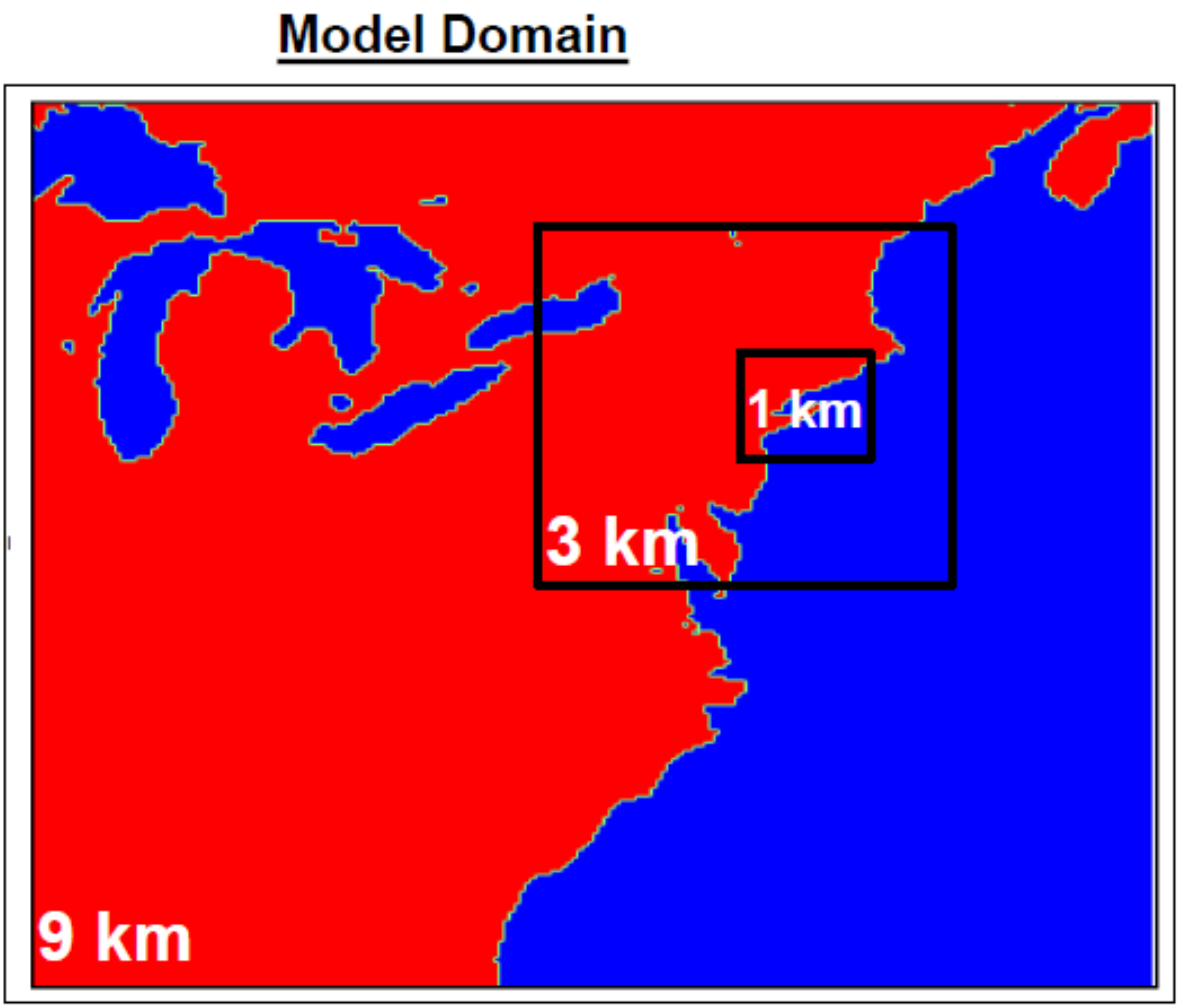

Figure 2. WRF nested model domain: 9 km, 3 km, 1 km.

Table 1. The WRF physics and domain settings.

WRF Setting	**Selected option**		
	Synoptic Domain	**Mesoscale Domain**	**Sea Breeze Domain**
Horizontal Resolution	9 km	3 km	1 km
Vertical Resolution	48 sigma levels		
Cumulus Scheme	Kain-Fritsch Cumulus Parameterization	Clouds solved explicitly	Clouds solved explicitly
Microphysics Scheme	Morrison Microphysical		
Planetary Boundary Layer Scheme	Mellor-Yamada-Nakanishi-Niino (MYNN) Level 2.5		
Surface Layer Scheme	MYNN Surface Layer		
Land Surface Scheme	Unified Noah Land Surface Model		

Table 2. The WRF model experiments.

	Initialization time	**21 August 2013 Experiments**	**08 July 2013 Experiments**
Coastline Sensitivity Experiments	**Nighttime**	*OrigCoast_night*	*OrigCoast_night*
		HRCoast_night	*HRCoast_night*
	Daytime	*OrigCoast_day*	*OrigCoast_day*
		HRCoast_day	*HRCoast_day*
SST Resolution Sensitivity Experiments	**Nighttime**	Uniform	Uniform
		NARR	NARR
		G1SST	G1SST

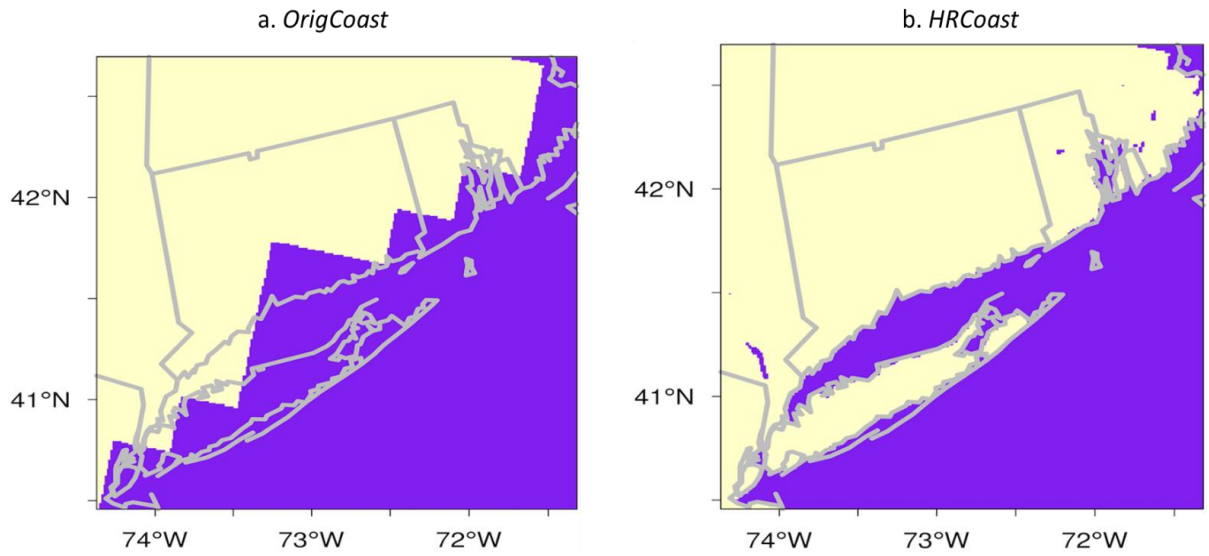

Figure 3. land (brown) and ocean (purple) representation for (a) *OrigCoast* and (b) *HRCoast*. The grey solid line are state boundaries and 1 km coastline.

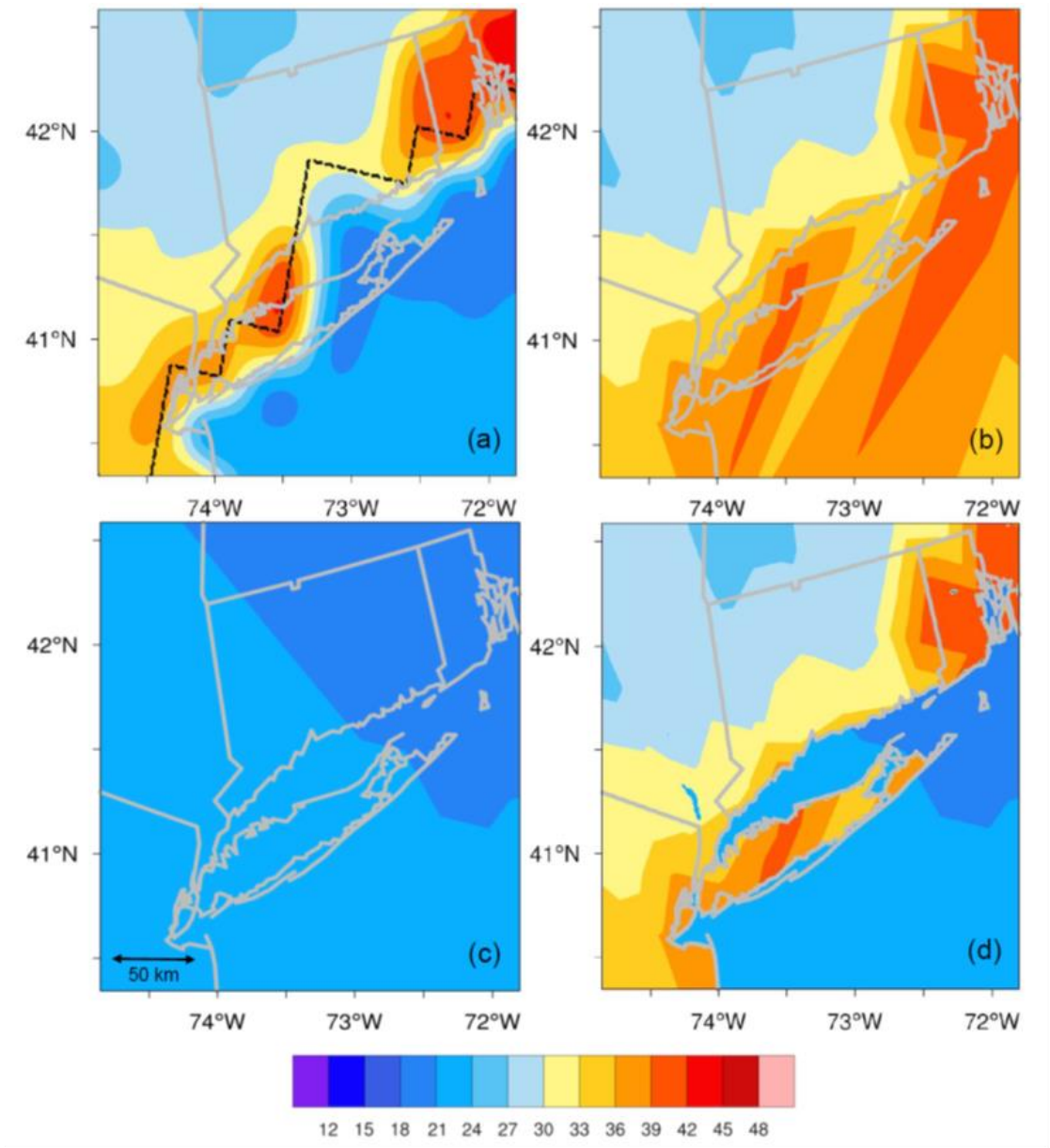

Figure 4. 21 August 2013 Coastline modification procedure plotting skin temperature (˚C). (a) *OrigCoast_day* (dashed line represents NARR (32 km) representation of coastline, and grey line represents state boundaries and high resolution (1 km) coastline). (b) NARR defined land interpolated from (a). (c) NARR defined ocean interpolated from (a). (d) *HRCoast_day*.

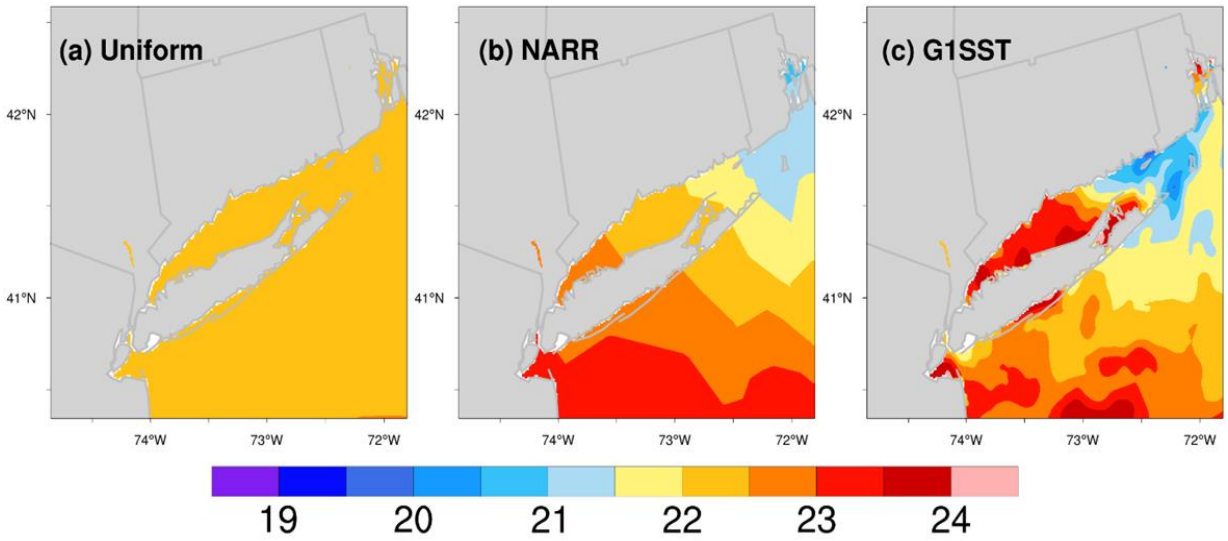

Figure 5. 21 August 2013 SST input (˚C) for (a) Uniform, (b) NARR and (c) G1SST.

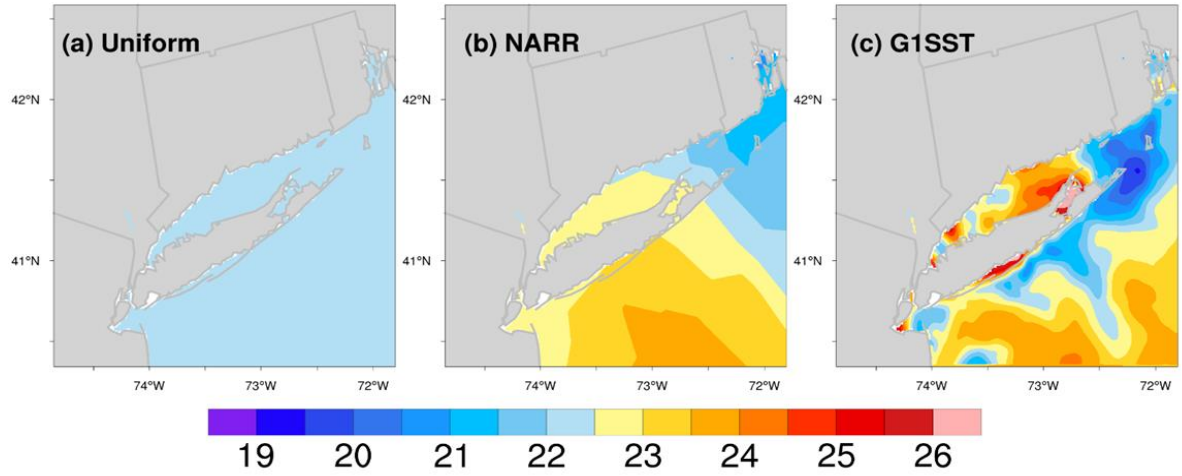

Figure 6. 08 July 2013 SST input (˚C) for (a) Uniform SST, (b) NARR and (c) G1SST.

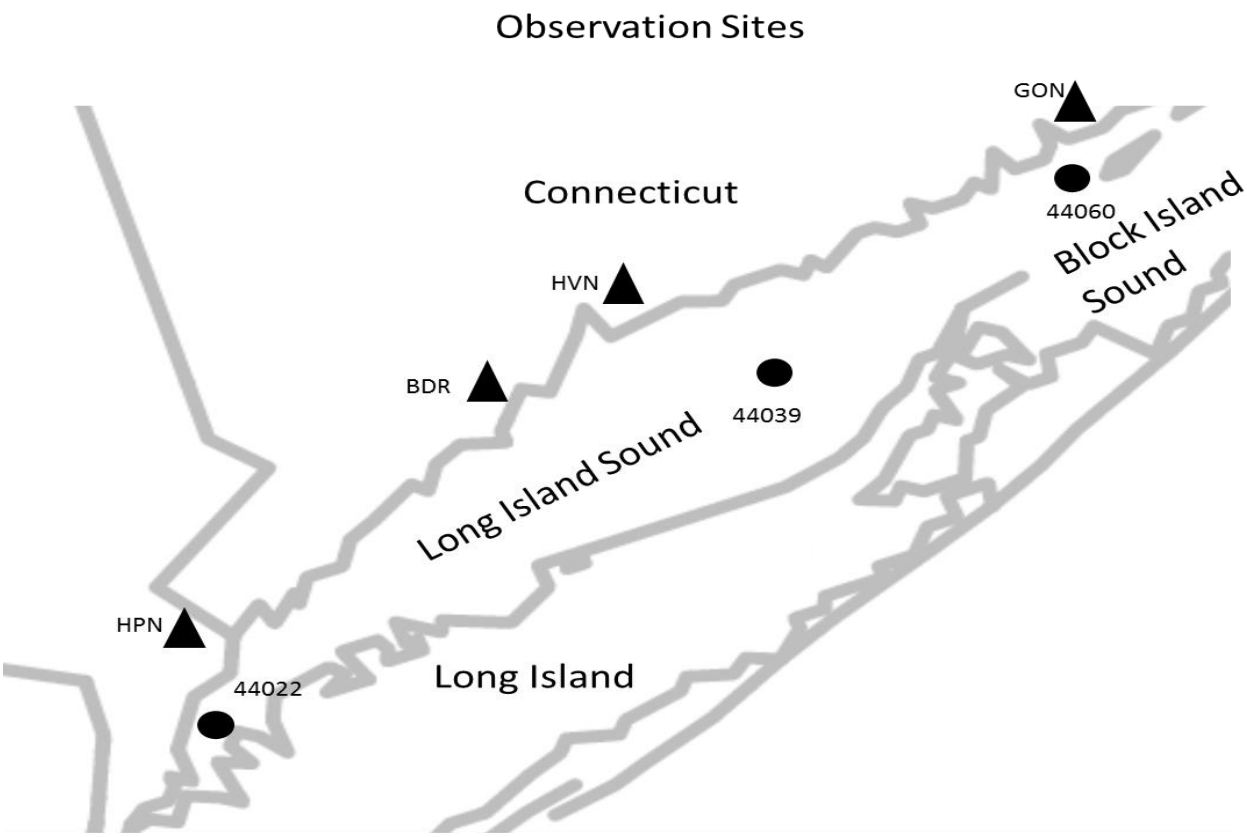

Figure 7. Observation sites. Circles denote buoy sites, and triangle denotes land sites. Geographical locations commonly referred to in this study are labelled here.

3. Results

3.1 Introduction to Results

3.1.1 Introduction to the Output Variables

The effects of a coarse coastline and SST resolution on the sea temperature, 2-m (near-surface) air temperature, 10-m wind and 54-m (lowest model level) horizontal wind convergence are explored for the July and August sea breeze events. These variables best describe the various sea breeze features. The sea temperature and near-surface air temperature are extracted directly from the WRF output. The 10-m wind and 54-m wind convergence are variables derived using NCL. The 10-m wind is derived from the 10-m zonal (u) and 10-m meridional (v) WRF variables. It is important to recall that the ocean sea temperature model output is temporally static.

The horizontal wind convergence is derived from the 54-m meridional and the 54-m zonal wind (eq. 2). This variable is used to trace the sea breeze front for the different WRF sensitivity experiments. A centered-finite difference is used to compute the derivative of the terms to get the wind convergence. In the SST sensitivity experiments, in addition to surface variables, model variables will be explored in vertical cross sections up to 2 km into the boundary layer. These variables include wind convergence, potential temperature, and wind.

$$\text{(2) Wind Convergence} = -\left(\frac{\partial u}{\partial x} + \frac{\partial v}{\partial y}\right)$$

Surface heat flux will also be addressed throughout this study to explain how sea temperature impacts 2-m air temperature. Surface heat flux links surface and model processes. The surface heat fluxes are sensible heat flux and latent heat flux. Sensible heat flux measures how much heat transfers between the ocean and atmosphere by conduction. Latent heat flux

measures how much heat transfers between the ocean and atmosphere contributed by evaporation. Evaporation is a liquid-to-gas phase change that releases heat into the atmosphere, which is quantified by a temperature-dependent variable called the latent heat of vaporization (L_e).

Model sensible and latent heat fluxes are calculated based on Monin-Obukhov similarity theory (Monin and Obukhov 1954). The sensible heat flux depends on dry air density (ρ; kg m^{-3}), specific heat capacity at constant pressure (c_p; J $kg^{-1}K^{-1}$), bulk transfer coefficient (C_h) computed by the MYNN, mean wind speed (U; m s^{-1}), surface potential temperature (θ_g; K) and first model level (54-m) potential temperature (θ_a; K) (eq. 3; Liu et al. 2013; Tong et al. 2006). The latent heat flux depends on latent heat of vaporization (L_e; J kg^{-1}), dry air density (ρ; kg m^{-3}), bulk transfer coefficient (C_q), mean wind speed (U; m s^{-1}), moisture availability (M), surface mixing ratio (q_g) and 54-m mixing ratio (q_a) (eq. 4; Liu et al. 2013; Tong et al. 2006).

(3) sensible heat flux = $\rho c_p C_h U(\theta_g-\theta_a)$; (Tong et al. 2013)

(4) latent heat flux = $L_e \rho M C_q U(q_g-q_a)$; (Tong et al. 2013)

A positive sensible heat flux indicates a transfer of heat from the ocean to the atmosphere, which occurs when the air aloft is cooler than the surface. A negative sensible heat flux indicates a transfer of heat from the atmosphere to the ocean, which occurs when the air aloft is warmer than the surface. A positive latent heat flux indicates a transfer of moisture from the surface to the air aloft, which occurs when the air aloft has less moisture than the surface. A negative latent heat flux indicates a transfer of moisture from the air aloft to the surface, which occurs when the air aloft has more moisture than the surface.

3.1.2 General Setup of Results

Before the model results are assessed, comparisons between model sea temperature and

observation sea temperature will be displayed for initial ocean sea temperature model validation for select experiments. Initial sea temperature validation is designed to give an idea on which model run sea temperature is more realistic for the coastline and SST sensitivity experiments. Knowing the accuracy of the initial sea temperature will provide perspective on model accuracy when discussing the model results.

For the coastline sensitivity experiment, model variables will be described for both the cool and warm initialization time, and for the August and July sea breezes. The *HRCoast_night* and the *OrigCoast_night* will be described separately with regards to sea temperature, followed by 2-m temperature and 10-m wind. These two model runs will then be compared to one another using difference plots for 2-m temperature, and wind, as well as wind convergence. These analyses are intended to find the impacts of the coarse coastline. This same format will be employed for the *HRCoast_day* and the *OrigCoast_day* model runs, and for both the August and July sea breezes.

For the SST sensitivity experiments, these variables are observed in both the SST uniform, NARR adjusted and G1SST model runs. The NARR adjusted and the G1SST will be compared to the SST uniform (SST sensitivity experiment control). The temporal evolution of the sea breeze of each case will be analyzed in the SST sensitivity experiments. In addition, the impacts sea temperature has on the 2-m temperature will be explained in a context using surface heat fluxes.

Throughout chapters 3 and 4, the results are qualitatively as well as quantitatively described. The quantities are extracted from the WLIS, CLIS and ELIS buoy locations in the model. The model output at these buoy locations are considered representative of the regions in which they reside. For example, the location of WLIS is considered representative of the western

Long Island Sound region.

3.1.3 August Sea Breeze and Synoptic Conditions

The 21 August 2013 sea breeze event is captured by radar and satellite. Radar and satellite images of the sea breeze are shown in figure 8. The sea breeze fronts can be seen in the reflectivity as a line over coastal Connecticut and over central Long Island (fig. 7d-f). The Connecticut sea breeze front, which is the focus of this study, is identified with a circle in (d-f). There is minimal cloud development in this sea breeze event, which makes it difficult to detect the sea breeze with visible satellite imagery (fig. 8a-c). There is a sparse cumulus field, however, which allows parts of the sea breeze front to be seen in southeast Connecticut in the satellite image (fig. 8a-c). As time progresses, there is indication of an inland progressing sea breeze front, especially in central Connecticut as indicated by the composite radar images. Given the calm wind in the New England region during the sea breeze, the existing synoptic conditions are light (figure 8g-h).

3.1.4 July Sea Breeze and Synoptic Conditions

The 08 July 2013 sea breeze is also captured by radar and satellite. Radar and satellite images of the sea breeze are shown in figure 8. In this sea breeze, there is considerable cloud development inland. The line of clearing in the cumulus field in coastal eastern Connecticut is evidence of a sea breeze front in the visible satellite imagery (fig. 9a-c). In central and west Connecticut, the sea breeze front is evident through the composite radar images with a line of weak radar echoes along the coast (fig. 9d-f). As time progresses, the CT sea breeze originating from WLIS remains almost stationary at the coast of western Long Island Sound as indicated by both the visible satellite and composite radar images (fig.9a-f). Given the strong, persistent, widespread westerly and southwesterly winds in southern New England, New Jersey, New York

and the Mid-Atlantic Bight, the synoptic conditions during this sea breeze event are relatively strong. These widespread westerly and southwesterly winds originate from a lee trough through the Appalachians (fig. 9g-h). As westerly flow passes through the Appalachians, subsidence occurs on the leeside. When the air sinks, adiabatic compression occurs, which allows a decrease in the vertical potential temperature gradient at the leeside. According to the conservation of potential vorticity, as the vertical potential temperature gradient decreases, the relative vorticity must increase for potential vorticity to be conserved (Martin 2013; Holton and Hakim 2012). An increase in relative vorticity at the leeside of the Appalachians results in stronger large-scale cyclonic vorticity (more convergence). The curvature of cyclonic flow results in a southerly and southwesterly flow in the northeast United States, which explains the widespread southwesterly/westerly synoptic-scale wind during the 08 July 2013 sea breeze.

3.2 August Sea Breeze Coastline Sensitivity Experiments

3.2.1 Initial Sea Temperature Model Validation for OrigCoast_night and HRCoast_night

It is important to validate the model SST with observations for the coastline sensitivity experiments before model output is presented. Figure 10a-c shows 18-hr time series for the WLIS, CLIS and ELIS buoys. In WLIS, the *OrigCoast_night* sea temperature is 4.6˚C lower than observations at 1700 UTC. The *HRCoast_night* sea temperature is only 2.3˚C from buoy observations in WLIS (fig. 10a). In CLIS, *OrigCoast_night* and *HRCoast_night* are respectively 2.2˚C and 2.4˚C lower than observations. Since the ocean is being represented properly as water in both simulations in this particular region, it is expected that the sea temperatures are similar. In ELIS, *OrigCoast_night* is 1.3˚C cooler than observations while *HRCoast_night* is 1.3˚C warmer than observations during the sea breeze event. These initial results indicate that the *HRCoast_night* simulation uses a more realistic SST, which could potentially produce a more

realistic simulated sea breeze.

3.2.2 OrigCoast_night August Model Results

In the *OrigCoast_night* at the initialization time 0300 UTC, the Long Island Sound sea temperature for the August sea breeze event is anomalously cooler in the western region (figure 11a). The black dashed line in figure 11a represents the original NARR's representation of the coastline. The grey solid line in the figure represents the 1 km, high resolution coastline. The SST in WLIS is 19.8˚C, CLIS is 21.7˚C and ELIS is 18.3˚C. These cold anomalies in WLIS and CLIS are occurring because the ocean is being treated as land in the initial conditions and therefore is initialized with a cool, evening land surface sea temperature value. During the warm season at the initial time of 0300 UTC, the land is typically cooler than the ocean because of the differing heat capacities. The shallow land surface layer affected by the diurnal cycle allows the land to cool at a substantially higher rate than the ocean during the overnight.

Recall that the ocean sea temperature is static for the duration of the model run. Therefore, the sea temperature remains anomalously cool in WLIS region during the sea breeze while the land heats up due to solar heating.

The near surface (2-m) air temperature is modulated by the underlying sea temperature. The 2-m temperature results are shown in figure 12a at 1700 UTC with 10-m horizontal wind vectors included. The 2-m temperature results show a cold anomaly over WLIS and ELIS (fig. 12a). The 2-m temperature in WLIS is 22.7˚C, while CLIS and ELIS are respectively 22.4˚C and 20.0˚C. The 2-m temperature over ocean (fig. 12a) is strongly modulated by the surface heat fluxes from the ocean sea temperature (fig. 11a). Over WLIS, the land-sea temperature gradient is 7.1 ˚C, while the land-sea temperature gradient in ELIS is 5.7 ˚C. In addition, a 4.0 m s^{-1}

southwesterly (192˚) 10-m wind along the Connecticut coast has a large 3.9 m s^{-1} onshore component which is an indicator that there is a sea breeze wind present.

3.2.3 HRCoast_night August Model Results

In *HRCoast_night,* the cool biases have been removed. This is because of the realistic coastline that exists in *HRCoast_night*. The initial sea temperature can be seen in figure 10b. In *HRCoast_night*, the sea temperature in WLIS is 22.1˚C, CLIS is 21.5˚C and ELIS is 20.9˚C.

The 2-m temperature results for the *HRCoast_night* is shown in figure 12b for 1700 UTC. 2-m temperature is 24.1˚C in WLIS, 22.4˚C in CLIS and 21.8˚C in ELIS. The land-sea temperature gradient is 5.9˚C in WLIS and 8.2˚C in ELIS. Furthermore, a large onshore component of the 10-m wind of 3.9 m s^{-1} can be seen throughout the Connecticut coast which indicates the presence of a sea breeze wind.

3.2.4 HRCoast_night versus OrigCoast_night Model Results

Notable differences are found between *OrigCoast_night* and *HRCoast_night* for the 21 August 2013 sea breeze event at 1700 UTC (fig. 12c). By initializing the model with a coarse coastline, the 2-m temperature is 1.4 ˚C cooler in WLIS, 0.02˚C cooler in CLIS and 1.7˚C cooler in ELIS. As a consequence, a stronger land-sea temperature gradient exists in the *OrigCoast_night* relative to the *HRCoast_night* in WLIS. With a stronger land-sea temperature gradient, a stronger sea breeze is expected in the *OrigCoast_night* in WLIS.

Differences are also found in the model 10-m wind speed between the *OrigCoast_night* and *HRCoast_night* at 1700 UTC (fig. 12d). By initializing the model with a coarse coastline, the wind speed associated with the sea breeze front is 1.5 m s^{-1} greater than *HRCoast_night*. These wind speed differences are occurring at approximately the same location as the sea breeze front, as indicated by the composite radar images (fig. 8e). These wind differences are adjacent to the

2-m temperature differences. This indicates that the lower 2-m meter temperatures in the *OrigCoast_night* have increased the land-sea temperature gradient, and thus increased the wind speed at the location of the sea breeze front, which is an indicator of a faster sea breeze.

It is important to see if the model sea breeze front is consistent with these 2-m temperature and 10-m wind speed differences. Recall that wind convergence marks the leading edge of the sea breeze front. Figure 12e shows the 54-m wind convergence for *OrigCoast_night* (shaded) and *HRCoast_night* (contoured) for 21 August 2013 1700 UTC. The wind convergence shows strong evidence of a sea breeze front in Connecticut and Long Island Sound for *OrigCoast_night* and *HRCoast_night*. The location of the sea breeze front is verified with the composite radar images (Fig. 7e). When distinguishing the location between the *OrigCoast_night* (shaded) and *HRCoast_night* (contoured), the differences are small in the location of the sea breeze front, most likely because the differences in sea temperature are not large enough to create huge differences in the 2-m temperature (1.7˚C difference) and ultimately the sea breeze front. However, notable differences do exist in WLIS. Although these differences are difficult to detect in figure 11e, the differences are more visible when the *HRCoast_night* wind convergence is subtracted from the *OrigCoast_night* wind convergence (fig. 12f). In western Connecticut, there is a dipole pattern in the wind convergence difference plot (marked in fig. 12f). This indicates that the wind convergence is less in *OrigCoast_night* towards the coastline and greater away from the coastline relative to *HRCoast_night*, which means that the *OrigCoast_night* has progressed more inland than the *HRCoast_night* at this location. This is consistent with the 10-m wind speed and temperature difference plots (fig. 12d), which show a stronger wind for the *OrigCoast_night* in western Connecticut, and the 2-m temperature difference plots (fig. 12d), which show a stronger land-sea temperature gradient for

OrigCoast_night in WLIS. Therefore, by initializing WRF with a coarse coastline at 0300 UTC, the sea breeze front will be slightly stronger in WLIS relative to a case where WRF is initialized with a high resolution coastline (*HRCoast_night).*

3.2.5 Initial Sea Temperature Model Validation for OrigCoast_day and HRCoast_day

OrigCoast_day and *HRCoast_day* have been compared to observations (fig. 13). By properly representing the Long Island Sound with an ocean surface, the sea temperature becomes closer to the buoy observations. In WLIS, the *Origcoast_day* sea temperature is 10.3˚C warmer than observations, while *HRCoast_day* is only 2.7˚C cooler than observations (fig. 13a). In CLIS, *OrigCoast_day* is 3.4˚C cooler than observations, while *HRCoast_day* is 2.8˚C cooler than observations (fig. 13b). In ELIS, *OrigCoast_day* is 10.5˚C warmer than observations, while *HRCoast_day* is only 1.0˚C from observations (fig. 13c).

3.2.6 OrigCoast_day August Model Results

In this section, the *OrigCoast* simulation initialized at 2100 UTC 20 August 2013 (*OrigCoast_day*) will be discussed. The *OrigCoast_day* August results have an anomalously warm WLIS and ELIS during the sea breeze event (fig 14a). This warm anomaly occurs because WLIS and ELIS are being treated as land in the NARR. The land at the initialization time of 2100 UTC (5 PM LT) is warmer than the coastal waters. Since the model is initialized 6 hours earlier than the 0300 UTC *OrigCoast_night* warmer initial sea temperatures values are prescribed in WLIS and ELIS. In WLIS, the sea temperature is 34.8 ˚C, while CLIS and ELIS are respectively 20.5˚C and 30.1˚C in *OrigCoast_day*. The initial sea temperature in WLIS and ELIS are respectively 15˚C and 11.8˚C warmer by initializing the model 6 hours earlier with a coarse coastline, while CLIS is only 1.2˚C cooler (fig.11 and fig. 14).

At 1700 UTC, the 2-m temperature is respectively 28.5˚C and 22.6˚C in WLIS and CLIS,

while ELIS is 26.1˚C in *OrigCoast_day* (fig. 15a). WLIS and ELIS 2-m temperature are 4 ˚C warmer than the surrounding coastal water because of the warm anomaly in the sea temperature. The 10-m wind has a 4.8 m s^{-1} onshore component throughout coastal Connecticut, which is an indicator of a sea breeze wind. Furthermore, the anomalously warm 2-m temperature in WLIS and ELIS results in a weak land-sea temperature gradient of respectively 2.3˚C and 3.2˚C, while CLIS has a stronger land-sea temperature gradient of 7.6˚C.

3.2.7 HRCoast_day August Model Results

In the *HRCoast_day* August results, there is no warm anomaly in WLIS and ELIS (fig. 14b). This is because the ocean is properly being represented as ocean and the land is properly being represented as land in the 2100 UTC initialization. In WLIS, the ocean sea temperature is 21.7˚C while ELIS is 20.6˚C.

In WLIS, the 2-m temperature is 24.5˚C, whereas in CLIS and ELIS, the 2-m temperature is respectively 22.8˚C and 22.2˚C (fig. 15b). The 10-m wind along the Connecticut coast has a 4.2 m s^{-1} onshore component, which is evidence of a sea breeze wind. Furthermore, the land-sea temperature gradient is 6.6˚C in WLIS and 4.8˚C in ELIS. In WLIS and ELIS, this WLIS and ELIS *HRCoast_day* land-sea temperature is greater than the *OrigCoast_day* 2.3˚C WLIS and 3.2˚C ELIS land-sea temperature gradient.

3.2.8 HRCoast_day versus OrigCoast_day Model Results

It is important to find the differences between the two cases so that the impacts of a coarse coastline are made known for a warm (2100 UTC) initialization. By initializing with a coarse coastline, the 2-m temperature is 4 ˚C warmer in WLIS and ELIS than *HRCoast_day* (fig. 15c). These differences are occurring because of the upward surface heat fluxes transferring heat from the strong warm SST anomaly present in the *OrigCoast_day* in WLIS and CLIS. A warmer

2-m air temperature over LIS creates a weaker land-sea temperature gradient. This weaker land-sea temperature gradient suggests that there is a weaker sea breeze in WLIS and CLIS, as well as in southeast coastal Connecticut.

There are large differences in the 10-m wind speed between *OrigCoast_day* and *HRCoast_day*. By initializing with a coarse coastline, the wind speed is about 3 m s^{-1} slower at 15 km inland of eastern coastal Connecticut and 5 km inland in western and central Connecticut (Fig. 15d). These differences in wind speed are occurring at approximately the same location as the sea breeze front, which is verified by the composite radar images (fig. 8e). A slower wind speed by the sea breeze front suggests a weaker wind convergence, thus a weaker sea breeze. In addition, greater wind speeds are evident over ELIS and WLIS relative to *HRCoast_day*. These faster 10-m wind speeds are occurring because since the sea temperature (up to ~42 ˚C) is considerably warmer than the overlying 2-m air temperature (~22 ˚C) in the *OrigCoast_day*, there is a lot of rising air in the surface layer, which enhances mixing and ultimately 10-m wind speed over the Long Island Sound (LaCasse et al. 2008; Crosman and Horel 2010; Steele et al. 2013). It should be noted that these differences between sea temperature and 2-m air temperature do not necessarily guarantee enhanced mixing throughout the depth of the sea breeze, just the lowest 2-m of the sea breeze.

Just like with the cool initialization August sea breeze model runs, it is important to see if the model sea breeze front is consistent with these 2-m temperature and 10-m wind speed differences for the warm initialization August sea breeze model runs. The 54-m wind convergence maps show a sea breeze front 5 km inland of coastal western, central Connecticut and Long Island, and 15 km inland in eastern coastal Connecticut for both cases (Fig. 15e). Unlike for the *HRCoast_night* and the *OrigCoast_night*, there are 8 km differences in the

location of the sea breeze front between *HRCoast_day* (contoured) and the *OrigCoast_day* (shaded; fig 15e). These differences can also be clearly seen in the wind convergence difference maps (fig. 15f). These differences in sea breeze front location occur because the differences between the *HRCoast_day* and the *OrigCoast_day* ocean sea temperature are 2.6˚C greater than the differences between *HRCoast_night* and the *OrigCoast_night* ocean sea temperature in WLIS. By initializing with a coarse coastline, the *OrigCoast_day* sea breeze front is less inland relative to the *HRCoast_day* sea breeze front in west (2 km less inland) and central Connecticut (8 km less inland) as well as far eastern Connecticut (3 km less inland). The difference in sea breeze front location exists in WLIS and CLIS because *OrigCoast_day* is warmer than *HRCoast_day*, which is from the warm anomaly in *OrigCoast_day*, which brings a weaker land-sea temperature gradient. The difference in sea breeze front location exists in far eastern Long Island Sound because the ocean sea temperature is 4˚C warmer than *HRCoast_day*, creating a weaker land-sea temperature gradient. This difference in sea breeze location in west, central and far eastern Connecticut is an indicator that the sea breeze front is weaker in the *OrigCoast_day* than the *HRCoast_day*. Furthermore, wind convergence results are consistent with the 2-m temperature difference with a 3 m s^{-1} weaker wind at the location of the sea breeze front (fig. 15d).

3.3 July Sea Breeze Coastline Sensitivity Experiments

3.3.1 Initial Sea Temperature Model Validation for OrigCoast_night and HRCoast_night

In the 21 August 2013 sea breeze, it was shown that a realistic coastline is important for sea breeze simulations, especially when initialized during the previous day due to larger coastal temperature gradients. It is important to test the robustness of the results of the 21 August 2013 sea breeze event by examining other sea breeze events. In this study, the 08 July 2013 sea breeze

will also be analyzed.

Figure 16a-c shows 18-hr time series for the WLIS, CLIS and ELIS buoys with similar convention as figure 10 but for the 08 July 2013 sea breeze. In WLIS, the *OrigCoast_night* sea temperature is 4.8˚C higher than observations during the sea breeze. The *HRCoast_night* sea temperature is 0.9˚C from buoy observations in WLIS during the sea breeze (fig. 16a). In CLIS, *OrigCoast_night* and *HRCoast_night* are respectively 0.9˚C and 0.7˚C cooler than observations (fig. 16b). Just like for the August sea breeze event, since the ocean is being represented properly in both simulations in this particular region, it is expected that the sea temperatures are similar. In ELIS, *OrigCoast_night* is 3.3˚C warmer than observations while *HRCoast_night* is 2.5˚C warmer than observations during the sea breeze event. These initial results indicate that the 08 July 2013 sea breeze *HRCoast_night* simulation uses a more realistic SST, which could potentially produce a more realistic simulated sea breeze.

3.3.2 OrigCoast_night Model Results

In the *OrigCoast_night* for the July case, there is no cool anomaly like there was for the *OrigCoast_night* August case in WLIS (fig 17a and fig. 11a). This is because the day prior to the July sea breeze was a very warm 48˚C. Even with radiative cooling from sunset to 0300 UTC, the land temperature still exceeds the sea temperature by 6˚C at 0300 UTC 08 July 2013 (2300 LST). Therefore, instead of a cool anomaly, there is a warm anomaly in WLIS (fig. 17a). In WLIS, the sea temperature of the warm anomaly is 26.6˚C, while in ELIS the sea temperature is 22.6˚C.

At 1700 UTC, the overlying 2-m temperature is 29.0˚C in WLIS and 24.1˚C in ELIS. In addition to a notable 4.9 m s^{-1} onshore sea breeze wind component along the Connecticut coast, there is also a 2.9 m s^{-1} westerly wind component.

3.3.3 HRCoast_night Model Results

In the *HRCoast_night*, there is no warm anomaly (fig. 17b). This is because the ocean is correctly being represented as ocean in the WLIS, therefore the warm urban heat Island has little influence on WLIS. Instead, the sea temperature is relatively uniform throughout the Sound with a sea temperature of 22.7˚C, 22.6˚C and 21.8˚C in WLIS, CLIS and ELIS, respectively.

The 2-m temperature is also relatively uniform in Long Island Sound because of the weak horizontal 0.9˚C SST gradient in the underlying sea temperature. In WLIS, CLIS and ELIS, the 2-m temperature is respectively 26.6˚C, 24.9˚C and 23.5˚C (fig. 18b). Similar to the *OrigCoast_day*, in addition to a strong 5.1 m s^{-1} onshore component to the 10-m wind over Long Island Sound and coastal Connecticut, there is also a 3.0 m s^{-1} synoptic westerly wind.

3.3.4 HRCoast_night versus OrigCoast_night Model Results

The differences between the *OrigCoast_night* and the *HRCoast_night* for the July sea breeze event are explored at 1700 UTC (fig. 18). The *OrigCoast_night* 2-m temperature for WLIS, CLIS and ELIS are respectively 2.4˚C warmer, 0.02˚C cooler and 0.56˚C warmer than *HRCoast_night* (fig. 18c). These differences are relatively small because the differences in the sea temperature are small (fig. 17a-b). When a high resolution coastline was used, the LIS sea temperature did not change substantially compared to simulations using the coarse coastline. Therefore, when the land-sea temperature gradient at the initialization time is weak like for this July example and the previous August example, sea temperatures do not substantially change when the NARR coastline is modified to 1 km. With no greater than 2.5˚C differences in 2-m temperature, there are expected to be relatively small differences in the July sea breeze front position between *HRCoast_night* and *OrigCoast_night* simulations. The differences in wind speed are 0.2 m s^{-1} throughout the Long Island Sound and 1.0 m s^{-1} at the location of the sea

breeze front (fig. 18d).

At 1700 UTC, the sea breeze front is visible in the wind convergence maps in both the *HRCoast_night* and *OrigCoast_night* (fig. 18e). The sea breeze front in the model runs are 5 km further inland from the observations in the corresponding visible satellite image at 1700 UTC (fig. 9b). There are negligible differences in the location of the sea breeze front between *HRCoast_night* (contoured) and *OrigCoast_night* (shaded) due to the relatively small differences in coastal temperature gradients between the two simulations (fig. 18e). Furthermore, the wind convergence difference results show no dipole patterns along the sea breeze front, which further indicates that the difference in sea breeze front position between *HRCoast_night* and *OrigCoast_night* is small (fig. 18f).

3.3.5 Initial Sea Temperature Model Validation for July warm coastline sensitivity experiment

The *HRCoast_day* and *OrigCoast_day* simulations are also explored for the 08 July sea breeze. Figure 18a-c shows 24-hr time series for the WLIS, CLIS and ELIS buoys with similar convention as figure 13 but for the 08 July 2013 sea breeze. In WLIS, the *OrigCoast_day* sea temperature is 25.2˚C higher than observations during the sea breeze (fig. 19a). The *HRCoast_day* sea temperature is 0.7˚C higher than buoy observations in WLIS during the sea breeze (fig. 19a). In CLIS, *OrigCoast_day* is 1.9˚C lower than observations and *HRCoast_day* is 1.3˚C lower than observations (fig. 19b). Unlike ELIS and WLIS, since the ocean is being represented properly in both *OrigCoast_day* and *HRCoast_day* simulations in this particular region, it is expected that the sea temperatures are similar in CLIS. In ELIS, *OrigCoast_day* is 21.8˚C higher than observations while *HRCoast_day* is 2.3˚C higher than observations during the sea breeze event (fig. 19c). These initial results indicate that the 08 July 2013 sea breeze *HRCoast_day* simulation uses a considerably more realistic SST, which could potentially

produce a more realistic sea breeze.

3.3.6 OrigCoast_day Model Results

For the *OrigCoast_day*, there is large horizontal gradient in the sea temperature (fig. 20a), where CLIS sea temperature is 22˚C, while ELIS and WLIS are at a very warm, respective 47˚C and 41˚C, due to WLIS and ELIS being treated as land in the initial conditions. The land is very warm at 2100 UTC (1700 LST) because it is close to the diurnal heating maximum in the day prior to the sea breeze. In addition, there is an urban heat island effect occurring from New York City.

In response to the warmer SSTs, the WLIS 2-m temperature is 32.2˚C while the ELIS 2-m temperature is 30.5˚C at 1700 UTC (fig. 21a). Similar to *OrigCoast_night*, there is a 5.8 onshore, southerly sea breeze wind in addition to a 4.3 m s^{-1} westerly, synoptic wind.

3.3.7 HRCoast_day Model Results

There is a smaller horizontal SST gradient in the sea temperature in *HRCoast_day* compared to *OrigCoast_day*. The sea temperature in WLIS is 22.5˚C, CLIS is 22.6˚C and ELIS is 21.6˚C (fig. 20b). There is a small SST gradient in the sea temperature because the coastline is being properly represented in the initial conditions.

The 2-m temperature at 1700 UTC is relatively uniform like the sea temperature. In WLIS and CLIS, the 2-m temperature is respectively 25.8˚C and 24.2˚C whereas in ELIS the 2-m temperature is 23.6˚C (fig. 21b). The 10-m southerly, sea breeze wind along the Connecticut coastline is 5.2 m s^{-1}.

3.3.8 HRCoast_day versus OrigCoast_day Model Results

The results of the two model simulations will be compared so that the impacts of an accurate coastline can be explored. The differences in 2-m temperature at 1700 UTC are

relatively large, especially in WLIS (fig. 21c). By initializing WRF with a coarse coastline, the 2-m temperature is respectively 6.6˚C and 6.9˚C warmer in WLIS and ELIS, reducing the land-sea temperature gradient, promoting a weaker sea breeze circulation.

There are also large changes in the 10-m wind speed (fig. 21d). In WLIS and ELIS, the wind speed is 5.0 m s^{-1} greater by initializing with a coarse coastline. These higher wind speeds exist because of the very warm sea temperature (47˚C WLIS and 41˚C ELIS) underlying a cooler 2-m temperature (32.2˚C WLIS and 30.5˚C ELIS) in the *OrigCoast_day*. When the sea temperature is much greater than the 2-m temperature, an unstable surface layer is achieved which causes a lot of mixing and ultimately greater wind speeds near the surface. There are no notable differences in the 10-m wind at the CT sea breeze front. Therefore, the differences in sea breeze location should mainly be contributed by the land-sea temperature gradient difference explained above.

The sea breeze front is evident in both the *HRCoast_day* (contoured) and the *OrigCoast_day* (shaded) wind convergence maps as well as the wind convergence difference maps (fig. 21e-f). Results show that the *HRCoast_day* sea breeze front has progressed from 5 km to 8 km further inland than the *OrigCoast_day* sea breeze front in west Connecticut and east Connecticut. The *OrigCoast_day* sea breeze front has not progressed as far because of the weaker land-sea temperature gradient. The land-sea temperature gradient is weaker in the *OrigCoast_day* because of the warmer LIS sea temperature relative to the *HRCoast_day*.

3.4 August Sea Breeze SST Sensitivity Experiment

3.4.1 Introduction and Initial Model Validation

It has been shown that a coarse coastline can have a large impact on sea breezes, especially when the sea breeze is initialized during the previous day. The Long Island Sound

SST structure is complex where the resolution of the SST product becomes important (fig. 5c and fig. 6c). Thus, SST resolution is another model constraint whose impacts need to be studied. The impact of SST resolution is examined by performing 3 sensitivity experiments; uniform SST, 32 km NARR SST and 1 km G1SST.

The model sea temperature is validated with buoy observations from WLIS, CLIS, and ELIS (fig. 22). By increasing the SST resolution, the model sea temperature becomes closer to buoy observations. In ELIS at 1500 UTC, model sea temperature is 2.3˚C cooler than the observed SST when initializing with the uniform SST. When initializing with the NARR SST, ocean sea temperature is a 1.8˚C cooler than the observations. Using the G1SST, the ocean sea temperature is 1.2˚C cooler than observations. These initial results indicate that by increasing the resolution of the SST product used to initialize the model, a more accurate SST and potentially a more accurate sea breeze is achieved.

3.4.2 SST uniform sensitivity experiment

Recall that the SST uniform case has a spatially uniform SST of 22˚C throughout Long Island Sound for the August sea breeze case (Fig. 23a). This uniformity contributes to a 2-m temperature with little spatial variation throughout the Long Island Sound and Block Island Sound at 1500 UTC through surface heat fluxes (fig. 23b). In ELIS, CLIS and WLIS at 1500 UTC, the 2-m temperature is respectively 21.9 ˚C, 21.6˚C and 22.5˚C (fig. 23b). The relatively warm 2-m WLIS 2-m temperature is likely due to warm air advection from Long Island as suggested by the southerly wind in Long Island and the downward surface heat fluxes, which will be examined in more detail. The 10-m wind at 1500 UTC has a 4 m s^{-1} onshore component throughout coastal Connecticut, indicating the presence of sea breeze wind.

At 1600 UTC, WLIS, CLIS and ELIS have respectively warmed to 23.1˚C, 22.3˚C and

21.7˚C (fig. 23e). Given that the SST remains temporally static throughout the model run, the sea temperature variations are not the main reason for the 2-m temperature temporal increase. The land temperature responds to the varying insolation, which directly impacts the 2-m temperature. Therefore, the warming is likely due to southwesterly warm air advection from Long Island. By 1700 UTC, the 2-m temperature in WLIS reached 24.1˚C (fig. 23h). The coastal CT sea breeze wind remains southwesterly at 5 m s^{-1} between 1600-1700 UTC.

It is important to understand how the surface heat fluxes evolve during the sea breeze so that it is further understood how the 2-m temperatures mentioned prior are impacted by the uniform SST. Figure 23c, 23f, and 23i shows sensible heat flux for 1500 UTC, 1600 UTC and 1700 UTC, respectively. For the uniform simulation, the sensible heat flux is -0.23, 2.42 and 1.18 W m^{-2} at 1500 UTC for WLIS, CLIS and ELIS, respectively (fig. 22c). By 1600 UTC, the CLIS sensible heat flux becomes negative. WLIS, CLIS and ELIS are -0.7, -0.8 and 0.02 W m^{-2}, respectively at 1600 UTC (fig. 23f). At 1700 UTC, the sensible heat flux becomes more negative throughout LIS, where values are respectively -1.6, -2.3 and -3.2 W m^{-2} in WLIS, CLIS and ELIS (fig. 23i). These results indicate that during the duration of the sea breeze, the transfer of heat changes from upward to downward when assuming a static ocean. This change in sign of sensible heat flux is likely because of the ongoing warm air advection from Long Island. From 1500 UTC to 1700 UTC, the overlying air temperature (θ_a) increases 4.0˚C, 2.1˚C and 0.6˚C respectively in WLIS, CLIS and ELIS (table 3). Given that the potential sea temperature (θ_g) is nearly static and that θ_a is increasing from 1500 UTC to 1700 UTC (table 3), it is deduced that the 54-m air temperature is driving the change in sign in sensible heat flux indicating warm air advection. It should be noted that although the *in situ* sea temperature is spatially uniform, the potential sea temperature has slight spatial variations. In the uniform SST simulation, the

potential sea temperature spatial variations are contributed by the surface pressure spatial variations. The warm air advection is also evident in the 10-m wind results, where warm air is blowing from Long Island towards the Sound (fig. 23b,e,h). This warm air advection causes the air aloft to be warmer than the air near the surface. When less dense air overlays cooler less dense air, there is a downward heat transfer and thus a negative sensible heat flux.

The temporal latent heat flux variations are relatively small between 1500 UTC and 1700 UTC in the uniform, NARR and G1SST simulations (fig.23d,g,j). The spatial variation, however, is evident in the latent heat flux from 1500 UTC to 1700 UTC for all three SST model runs. At 1500 UTC in the uniform simulation, the latent heat flux is 9.5 W m^{-2} in WLIS, 36.1 W m^{-2} in CLIS and 43.3 W m^{-2} in ELIS (fig. 23d). At 1600 UTC, the latent heat flux is 5.9 W m^{-2} in WLIS, 41.4 W m^{-2} in CLIS and 48.1 W m^{-2} in ELIS (fig. 23g). At 1700 UTC, the latent heat flux is 7.2 W m^{-2} in WLIS, 21.7 W m^{-2} in CLIS and 50.1 W m^{-2} in ELIS (fig. 23j). The reason why the latent heat flux is so large in ELIS as well as all of coastal Connecticut is because of the strong sea breeze wind (eq.3; fig. 23b-d). The reason why the latent heat flux is so small in WLIS and CLIS towards the Long Island coast is because of the weak wind. The reduced wind is in part due to a northerly wind over southern LIS generated due to the developing sea breeze convergence boundary over Long Island (fig. 26a). The northerly wind opposes the regionally dominant southwesterly wind, reducing the value of the 10-m wind over southern LIS (fig. 23b,e,h).

3.4.3 NARR sensitivity experiment

Initializing the model with the moderate resolution NARR SST, an east-west spatial gradient is introduced in the Long Island Sound. In WLIS, the sea temperature is 22.6˚C, decreasing eastward to 21.4˚C at the mouth of the Long Island Sound (fig. 24a). The 2-m

temperature responds to this spatial SST gradient through surface heat fluxes.

By 1500 UTC, the 2-m temperature is 22.7˚C in WLIS, 21.6˚C in CLIS, and 21.4˚C in ELIS. The local maximum in warm 2-m temperature in WLIS is due to the upward surface heat fluxes transferring heat from the warmer sea temperature in WLIS, but also partly due to warm air advection. In Block Island sound, the 2-m temperature is a relatively cool 21˚C, which is because of the cool sea temperature in Block Island Sound (fig. 24a-b).

At 1600 UTC, WLIS continues to warm due to surface fluxes when air is cooler than the SST and warm air advection. WLIS is 23.4˚C while ELIS and Block Island Sound are around and 21.7˚C (fig. 24c). CLIS also warms because of warm air advection from Long Island. At 1700 UTC, the 23˚C isotherm extends towards the center of Long Island sound, which indicates continuing upward surface heat fluxes and warm air advection between 1600 UTC and 1700 UTC (fig. 24d). The 2-m temperature of ELIS increases only 0.4˚C between 1500 UTC and 1700 UTC which is because of the relatively small turbulent surface heat flux and absence of warm air advection.

In the NARR, a similar temporal evolution occurs in the surface heat fluxes as the uniform. At 1500 UTC sensible heat flux is -0.4 W m^{-2} in ELIS, 2.3 W m^2 in CLIS and 0.04 W m^{-2} in WLIS (fig. 24c). At 1600 UTC, the sensible heat flux drops to -2.2 W m^{-2} in ELIS, -2.6 W m^{-2} in CLIS and -0.5 W m^{-2} in WLIS (fig. 24f). At 1700 UTC, the sensible heat flux is -3.8 W m^{-2} in ELIS, -2.7 W m^{-2} in CLIS and -2.1 W m^{-2} in WLIS (fig. 24i)

Similar spatial and temporal patterns occur in the NARR for the latent heat flux as well (fig. 24d,g,j). At 1500 UTC, the latent heat flux is 13.1 W m^{-2} in WLIS, 35.4 W m^{-2} in CLIS and 34.3 W m^{-2} in ELIS (fig. 24d). At 1600 UTC, latent flux increases to 39.8 W m^{-2} in ELIS, while WLIS and CLIS respectively are 5.7 W m^{-2} and 42.7 W m^{-2} (fig. 24g). At 1700 UTC, the latent

heat flux decreases to 33.1 W m^{-2} in ELIS, while WLIS and CLIS are 10 W m^{-2} and 21.4 W m^{-2}, respectively (fig. 24j).

3.4.4 NARR versus Uniform

By adding a moderate SST gradient, there are relatively small changes. At 1500 UTC, the 2-m temperature is 0.2˚C warmer than the uniform simulation in WLIS and 0.5˚C cooler than the uniform simulation in ELIS (fig. 25d). The SST is warmer in WLIS because of the 0.5˚C warmer SST in the NARR, and cooler in ELIS because of the 0.7˚C cooler SST in the NARR. The 2-m temperature differences between the NARR and uniform are a relatively small 0.75˚C because the sea temperature changes very little when an SST gradient is added to Long Island Sound, especially in CLIS where the NARR is only 0.02˚C cooler than the uniform. At 1600 UTC, the 2-m temperature difference between NARR and the uniform is 0.3˚C warmer in WLIS, 0.003˚C warmer in CLIS, and 0.4˚C cooler in ELIS (fig. 25h). At 1700 UTC, the temperature differences are 0.3˚C warmer in WLIS, 0.02˚C warmer in CLIS, and 0.5˚C cooler in ELIS (fig. 25l). Little change in the 2-m temperature means that there is little change in the land-sea temperature gradient. This suggests that there will be relatively little change in the sea breeze strength when adding an SST gradient.

The surface heat flux differences allow the sea temperature differences to modulate the 2-m temperature differences. Therefore, it is important to explore the surface heat flux differences between the NARR and uniform to further understand the 2-m temperature differences. The surface heat fluxes have changed substantially by increasing the SST resolution (fig. 25b,c,f,g,j,k). The changes in surface heat flux will be evaluated at 1500 UTC because the least temperature advection has taken place, which will allow us to evaluate the changes in fluxes primarily contributed by the changes in SST, and not disturbed by temperature advection (fig.

25b-c). At 1500 UTC, the NARR has a sensible heat flux 0.3 W m^{-2} (120%) greater than the uniform in WLIS, 0.1 W m^{-2} (4%) greater in CLIS and 1.6 W m^{-2} (133%) less in ELIS (fig. 25b). In ELIS, the sensible heat flux becomes more negative as the SST resolution increases because of the cooler SST in the NARR. A cooler SST results in a more negative temperature difference between the surface and air aloft, ultimately causing a more negative (downward) sensible heat flux (eq. 3; table 4). In WLIS and CLIS, the sensible heat flux becomes more positive as SST resolution increases because of the warmer SST in the NARR. A warmer SST results in a greater positive temperature difference between the surface and air aloft, ultimately causing a larger positive (upward) sensible heat flux (eq. 3, table 4).

For latent heat flux, NARR is 3.6 W m^{-2} (37.8%) greater than the uniform in WLIS, 0.7 W m^{-2} (1.9%) less in CLIS, and 9.0 W m^{-2} (20.8%) less in ELIS (fig. 25c). The latent heat flux is increasing with increasing SST resolution in WLIS primarily because of the surface mixing ratio differences (eq. 4; table 5). It is important to understand that the moisture content is saturated at the ocean surface, therefore the moisture content is directly modulated by the sea temperature. A larger mixing ratio difference is occurring because of the warmer NARR sea temperature in WLIS (fig 25a). Since the surface mixing ratio differences are directly modulated by the sea temperature differences, the surface mixing ratio increases between the NARR and uniform, which allows the difference between the surface specific humidity and the first model level (54-m) mixing ratio to become larger when using the NARR in WLIS (eq. 4; table 5). In ELIS, the NARR latent heat flux is less than the uniform latent heat flux because q_g-q_a is less in the NARR, which is due to the smaller surface mixing ratio associated with the cooler sea temperature (eq. 4; table 5).

Adding an SST gradient brings small differences, less than 0.5 m s^{-1}, in the 10-m wind

speed in Long Island Sound. At 1500 UTC, there are notable changes in wind speed in west, central and far eastern Connecticut (CT) at 10 km north of the coastline (fig. 25e). The wind speeds at western and central CT are 0.75 m s^{-1} slower than the uniform. The wind speeds in far eastern CT are 0.7 m s^{-1} faster than the uniform. These relatively large wind speed differences are occurring along the sea breeze front, as verified by the composite radar images (fig. 8). This suggests that the NARR sea breeze front is in a different position than the uniform sea breeze front.

As mentioned earlier, the difference in 2-m temperature and 10-m wind are relatively small when the NARR (with a moderate SST gradient) is compared to the uniform (with no SST gradient). Based on these difference plots, differences in sea breeze front location should be most evident at CLIS and WLIS for 1500 UTC. Otherwise, differences in sea breeze front location will be dominated by terrain influences present at 1600 UTC and 1700 UTC. Terrain influences will make it difficult to detect differences in sea breeze front location due to differences in land-sea temperature gradient. Due to this limitation, only 1500 UTC wind convergence will be analyzed.

The wind convergence maps show evidence of a sea breeze front throughout coastal Connecticut for the NARR and uniform case at 1500 UTC (fig. 26a). At 1500 UTC, there is a notable difference in sea breeze location in throughout coastal Connecticut (fig. 26a,b). The NARR case (contoured) is 1.5 km closer to the coastline than the uniform case (shaded) in west Connecticut (fig. 26a,c,d), indicating that the modeled sea breeze propagation is slower when initialized with the NARR SST. In addition, the NARR sea breeze front is 1 km further inland than the uniform sea breeze front in ELIS, indicating the modeled sea breeze propagation is aster when initialized with the NARR SST (fig. 26h). The difference in sea breeze position is also

clearly seen in the wind convergence difference map (fig. 26b). Along the CT sea breeze front, a dipole pattern can be seen in the color shading. In western and central CT, the NARR wind convergence is $3x10^{-4}$ s^{-1} greater towards the coast and $2x10^{-4}$ s^{-1} less away from the coast relative to the uniform. This indicates that the NARR sea breeze front is closer to the coast than the uniform sea breeze front. In eastern CT, the dipole pattern is opposite, where the wind convergence is $1.5x10^{-4}$ s^{-1} greater away from the coast and $1.5x10^{-4}s^{-1}$ less towards the coast. This indicates the NARR sea breeze front is further inland than the uniform sea breeze front. The difference in sea breeze front position in WLIS and CLIS is consistent with the 10-m wind speed difference plots, which show a slower wind speed relative to the uniform in western and central CT and a stronger wind speed in eastern CT (fig. 25e).

3.4.5 G1SST sensitivity experiment

Using the G1SST, WLIS and CLIS sea temperature are respectively 23.2˚C and 22.7˚C (fig. 27a), both regions 0.6˚C warmer than the NARR SST (fig. 27a). The sea temperature ELIS is 20.1˚C (fig. 27a), and 1.3˚C cooler than the NARR (fig. 25a). In the G1SST, there is a 3.1˚C horizontal SST gradient, whereas in the NARR there is only a 1.5˚C horizontal SST gradient.

The 2-m temperature at 1500 UTC is warmest in WLIS at 22.8˚C (fig. 27b). This warm 2-m air temperature in WLIS exists because of the underlying warm sea temperature and warm air advection from Long Island. At the mouth of Long Island Sound, the 2-m temperature is at a cooler 20.8˚C. There's a sharp horizontal gradient in the 2-m temperature at the mouth due to the underlying horizontal gradient in the sea temperature from the high resolution SST. Furthermore, the results show a 5 m s^{-1} onshore wind along the Connecticut coastline which indicates the presence of a sea breeze wind, which is also present in 1600 UTC and 1700 UTC.

At 1600 UTC, the 2-m temperature is over the water warms, especially in the head of

Long Island Sound (fig. 27e). In WLIS, the 2-m temperature is at a relatively warm 24.1˚C, which is due to the underlying warm sea temperature and warm air advection. In CLIS, the sea temperature warms to 22.8˚C. This is mainly due to the underlying 23˚C warm sea temperature. In ELIS, the 2-m temperature is 21.2˚C.

At 1700 UTC, WLIS and CLIS continue to respectively warm to 24.8˚C and 23.2˚C, while the 2-m temperature over Block Island Sound remains relatively constant (21.3˚C; fig. 27h). This is because the underlying sea temperature is cooler, therefore upward surface heat fluxes are very small, which will be examined later. Overall, the combination of these SST influences causes the 2-m horizontal gradient to increase in WLIS between 1500 UTC and 1700 UTC.

Sensible heat flux in the G1SST evolves similarly as the NARR and uniform throughout the duration of the sea breeze. The sensible heat flux in the G1SST is -3.6 W m^{-2} in ELIS, 2.9 W m^{-2} in CLIS and 0.6 W m^{-2} in WLIS at 1500 UTC (fig. 27c). At 1600 UTC, the sensible heat flux is -7.6 W m^{-2} in ELIS, -0.7 W m^{-2} in CLIS and 1.3 W m^{-2} in WLIS (fig. 27f). At 1700 UTC, ELIS is -6.0 W m^{-2}, while CLIS and WLIS are respectively -2.5 and -1.8 W m^{-2} (fig. 27l). In the G1SST, the sensible heat flux becomes negative earlier in ELIS and later in WLIS than the uniform (fig. 27c,f,h and fig. 24c,f,h). This is because of the cooler SST in ELIS and warmer SST in WLIS relative to the uniform.

In the 1500 UTC G1SST simulation, very unlike the uniform and NARR, ELIS has a latent heat flux of 14.2, 15.4 and 12.1 W m^{-2} at 1500 UTC, 1600 UTC and 1700 UTC, respectively (fig. 27d,g,j). Like the NARR and G1SST ELIS, the wind remains 4.5 to 5 m s^{-1}, which means that the low latent heat flux in the G1SST ELIS cannot be because of the wind. The reason why the latent heat flux is so low in ELIS in is because of the smaller difference in

specific humidity between the surface and air aloft compared to CLIS and WLIS (eq.3; table 7). This indicates that there is a smaller difference in specific humidity between the surface and the overlying air at ELIS compared to CLIS and WLIS because of the cool 19˚C ELIS sea temperature in the G1SST. In CLIS and WLIS, the G1SST latent heat flux temporal and spatial evolution is relatively similar to the NARR and uniform (fig. 27d,g,j). At 1500 UTC, the latent heat flux is 21.8 W m^{-2} in WLIS and 39.9 W m^{-2} in CLIS. At 1600 UTC, WLIS is 19.5 W m^{-2} while CLIS increases to 48.6 W m^{-2}. At 1700 UTC, WLIS is 11.3 W m^{-2} and CLIS is 29.9 W m^{-2}.

3.4.6 G1SST versus Uniform

The 2-m temperature differences between the G1SST and uniform are large where there are large differences in sea temperature between the G1SST and uniform products (fig.28a,d,h,l). By using a high resolution SST product, the 2-m temperature is 0.42˚C higher in WLIS and CLIS, and 1.2˚C lower in ELIS at 1500 UTC (fig. 27d). These differences increase in WLIS and CLIS with respect to time (fig.28d,h,l). At 1700 UTC the differences are 0.5˚C in CLIS and -1.3˚C in ELIS (fig.27l). The differences in these regions increase because in the G1SST (23˚C), there is a greater upward surface heat flux in CLIS and a smaller surface heat flux in ELIS (fig. 28).

At 1500 UTC, the G1SST has a sensible heat flux 0.8 W m^{-2} (400%) greater than the uniform in WLIS, 0.5 W m^{-2} (21%) greater in CLIS, and 4.7 W m^{-2} (-400%) less in ELIS (fig. 28b,f,j). The sensible heat flux differences between the G1SST and uniform are occurring for the same reasons as the sensible heat flux differences between the NARR and uniform, except that the differences are amplified between the G1SST and uniform because of the larger temperature between the surface and air aloft from the warmer G1SST sea temperature in WLIS and CLIS

and the cooler SST in ELIS (eq.2; table 6).

The G1SST latent heat flux is 12.3 W m^{-2} (129.7%) greater than the uniform in WLIS, 3.8 W m^{-2} (10.5%) greater in CLIS, and 29.1 W m^{-2} (67%) less in ELIS (fig.28c,g,k). The latent heat flux is increasing with increasing SST resolution in WLIS because of the larger positive moisture difference from the larger surface specific humidity from the warmer SST (eq.3; table 7). The latent heat flux is decreasing with increasing SST resolution in ELIS because of the cooler SST in the higher resolution SST products. A cooler SST results in a smaller surface specific humidity and thus the difference between the surface and the model first level specific humidity decreases, resulting in a smaller latent heat flux.

Using the G1SST, the wind speed changes are relatively small between the G1SST and uniform simulations over Long Island Sound (fig. 28e,i,m). The only changes in wind that might be associated with the change in sea breeze front location occur at 1500 UTC (fig. 28e). By increasing the SST resolution, the wind speed decreases 1 m s^{-1} along sea breeze front at 1500 UTC for west and central Connecticut, indicating a difference in sea breeze position between the G1SST and uniform. 0.75 m s^{-1} 10-m wind speed increases occur in the eastern Connecticut sea breeze front also indicating a difference in sea breeze position between the G1SST and uniform.

There are notable differences in the sea breeze front position in WLIS, CLIS and ELIS between the G1SST and the uniform at 1500 UTC (fig. 29). In WLIS, the G1SST (contoured) is 2 km closer to the coastline relative to the uniform model run (shaded; fig.29a,c,d). In CLIS, the G1SST sea breeze front is 1.5 km closer to the coastline, and the sea breeze front at ELIS is 1 km further from the coastline. The wind convergence difference maps also indicate that the G1SST sea breeze front is less inland than the uniform sea breeze front in WLIS and CLIS, and further inland in ELIS (fig. 29b). These differences in sea breeze position exist because the G1SST has a

weaker land-sea temperature gradient in WLIS and CLIS and a stronger land-sea temperature gradient in ELIS relative to the uniform. At 1600 UTC and 1700 UTC when the sea breeze front gets inland enough, the sea breeze front in the uniform and G1SST are both affected by terrain and friction which it makes it difficult to detect whether the G1SST sea breeze front is further or less inland than the uniform.

3.5 July Sea Breeze SST Sensitivity Experiment

3.5.1 Introduction and Initial Model Validation

In this section, these impacts of SST resolution on sea breeze will be verified by studying the 08 July 2013 sea breeze event. Just like with the 21 August 2013 sea breeze, the model sea temperature is validated with buoy observations from WLIS, CLIS, and ELIS (fig. 30). By increasing the SST resolution, the model sea temperature becomes closer to buoy observations. In ELIS at 1500 UTC, model sea temperature is 3.5˚C warmer than the observed SST when initializing with the uniform SST. When initializing with the NARR SST, sea temperature is a 2.7˚C warmer than the observations. Using the G1SST, the sea temperature is 2.2˚C cooler than observations. These initial results indicate that by increasing the resolution of the SST product used to initialize the model, a more accurate SST and potentially a more accurate sea breeze is achieved.

3.5.2 SST Uniform Sensitivity Experiment

In the 08 July 2013 uniform SST sensitivity experiment, the sea temperature is 22.4˚C throughout the Long Island Sound (fig. 31a). As time progresses, WLIS 2-m temperature increases from 24.6 ˚C at 1500 UTC to 25.9˚C at 1700 UTC, which is due to warm air advection from Long Island as indicated by the westerly strong 8 m s^{-1} 10-m winds over New York City (fig. 31b,e,h). In ELIS, the 2-m temperature is 23.3˚C at 1500 UTC and 23.7˚C at 1700 UTC. In

addition, the uniform case has a persistent synoptic westerly wind along coastal Connecticut as well as a southerly sea breeze wind.

The surface heat fluxes help explain why the 2-m temperature is warmer than the sea temperature. At 1500 UTC, the sensible heat flux is -5.1 W m^{-2} in WLIS, -7.8 W m^{-2} in CLIS and -8.6 W m^{-2} in ELIS (fig. 31c). Unlike the 21 August 2013 sea breeze, the sensible heat flux is downward towards to the ocean at 1500 UTC. This is because of warm air advection from the strong 8 m s^{-1} southwesterly wind from Long Island (fig. 31b). Also unlike the 21 August 2013 sea breeze, warm air advection is a more important factor in this sea breeze because of the stronger wind that exists throughout Long Island, LIS, and CT (~8 m s^{-1}) compared to the 21 August 2013 sea breeze (~4 m s^{-1}; fig 23b). The stronger wind brings more warm air to the Long Island Sound region, hence the highly negative sensible heat flux in the 08 July 2013 uniform compared to the 21 August 2013 uniform at 1500 UTC (-0.2 W m^{-2} in WLIS; 2.4 W m^{-2} in CLIS; 1.2 W m^{-2} in ELIS for 21 August 2013). The sensible heat flux becomes more negative for 1600 UTC and 1700 UTC throughout LIS because of the continuing warm air advection from Long Island (fig. 31f,i). The latent heat flux at 1500 UTC is 11.5 W m^{-2} in WLIS, 23.6 W m^{-2} in CLIS, and 21.6 W m^{-2} in ELIS. The latent heat flux increases with respect to time especially in CLIS due to increasing wind speed (fig.31b,e,h,g,h).

3.5.3 NARR Sensitivity Experiment

In the NARR, the sea temperature is 22.5˚C in WLIS (fig. 32a) decreasing eastward to 21.6 ˚C in ELIS. The SST gradient is 0.8˚C, which is 0.7˚C smaller than the 21 August 2013 event for the NARR (1.5 ˚C). Despite this horizontal SST gradient, there remains a relatively small horizontal gradient in the 2-m temperature at 1500 UTC through 1700 UTC (fig.32b,e,h). The small horizontal 2-m temperature gradient that does exist is mainly contributed by warm air

advection in WLIS, as indicated by the southwesterly winds in Long Island and New York City (fig. 32b,e,h). The 10-m wind has a very similar direction and magnitude as the control from 1500 to 1700 UTC.

Even with an SST gradient added, the surface heat fluxes remain relatively similar across Long Island Sound because of the strong role of warm air advection from Long Island and the relatively weak SST gradient in the NARR SST. At 1500 UTC, the sensible heat flux is -5.4 W m^{-2} in WLIS, -7.8 W m^{-2} in CLIS, and -12.3 W m^{-2} in ELIS (fig. 32c). At 1600 and 1700 UTC, the sensible heat flux becomes more negative for the same reasons as the uniform (fig. 32f,i). The latent heat flux at 1500 UTC is 10.9 W m^{-2} in WLIS, 23.8 W m^{-2} in CLIS, and 9.2 W m^{-2} in ELIS. The latent heat flux increases with respect to time for the same reasons as the uniform (fig.32b,e,h,g,h).

3.5.4 NARR versus Uniform

By increasing the resolution of the SST to 32 km, there are negligible changes in 2-m temperature over Long Island Sound that do not exceed 0.25˚C between 1500 UTC and 1700 UTC (fig. 33d,h,l). In ELIS, however, the 2-m temperature decreases 0.4˚C at 1500 UTC through 1700 UTC, due to the cooler sea temperature in the NARR relative to the uniform form the differences in surface heat fluxes (fig. 33a). Furthermore, changes in 10-m wind speed along the sea breeze front are less than 0.5 m s^{-1}, which is considered small (fig. 33e,i,m).

Changes occur between the NARR and uniform in the surface heat fluxes that explain the changes in the 2-m temperature. At 1500 UTC, the sensible heat flux decreases 0.3 W m^{-2} (-6%) in WLIS, 0.0 W m^{-2} (0%) in CLIS, and decreases 3.7 W m^{-2} (43%) in ELIS (fig. 33b). The NARR latent heat flux decreases the most in ELIS relative to the uniform because the relatively large 0.75˚C decrease in sea temperature (fig. 33a). The sensible heat flux differences are small

in WLIS and CLIS because of the small difference in sea temperature between the NARR and uniform, which means the changes in θ_g-θ_a are also small (fig. 33a; table 8). The latent heat flux at 1500 UTC decreases 0.6 W m^{-2} (5%) in WLIS, increases 0.2 W m^{-2} (1%) in CLIS, and decreases 12.4 W m^{-2} (57%) in ELIS (fig. 33c). The latent heat flux decreases the most in ELIS because of the relatively large decrease in surface moisture content from the relatively large decrease in ocean sea temperature (table 9).

In 54-m wind convergence maps show a sea breeze front for both the NARR (contoured) and uniform (shaded) model runs from 1500 to 1700 UTC (fig. 34). The location of the model sea breeze front is verified by the visible satellite and composite radar (fig. 9a-f). There are minimal differences between the location of the sea breeze front between the NARR and the uniform at 1500 UTC for Long Island Sound (fig. 34). The differences are small because the differences in 2-m temperature are less than 0.25˚C over WLIS and CLIS, which results in small differences in the land-sea temperature gradient. Even when viewing the sea breeze front from vertical cross sections and zoomed in vertical cross sections for WLIS and ELIS, there is very little difference in sea breeze position (fig.34c-f). The wind convergence difference map shows no dipole pattern along the sea breeze front, thus there is very little indication of notable differences in sea breeze front position between the NARR and uniform (fig. 34b).

3.5.5 G1SST Sensitivity Experiment

In the G1SST, the SST has a strong horizontal SST gradient at the mouth of Long Island Sound (fig. 35a). In CLIS, the SST is a warm 23.9˚C. In ELIS, the SST is a cooler 21˚C. The horizontal SST gradient is 2.9˚C between CLIS and ELIS, which exceeds the 0.7˚C NARR SST gradient for the July sea breeze case (fig.35a and fig. 27a). In WLIS, the SST is 21.9˚C, which is 2˚C cooler than CLIS. Therefore, the largest horizontal SST gradient is between CLIS and ELIS

rather than WLIS and CLIS.

In the G1SST, the ocean sea temperature impacts the 2-m temperature through surface heat fluxes (fig. 35). At 1500 UTC, the CLIS is 24.3˚C whereas ELIS is 22.9˚C. ELIS 2-m temperature remains relatively constant over the following 2 hours, while CLIS increases to 25.6˚C by 1700 UTC. Similar to the uniform and NARR simulations, the 2-m temperature increase in CLIS is due to surface heat fluxes which will be further examined. Warm air advection from Long Island and New York City is also a major factor, which is evident by the southwesterly winds in Long Island and New York City. The 10-m wind has a very similar direction and magnitude as the NARR and uniform simulations for the July sea breeze for 1500 UTC through 1700 UTC.

At 1500 UTC, the sensible heat flux in WLIS is -6.1 W m^{-2} in WLIS, -3.1 W m^{-2} in CLIS and -17.6 W m^{-2} in ELIS (fig. 35c). As indicated by the downward sensible heat fluxes in WLIS, CLIS and ELIS, warm air advection has a large impact. Impacts from SST can also be seen in the sensible heat flux. The sensible heat flux is most negative in ELIS because of the very cool 21˚C SST underlying the warm 22.9˚C 2-m temperature. Although the sensible heat flux is still negative in CLIS, the absolute magnitude of the sensible heat flux is relatively small due to the relatively warm 23.9˚C SST underlying an even warmer 24.3˚C 2-m temperature. The latent heat flux at 1500 UTC is 9.1 W m^{-2} in WLIS, 43.0 W m^{-2} in CLIS and -2.8 W m^{-2} in ELIS (fig. 35d). A negative latent heat flux is occurring in ELIS because there is more moisture at the first model level (54-m) than at the surface (table 11).

3.5.6 G1SST versus Uniform

The differences in 2-m temperature between the G1SST and the uniform are shown in figure 36d,h and i. By increasing the SST to 1 km resolution, the 2-m temperature is 0.3˚C, 0.4˚C

and 0.7 ˚C less at 1500 UTC, 1600 UTC and 1700 UTC, respectively, in ELIS. In CLIS, the 2-m temperature is 0.9 ˚C more at 1500 UTC through 1700 UTC. In WLIS, the 2-m temperature is 0.3˚C less at 1500 UTC through 1700 UTC. The 2-m temperature differences in CLIS and ELIS are respectively 0.9˚C and 0.3˚C larger than the differences between the NARR and uniform. The 2-m temperature difference plots remain about the same from 1500 UTC through 1700 UTC. Furthermore, although the differences in 10-m wind speed are overall minor between 1500 UTC and 1700 UTC, the G1SST is 0.4 m s^{-1} slower than the uniform along the sea breeze front at 1500 UTC along eastern coastal CT, which suggests a weaker sea breeze in the G1SST, which is confirmed in the horizontal wind convergence plots (fig. 36e,i,m and fig. 37f)

The sensible heat flux differences between the G1SST and uniform are -1.0 W m^{-2} (-20%) in WLIS, 4.7 W m^{-2} (60%) in CLIS and -9 W m^{-2} (-105%) in ELIS (fig. 36b). The sensible heat flux becomes more negative in ELIS because of the more negative temperature difference between the ocean surface and air aloft in the G1SST from the cooler sea temperature (table 10). The difference is more negative because of the cooler ocean sea temperature in the G1SST in ELIS. The sensible heat flux becomes less negative in CLIS because of the less negative temperature difference between the ocean surface and air aloft in the G1SST (table 10). The difference is less negative because of the warmer ocean sea temperature in the G1SST in CLIS. The latent heat flux differences between the G1SST and the uniform are -2.4 W m^{-2} (21%) in WLIS, 19.4 W m^{-2} (82%) in CLIS and -24.4 W m^{-2} (-113%) in ELIS (fig.36c). The latent heat flux is decreasing in ELIS because of the smaller specific humidity difference between the surface and air aloft from the cooler sea temperature (table 11). The latent heat flux is increasing in CLIS because of the larger specific humidity difference between the surface and air aloft from the warmer sea temperature.

The sea breeze front position differences are very small by increasing the SST resolution to 1 km for the 08 July 2013 sea breeze (fig. 37a,d,f). In WLIS, the G1SST front is 0.25 km less inland than the uniform sea breeze front (fig. 37d). In ELIS, the sea breeze front is 0.5 km less inland than the uniform sea breeze front (fig.37f). The wind convergence difference plots show weak dipole patterns along the CT sea breeze front, (fig.37b), indicating that the G1SST sea breeze has propagated less inland than the uniform sea breeze in WLIS and ELIS. The small differences in sea breeze front position between the G1SST and the uniform are not because of the small sea temperature differences. In fact, the ocean sea temperature differences between the G1SST and uniform for the 08 July 2013 sea breeze (fig. 36a) are comparable to the ocean sea temperature difference for the 21 August 2013 sea breeze (fig. 28a), where the 21 August 2013 sea breeze has sea breeze front position differences beyond a kilometer. A question remains as to why larger (~1-3km) sea breeze front position differences exist in the 21 August 2013 sea breeze than the 08 July 2013 sea breeze (fig. 29 and fig. 37), especially when the sea temperature difference between the G1SST and the uniform for the two sea breeze events are comparable (fig. 28a and fig. 36a). One important distinction between the August sea breeze and the July sea breeze is that the synoptic conditions are stronger for the July sea breeze, as indicated by the persistent westerly and southwesterly winds in the July sea breeze observations (fig. 8g-h and fig. 9g-h) and model results (fig. 23b,e,h and fig. 31b,e,h). Therefore, the differences in sea breeze front location between the SST products may be suppressed by the underlying synoptic conditions that exist during the July sea breeze event.

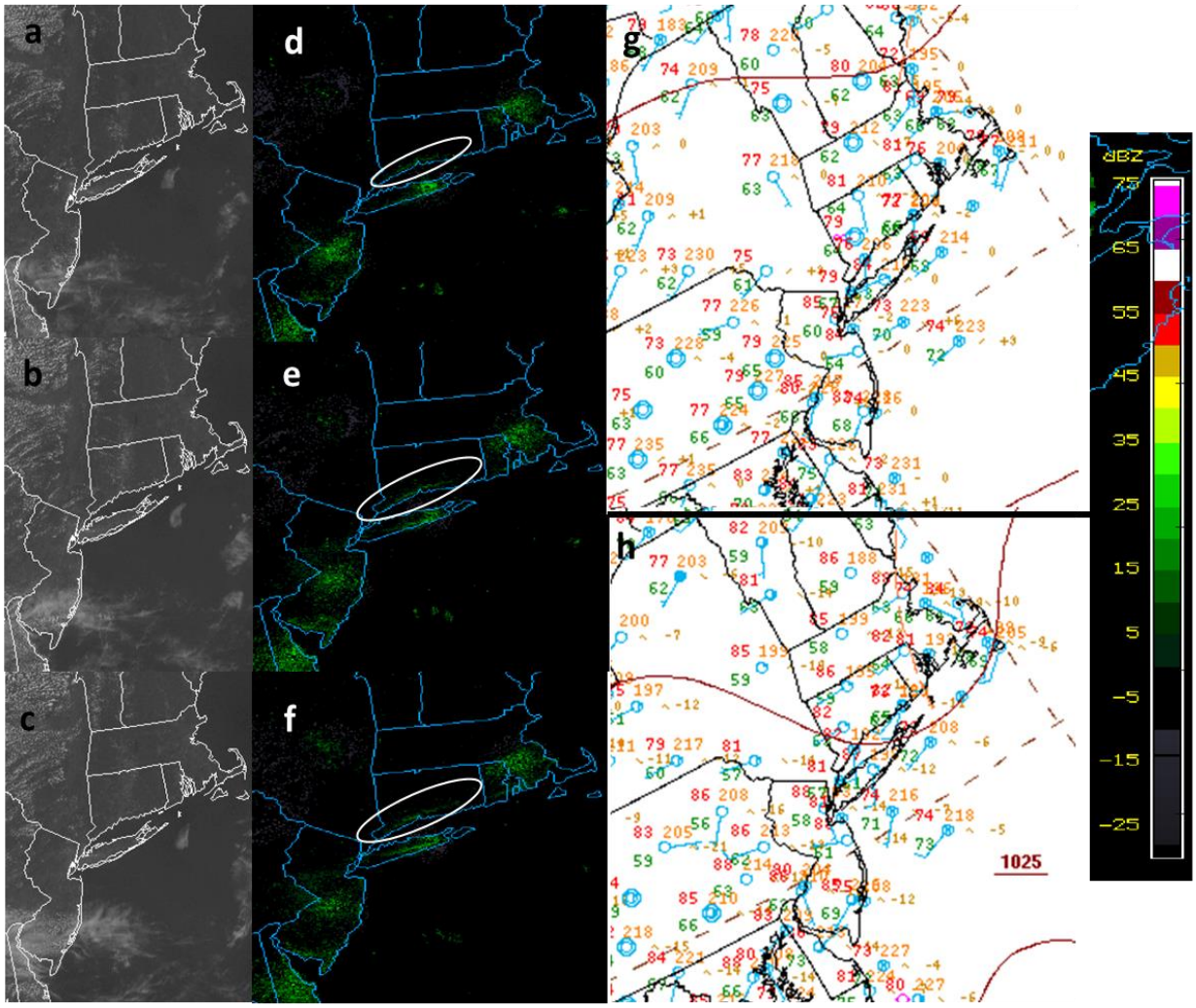

Figure 8. Observation Maps of 21 August 2013: (a-c) Visible Satellite Images: (a) 1545, (b) 1645, (c) 1745; (d-f) Composite Radar Images: (d) 1557, (e) 1657, (f) 1754; (g-h) Surface Analysis Maps: (g) 1500, (h) 1800. The circles in (d-f) identify the Connecticut sea breeze front.

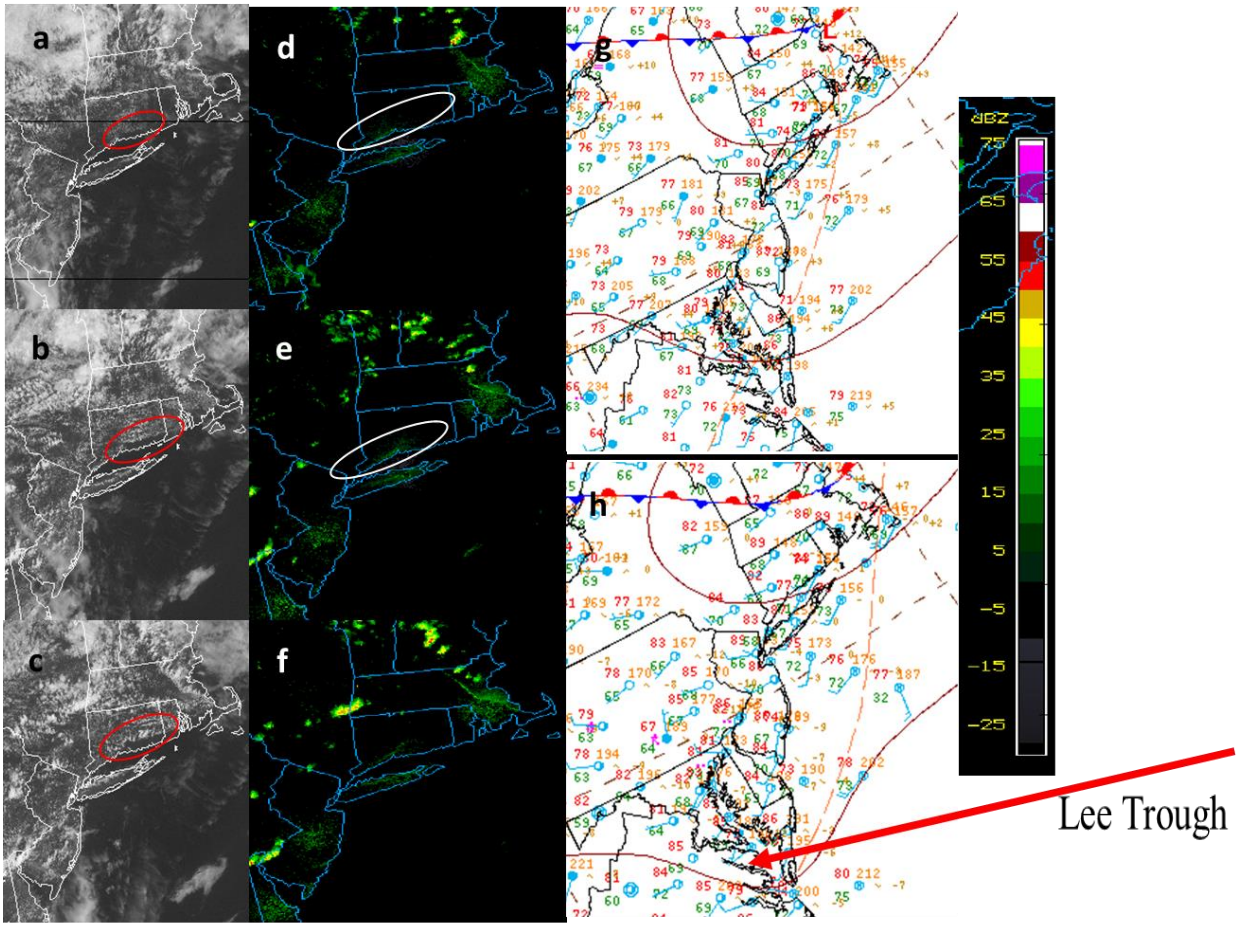

Figure 9. Observation Maps of 08 July 2013: (a-c) Visible Satellite Images: (a) 1545, (b) 1645, (c) 1745; (d-f) Composite Radar Images: (d) 1559, (e) 1659, (f) 1800; (g-h) Surface Analysis Maps: (g) 1500, (h) 1800. The circles in (a-f) identify the sea breeze front. The red arrow points to the lee trough (discussed in text).

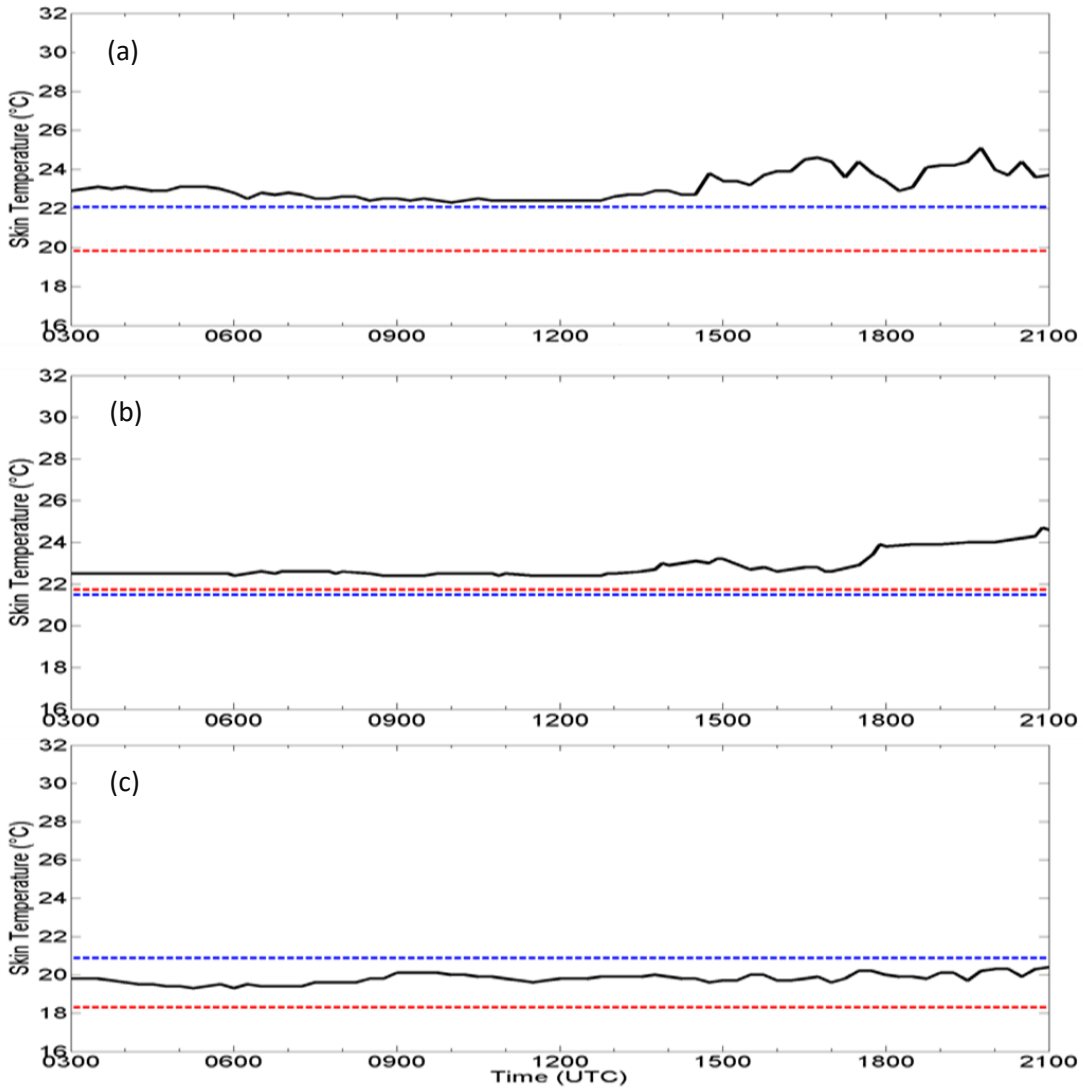

Figure 10. 21 August 2013 Sea Temperature: (a) WLIS, (b) CLIS, (c) ELIS; blue dashed line: *HRCoast_night*; red dashed line: *OrigCoast_night*; black solid line: observations.

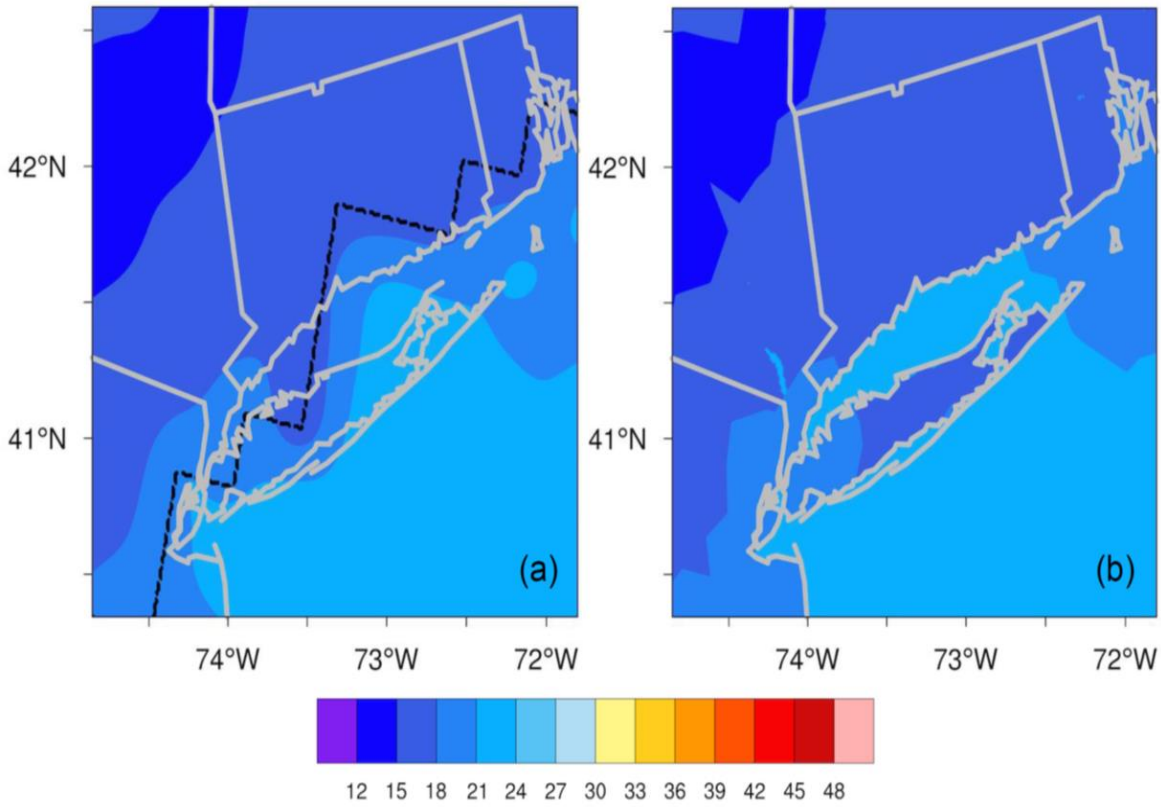

Figure 11. 21 August 2013 0300 UTC Sea Temperature (˚C): (a) *Origcoast_night*, (b) *HRCoast_night*. The dashed line in (a) represents the NARR (32 km) coastline and the grey solid line represents the WRF (1 km) coastline.

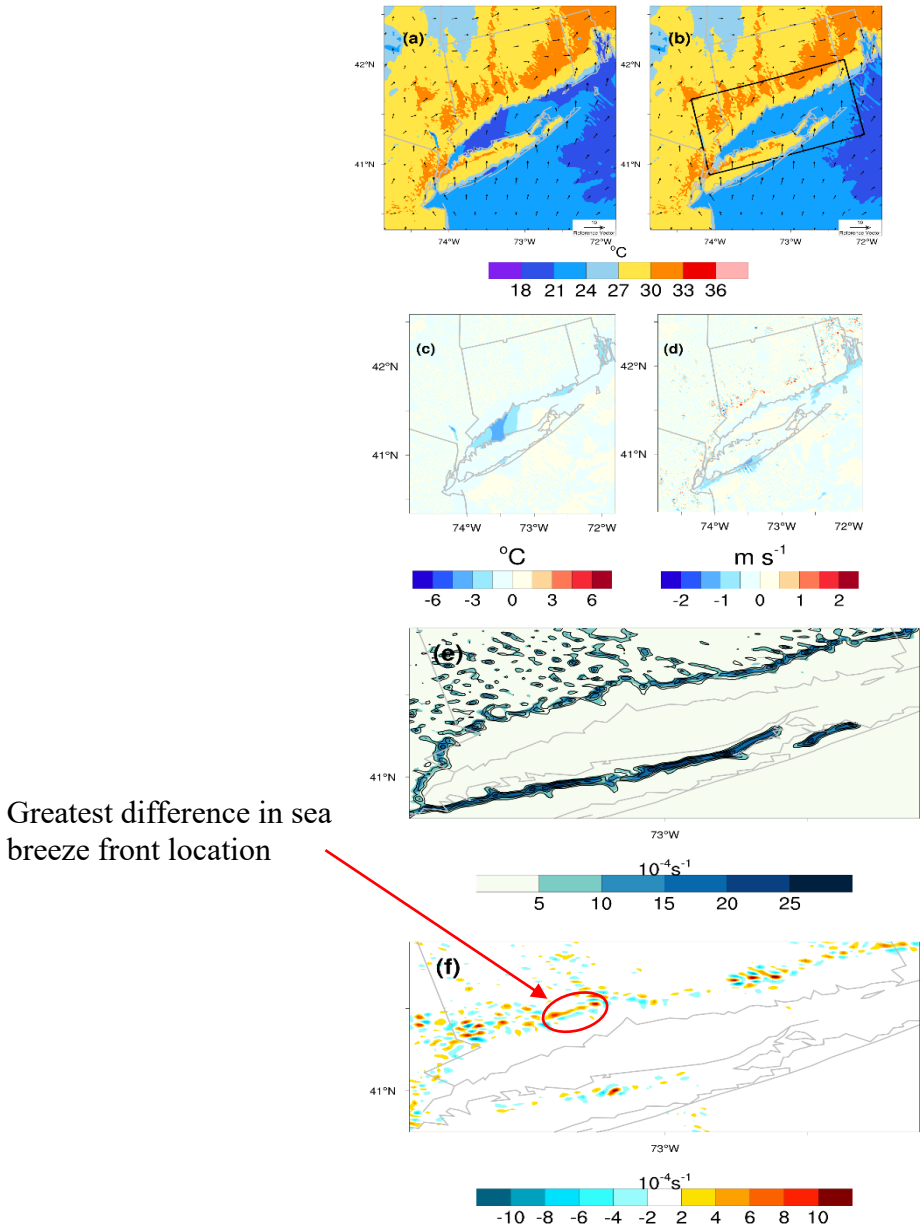

Figure 12. 21 August 2013 1700 UTC. 2-m temperature (˚C) and 10-m wind (m s^{-1}) for (a) *OrigCoast_night* and (b) *HRCoast_night*. (c-d) *Origcoast_night* minus *HRCoast_night*: (c) 2-m temperature difference; (d) 10-m wind speed difference. (e) Origcoast_night (10^{-4} s^{-1}; shaded) and *HRCoast_night* (10^{-4} s^{-1}; contoured) 54-m wind convergence (the intervals are the same for the color shading and contours); (f) *Origcoast_night* minus *HRCoast_night* 54-m wind convergence. The domains of (e) and (f) are denoted by the box in (b).

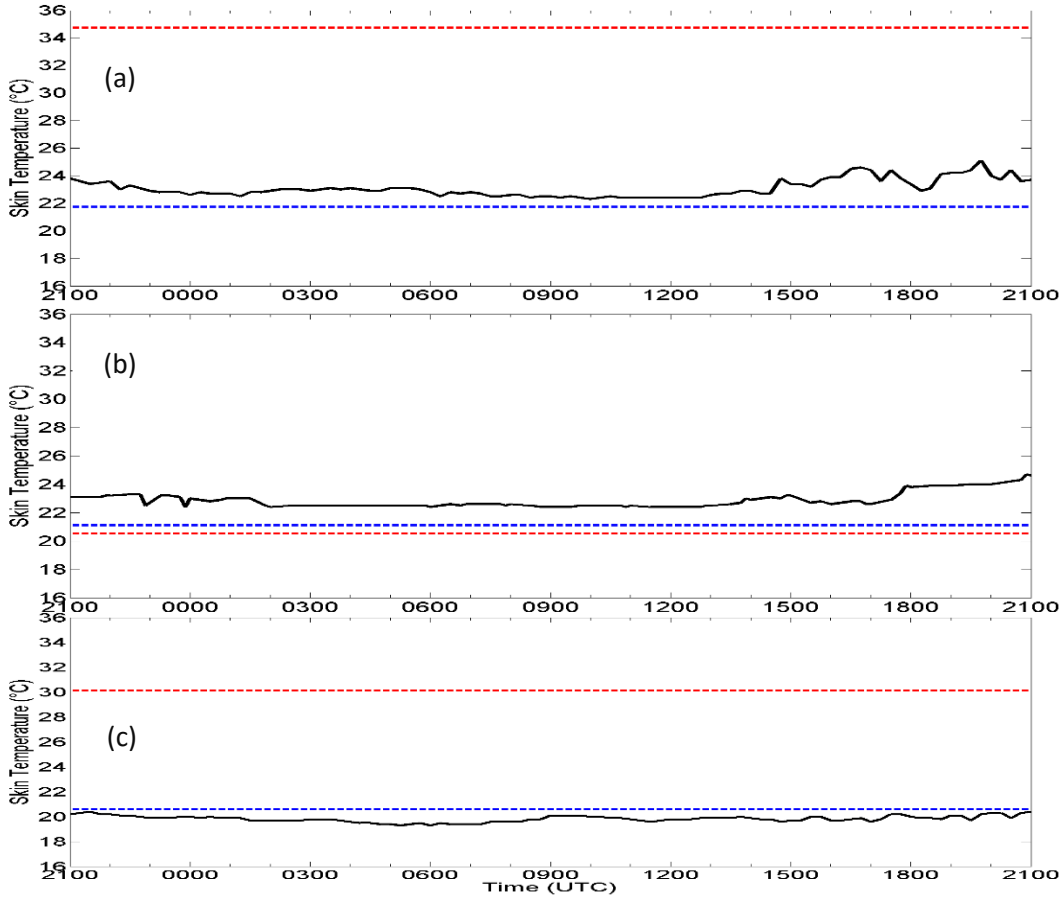

Figure 13. 21 August 2013 Sea Temperature: (a) WLIS, (b) CLIS, (c) ELIS; blue dashed line: *HRCoast_day*; red dashed line: *OrigCoast_day*.

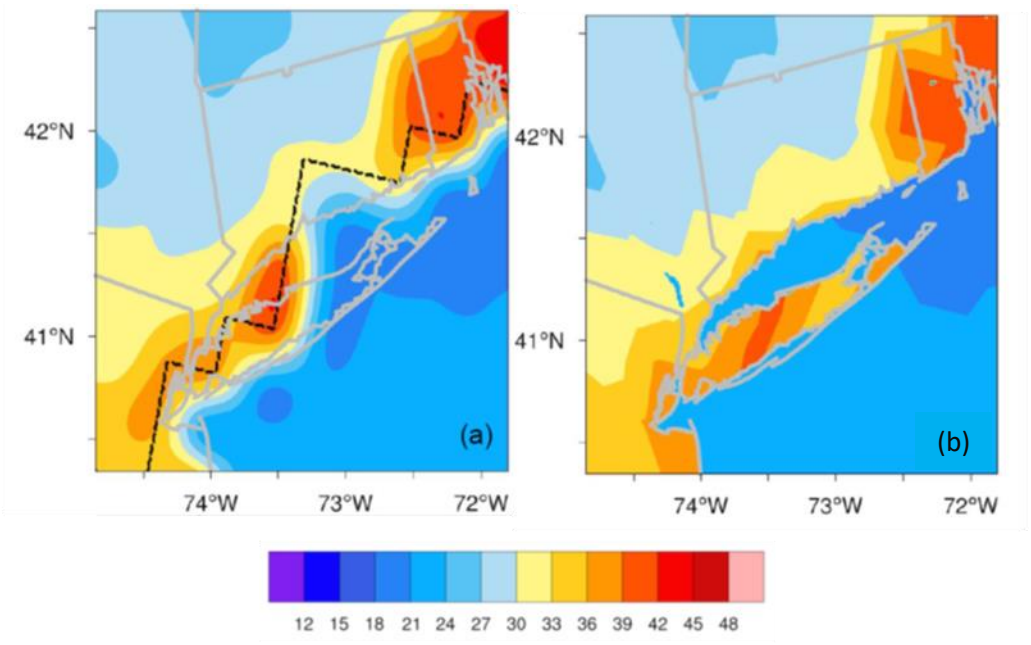

Figure 14. 20 August 2013 2100 UTC Sea Temperature (˚C): (a) *Origcoast_day*, (b) *HRCoast_day*.

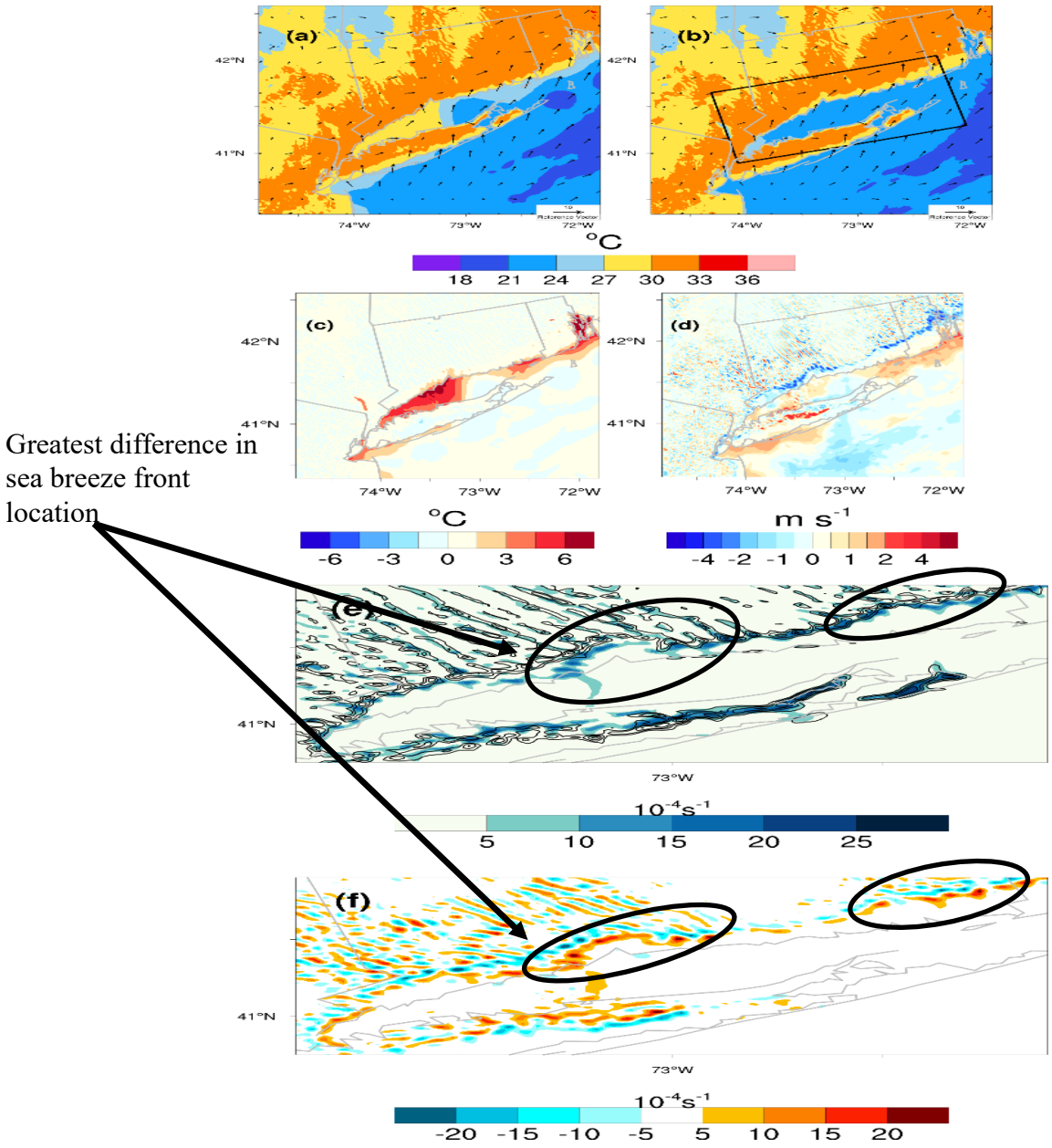

Figure 15. 21 August 2013 1700 UTC. 2-m temperature (˚C) and 10-m wind (m s^{-1}) for (a) *OrigCoast_day* and (b) *HRCoast_day*. (c-d) *Origcoast_day* minus *HRCoast_day*: (c) 2-m temperature difference; (d) 10-m wind speed difference. (e) *Origcoast_day* (10^{-4} s^{-1}; shaded) and *HRCoast_day* (10^{-4} s^{-1}; contoured) 54-m wind convergence (the intervals are the same for the color shading and contours); (f) *Origcoast_day* minus *HRCoast_day* 54-m wind convergence. The domains of (e) and (f) are denoted by the box in (b).

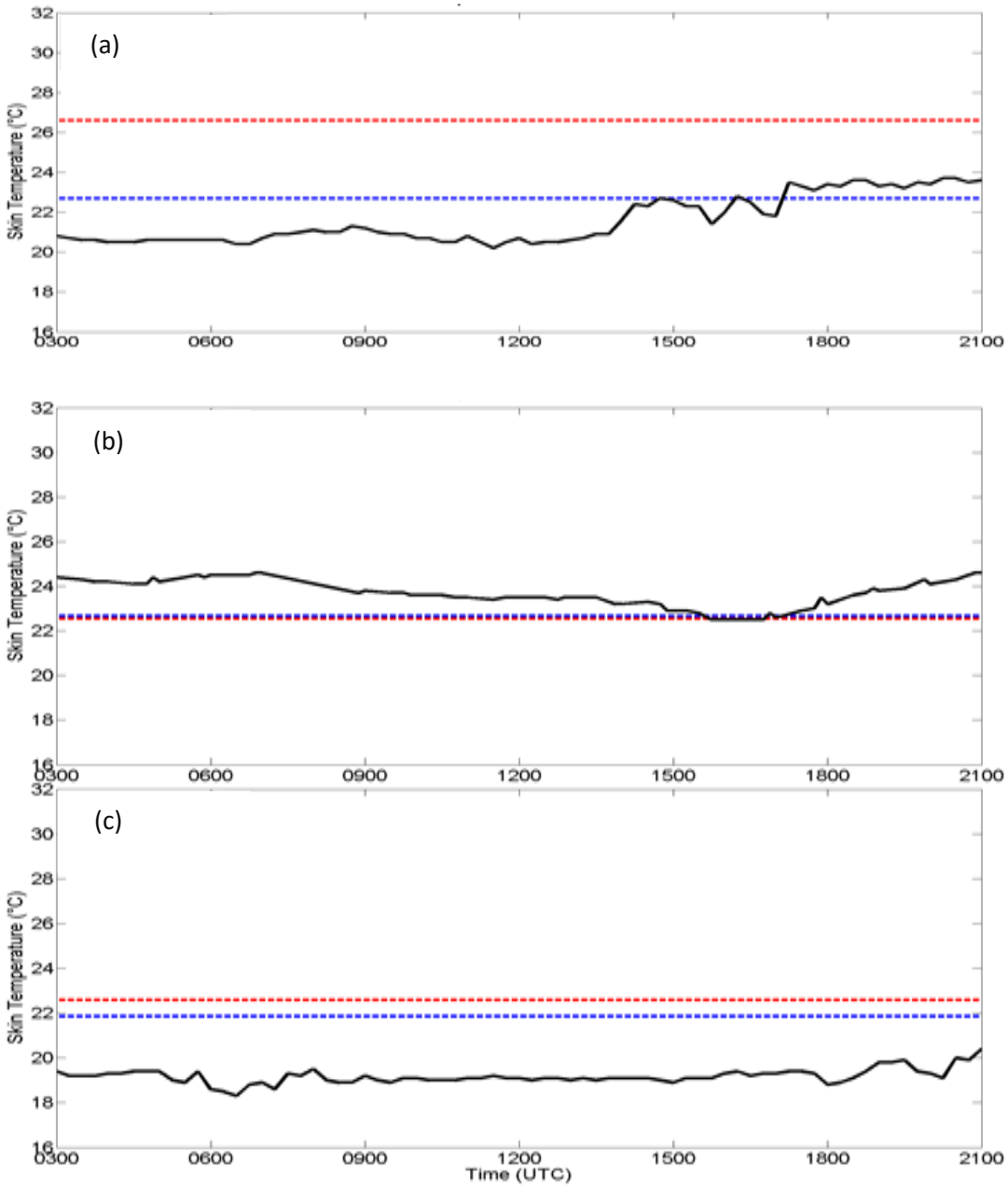

Figure 16. 08 July 2013 Sea Temperature: (a) WLIS, (b) CLIS, (c) ELIS; blue dashed line: *HRCoast_night*; red dashed line: *OrigCoast_night*.

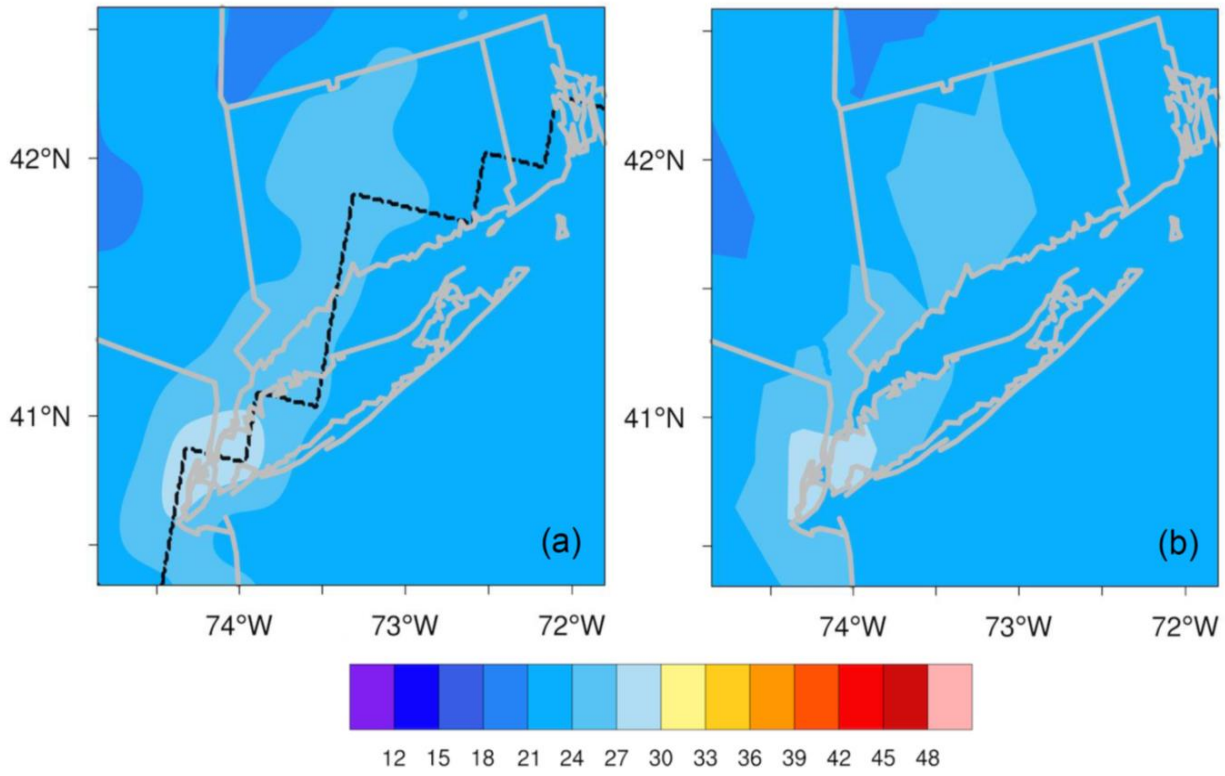

Figure 17. 08 July 2013 0300 UTC Sea Temperature (˚C): (a) *OrigCoast_night*, (b) *HRCoast_night*.

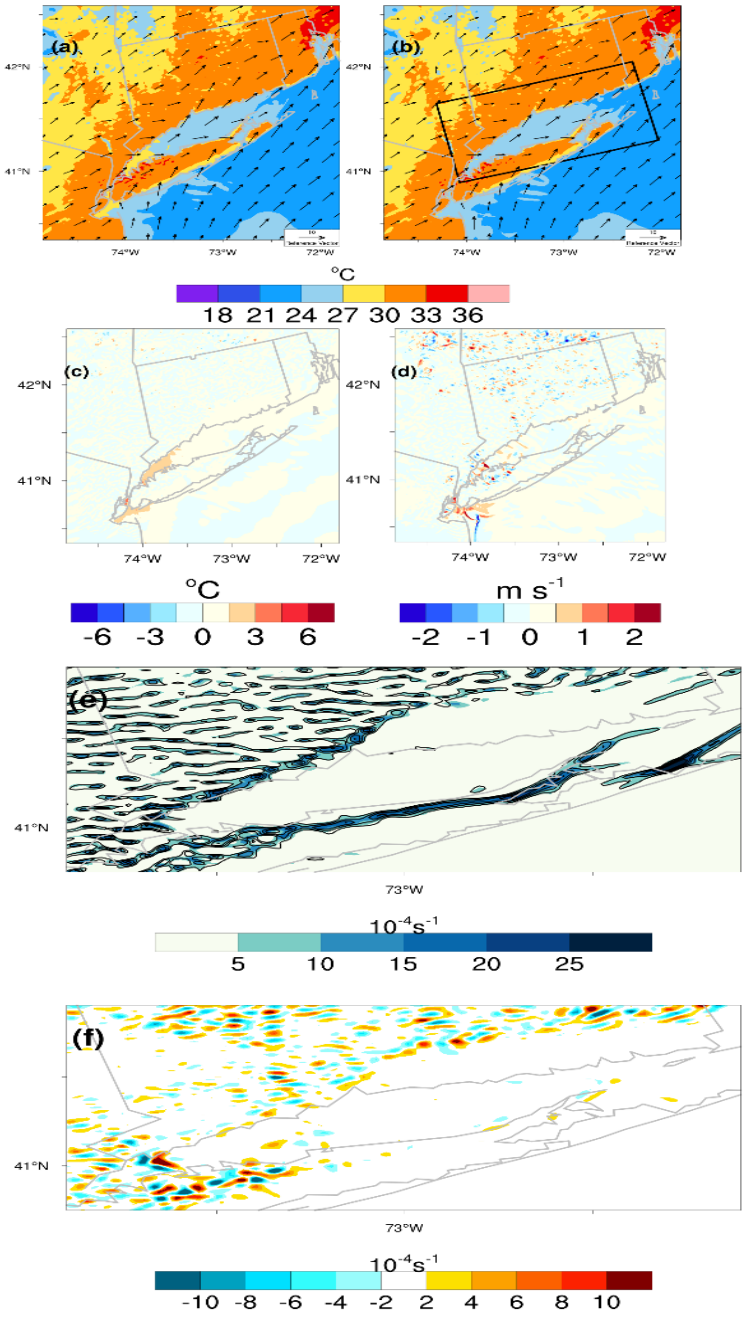

Figure 18. 08 July 2013 1700 UTC. 2-m temperature (˚C) and 10-m wind (m s^{-1}) for (a) *OrigCoast_night* and (b) *HRCoast_night*. (c-d) *Origcoast_night* minus *HRCoast_night*: (c) 2-m temperature difference; (d) 10-m wind speed difference. (e) *Origcoast_night* (10^{-4} s^{-1}; shaded) and *HRCoast_night* (10^{-4} s^{-1}; contoured) 54-m wind convergence (the intervals are the same for the color shading and contours); (f) *Origcoast_night* minus *HRCoast_night* 54-m wind convergence. The domains of (e) and (f) are denoted by the box in (b).

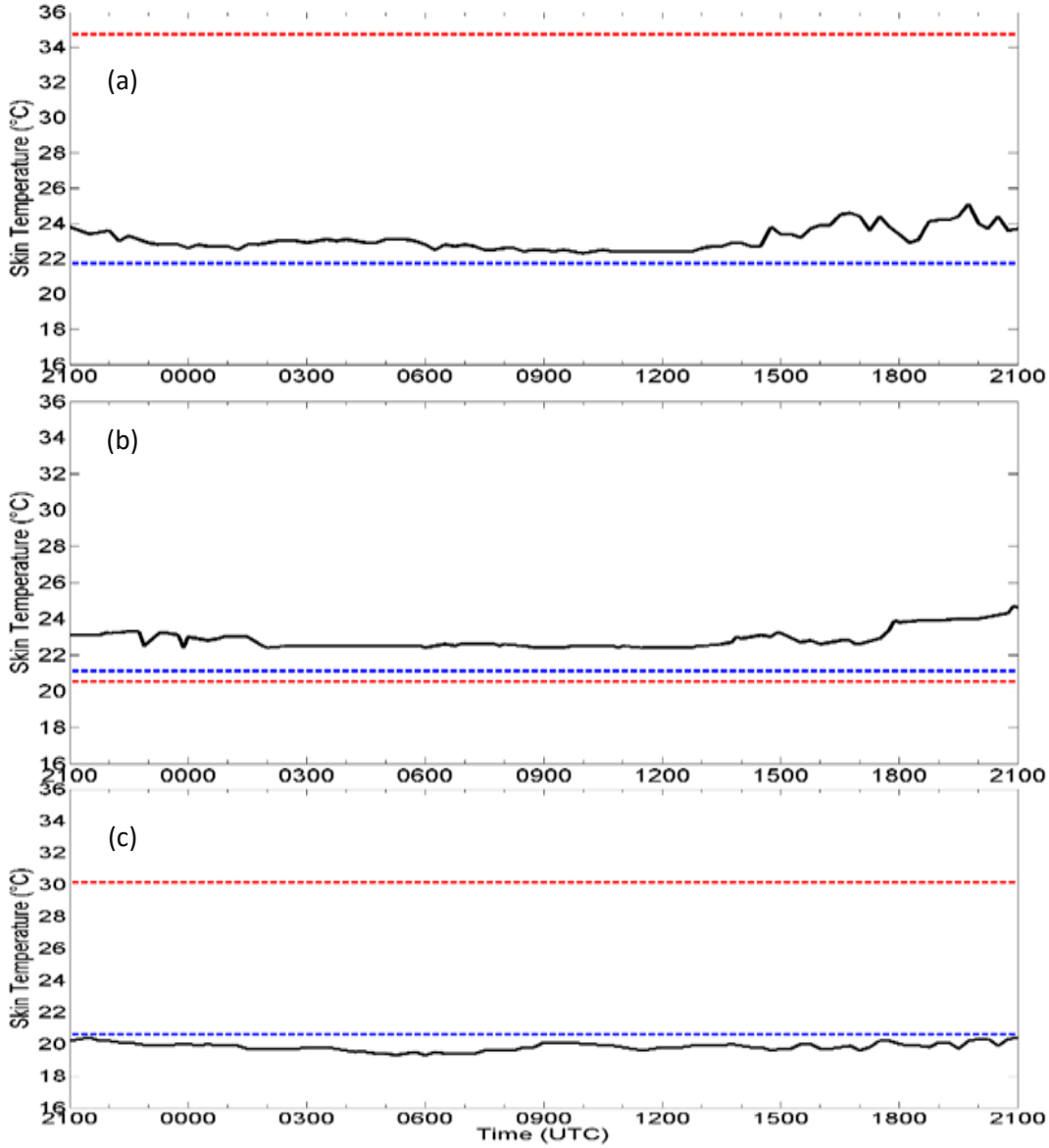

Figure 19. 08 July 2013 Sea Temperature: (a) WLIS, (b) CLIS, (c) ELIS; blue dashed line: *HRCoast_day*; red dashed line: *OrigCoast_day*.

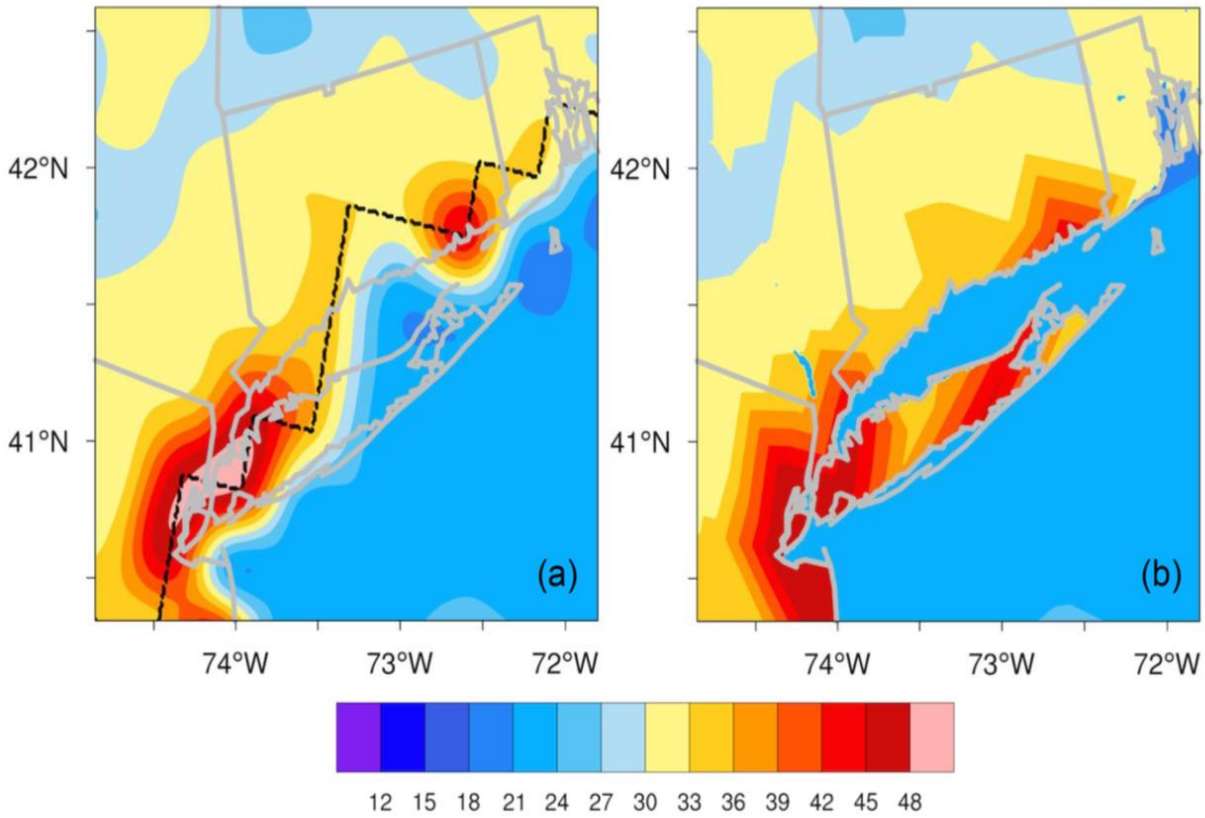

Figure 20. 07 July 2013 2100 UTC Sea Temperature (˚C): (a) *Origcoast_day*, (b) *HRCoast_day*.

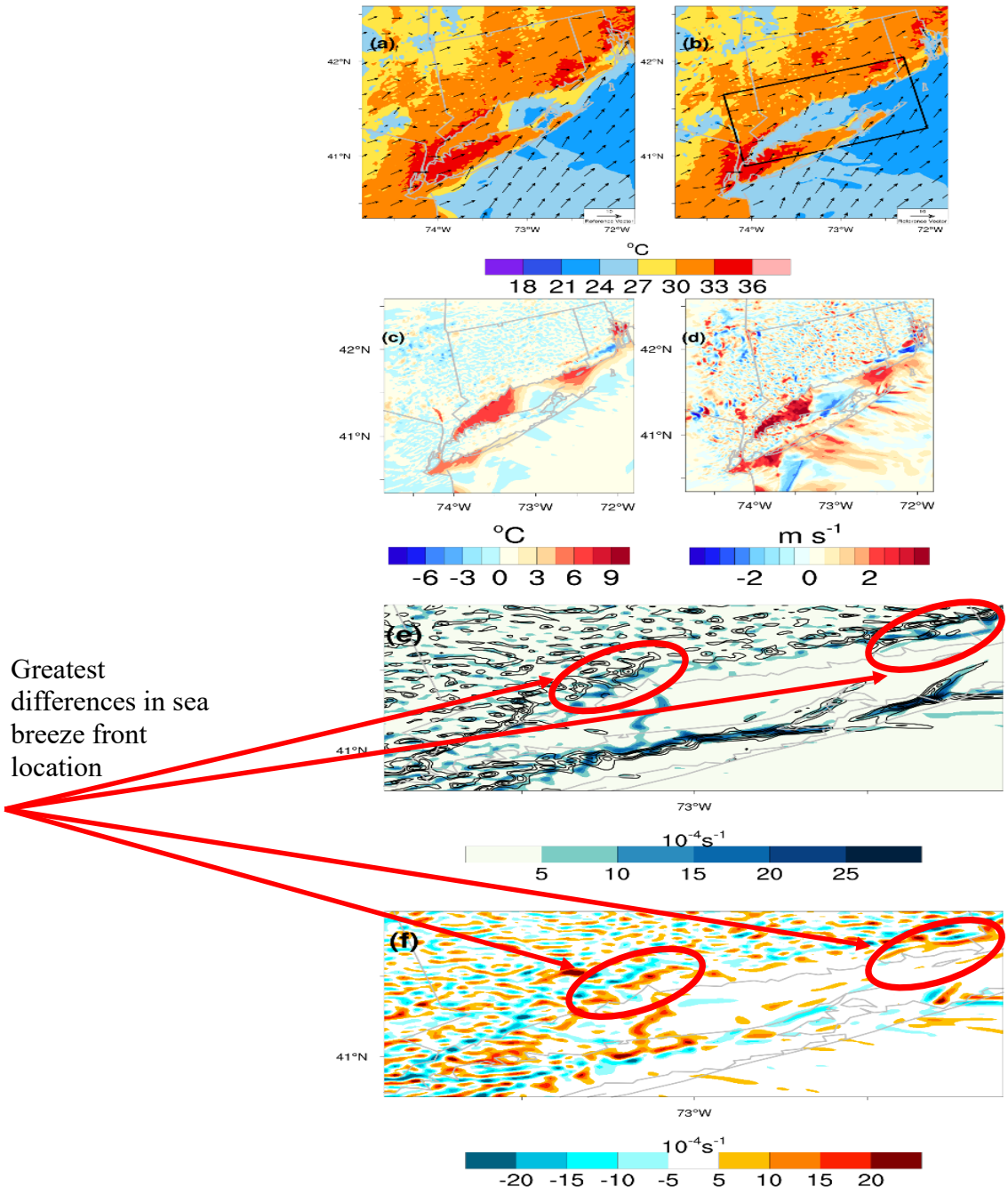

Figure 21. 08 July 2013 1700 UTC. 2-m temperature (˚C) and 10-m wind (m s^{-1}) for (a) *OrigCoast_day* and (b) *HRCoast_day*. (c-d) *Origcoast_day* minus *HRCoast_day*: (c) 2-m temperature difference; (d) 10-m wind speed difference. (e) *Origcoast_day* (10^{-4} s^{-1}; shaded) and *HRCoast_day* (10^{-4} s^{-1}; contoured) 54-m wind convergence (the intervals are the same for the color shading and contours); (f) *Origcoast_day* minus *HRCoast_day* 54-m wind convergence. The domains of (e) and (f) are denoted by the box in (b).

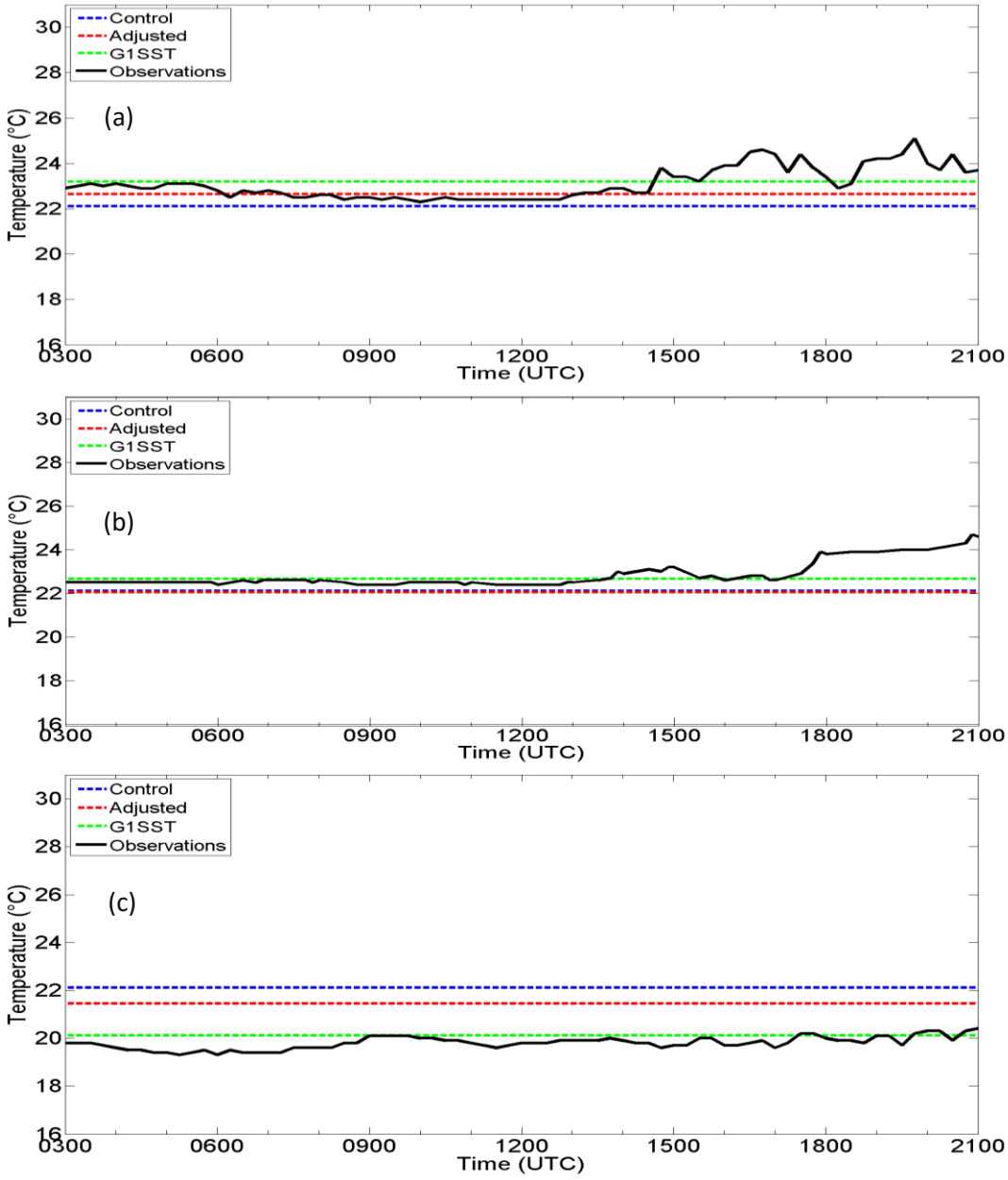

Figure 22. 21 August 2013 Sea Temperature: (a) WLIS, (b) CLIS, (c) ELIS; blue dashed line: Uniform; red dashed line: NARR; green dashed line: G1SST.

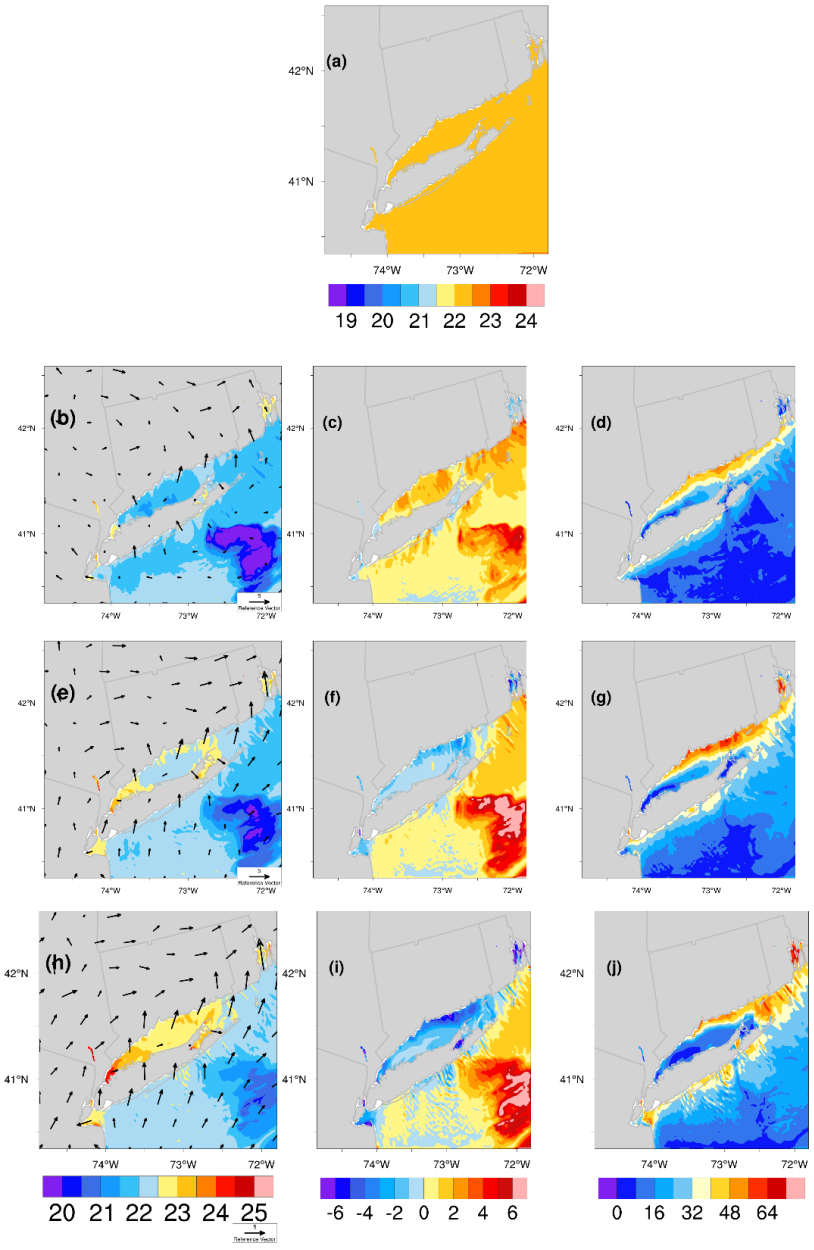

Figure 23. 21 August 2013 Uniform Results. (a) Sea Temperature (˚C); (b,e,h) 2-m temperature (˚C) with 10-m wind (m s^{-1}); (c,f,i) Surface Sensible Heat Flux (W m^{-2}); (d,g,j) Surface Latent Heat Flux (W m^{-2}). (b,c,d) is at 1500 UTC, (e,f,g) is at 1600 UTC, and (h,i,j) is at 1700 UTC. The length of the vector below (h) denotes a 5 m s^{-1} 10-m wind.

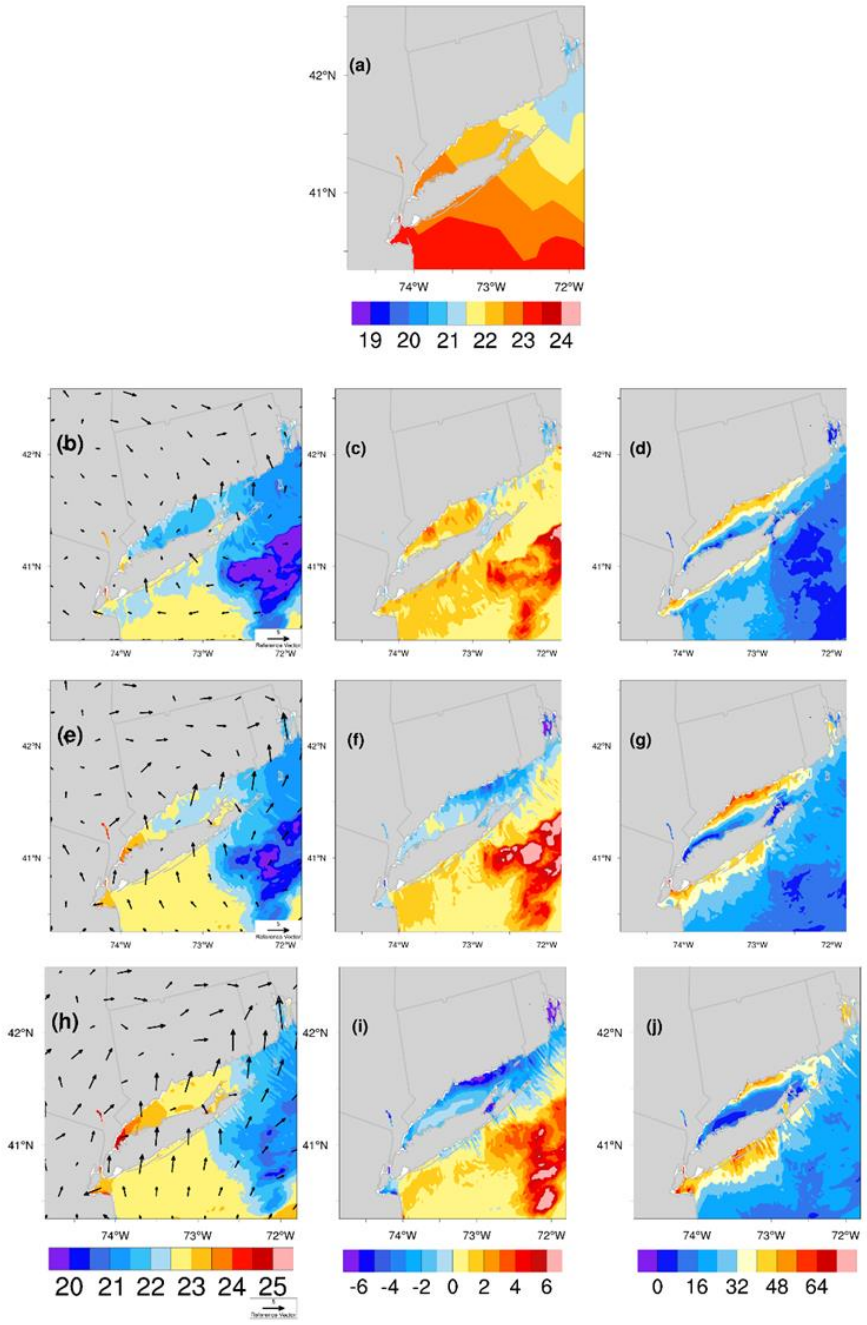

Figure 24. 21 August 2013 NARR Results. (a) Sea Temperature (˚C); (b,e,h) 2-m temperature (˚C) with 10-m wind (m s^{-1}); (c,f,i) Surface Sensible Heat Flux (W m^{-2}); (d,g,j) Surface Latent Heat Flux (W m^{-2}). (b,c,d) is at 1500 UTC, (e,f,g) is at 1600 UTC, and (h,i,j) is at 1700 UTC. The length of the vector below (h) denotes a 5 m s^{-1} 10-m wind.

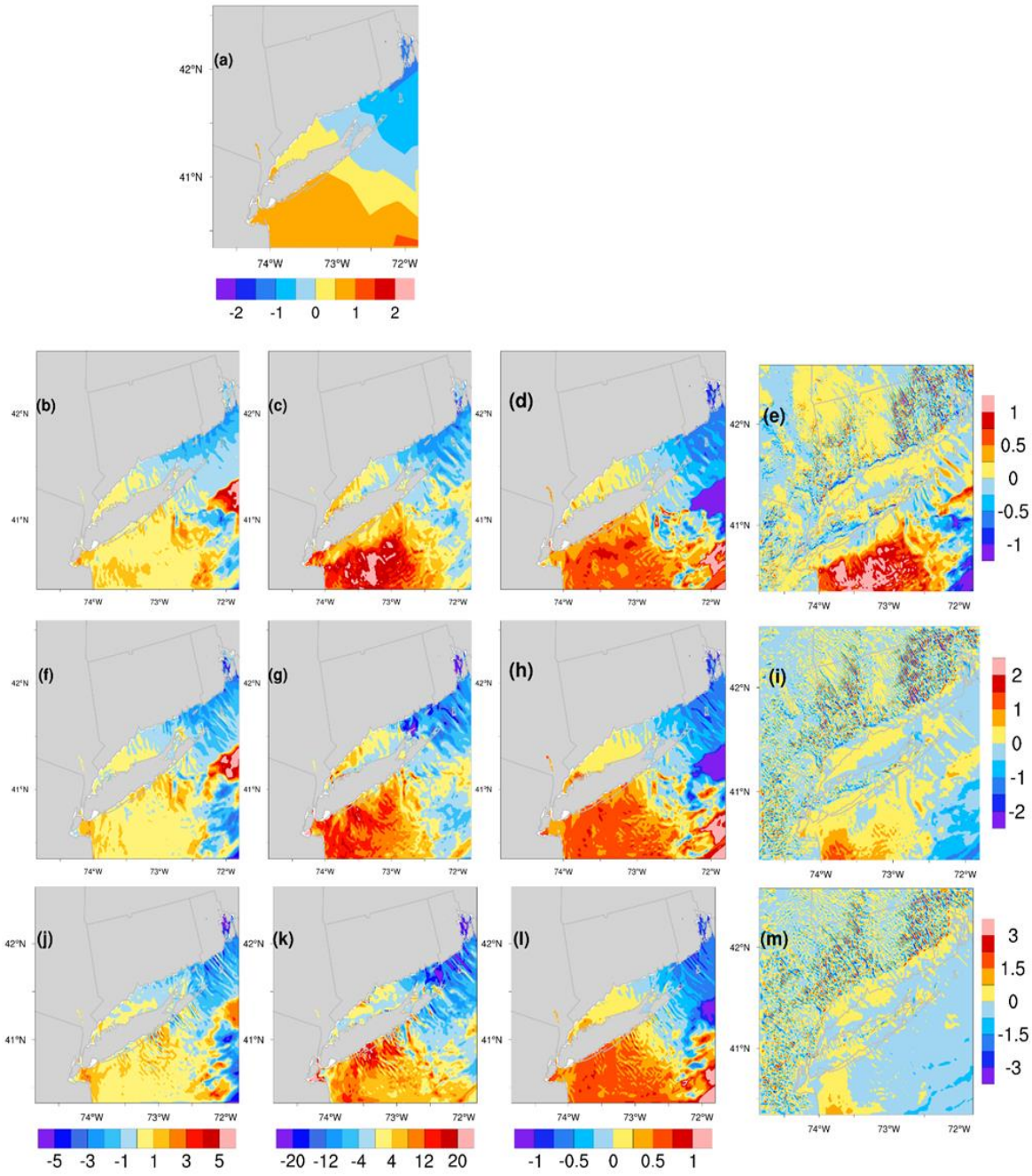

Figure 25. 21 August 2013 NARR minus Uniform plots. (a) Sea Temperature Differences (˚C); (b,f,j) Surface Sensible Heat Flux Differences (W m^{-2}); (c,g,k) Surface Latent Heat Flux Differences (W m^{-2}); (d,h,l) 2-m Temperature Differences (˚C); (e,i,m) 10-m Wind Speed Differences (m s^{-1}). (b,c,d,e) is at 1500 UTC, (f,g,h,i) is at 1600 UTC and (j,k,l,m) is at 1700 UTC.

Table 3. 21 August 2013 sea potential temperature(θ_g), 54-m air potential temperature (θ_a) and their difference (θ_g-θ_a) in Kelvin for 1500 UTC, 1600 UTC and 1700 UTC over WLIS, CLIS and ELIS.

		θ_g	θ_a	θ_g-θ_a
WLIS	1500 UTC	293.5	294.0	-0.5
	1600 UTC	293.5	295.6	-2.1
	1700 UTC	293.5	298.0	-4.5
CLIS	1500 UTC	293.5	292.6	0.9
	1600 UTC	293.5	293.8	-0.3
	1700 UTC	293.5	294.7	-1.2
ELIS	1500 UTC	293.6	293.4	0.2
	1600 UTC	293.6	293.6	0.0
	1700 UTC	293.6	294.0	-0.4

Table 4. 21 August 2013 1500 UTC. NARR and Uniform Sensible Heat Flux (SHF) and the value of the term in eq. 3 that drives the SHF difference. For SHF, the driver term is $(\theta_g-\theta_a)$. Equation 3 is repeated here for convenience with the driver term highlighted in blue: SHF = $\rho c_p C_h U(\theta_g-\theta_a)$.

1500 UTC	**Uniform**	**NARR**	**NARR minus uniform (% change)**
WLIS			
SHF (W m^{-2})	-0.2	0.04	0.24 (120%)
$\theta_g-\theta_a$ (˚C)	-0.462	0.046	0.508 (109%)
CLIS			
SHF (W m^{-2})	2.4	2.3	-0.1 (-4%)
$\theta_g-\theta_a$ (˚C)	0.590	0.535	-0.055 (-9%)
ELIS			
SHF (W m^{-2})	1.2	-0.4	-1.6 (-133%)
$\theta_g-\theta_a$ (˚C)	0.219	-0.043	-0.262 (-120%)

Table 5. 21 August 2013 1500 UTC. NARR and Uniform Latent Heat Flux (LHF) and the value of the term in eq. 4 that drives the LHF difference. For LHF, the driver term is (q_g-q_a). Equation 4 is repeated here for convenience with the driver term highlighted in blue: LHF = $L_e\rho MC_q U(q_g-q_a)$.

1500 UTC	**Uniform**	**NARR**	**NARR minus Uniform (% change)**
WLIS			
LHF (W m^{-2})	9.5	13.1	3.6 (38%)
q_g-q_a (g kg^{-1})	6.07	6.54	0.47 (7%)
CLIS			
LHF (W m^{-2})	36.1	35.4	-0.7 (-2%)
q_g-q_a (g kg^{-1})	3.14	3.00	-0.14 (-4%)
ELIS			
LHF (W m^{-2})	43.3	34.3	-9.0 (21%)
q_g-q_a (g kg^{-1})	2.72	2.21	-0.51 (19%)

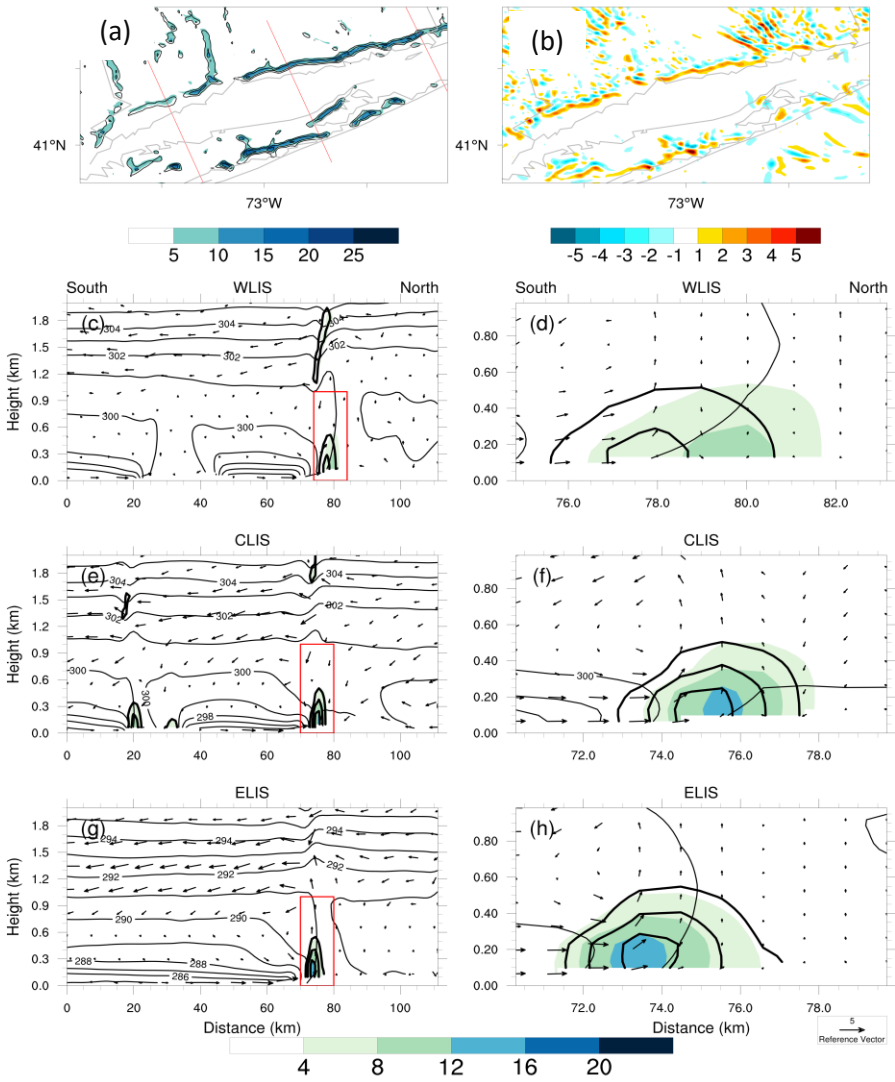

Figure 26. 21 August 2013 1500 UTC Wind Convergence. (a) the uniform wind convergence is color shaded and the NARR wind convergence is contoured (10^{-4} s^{-1}); (b) NARR minus uniform wind convergence plots (10^{-4} s^{-1}); (c-h) Vertical Cross sections of uniform wind convergence (10^{-4} s^{-1}; color shaded), NARR wind convergence (10^{-4} s^{-1}; boldly contoured), virtual potential temperature (K; contoured) and wind parallel to the plane of the cross section (m s^{-1}; vectors). (c) WLIS, (e) CLIS, and (g) ELIS, whose locations are denoted by the red lines in (a). (d) is zoomed into the sea breeze front over WLIS, whose location is denoted by the box in (c); (f) is zoomed into the sea breeze front over CLIS, whose location is denoted by the red box in (e), and (h) is zoomed into the sea breeze front over ELIS whose location is denoted by the box in (g). The uniform wind convergence (color shaded) and the NARR wind convergence (contoured) in (a), (c-h) are plotted at the same interval. The length of the vector below (h) denotes a 5 m s^{-1} 10-m wind.

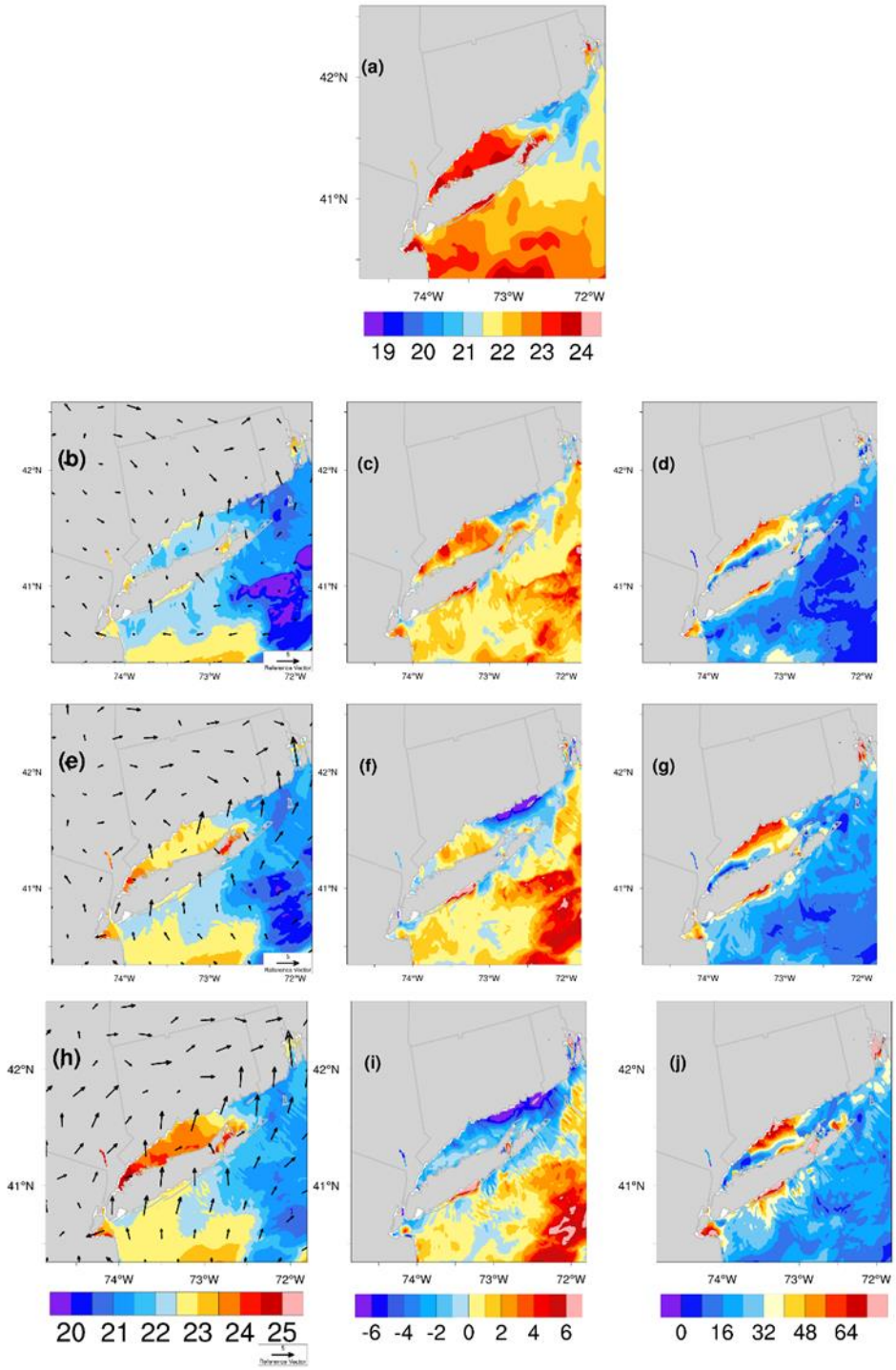

Figure 27. 21 August 2013 G1SST Results. (a) Sea Temperature (˚C); (b,e,h) 2-m temperature (˚C) with 10-m wind (m s^{-1}); (c,f,i) Surface Sensible Heat Flux (W m^{-2}); (d,g,j) Surface Latent Heat Flux (W m^{-2}). (b,c,d) is at 1500 UTC, (e,f,g) is at 1600 UTC, and (h,I,j) is at 1700 UTC. The length of the vector below (h) denotes a 5 m s^{-1} 10-m wind.

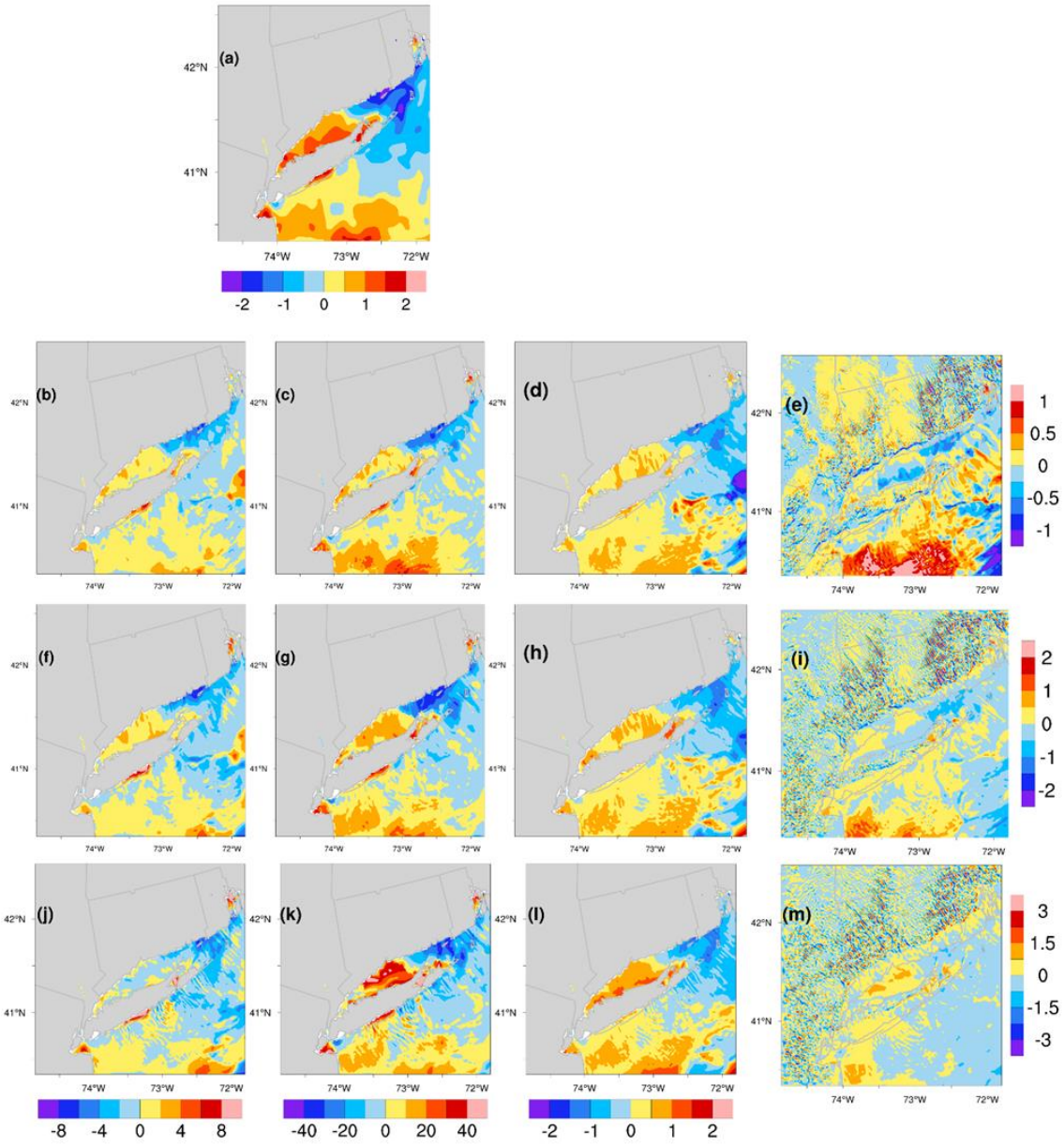

Figure 28. 21 August 2013 G1SST minus Uniform plots. (a) Sea Temperature Differences (˚C); (b,f,j) Surface Sensible Heat Flux Differences (W m^{-2}); (c,g,k) Surface Latent Heat Flux Differences (W m^{-2}); (d,h,l) 2-m Temperature Differences (˚C); (e,i,m) 10-m Wind Speed Differences (m s^{-1}). (b,c,d,e) is at 1500 UTC, (f,g,h,i) is at 1600 UTC and (j,k,l,m) is at 1700 UTC.

Table 6. 21 August 2013 1500 UTC. G1SST and Uniform Sensible Heat Flux (SHF) and the value of the term in eq. 3 that drives the SHF difference. For SHF, the driver term is $(\theta_g - \theta_a)$. Equation 3 is repeated here for convenience with the driver term highlighted in blue: $SHF = \rho c_p C_h U(\theta_g - \theta_a)$.

1500 UTC	**Uniform**	**G1SST**	**G1SST minus uniform (% change)**
WLIS			
SHF (W m^{-2})	-0.2	0.6	0.8 (400%)
$\theta_g - \theta_a$ (˚C)	-0.462	0.360	0.822 (178%)
CLIS			
SHF (W m^{-2})	2.4	2.9	0.5 (21%)
$\theta_g - \theta_a$ (˚C)	0.590	0.711	0.121 (21%)
ELIS			
SHF (W m^{-2})	1.2	-3.6	-4.8 (-400%)
$\theta_g - \theta_a$ (˚C)	0.219	-0.978	-1.197 (547%)

Table 7. 21 August 2013 1500 UTC. G1SST and Uniform Latent Heat Flux (LHF) and the value of the term in eq. 4 that drives the LHF difference. For LHF, the driver term is $(q_g - q_a)$. Equation 4 is repeated here for convenience with the driver term highlighted in blue: $LHF = L_e \rho M C_q U(q_g - q_a)$.

1500 UTC	**Uniform**	**G1SST**	**G1SST minus Uniform (% change)**
WLIS			
LHF (W m^{-2})	9.5	21.8	12.3 (129%)
$q_g - q_a$ (g kg^{-1})	6.07	7.12	1.05 (17%)
CLIS			
LHF (W m^{-2})	36.1	39.9	3.8 (11%)
$q_g - q_a$ (g kg^{-1})	3.14	3.45	3.14 (10%)
ELIS			
LHF (W m^{-2})	43.3	14.2	-29.1 (-67%)
$q_g - q_a$ (g kg^{-1})	2.72	1.40	-1.32 (-49%)

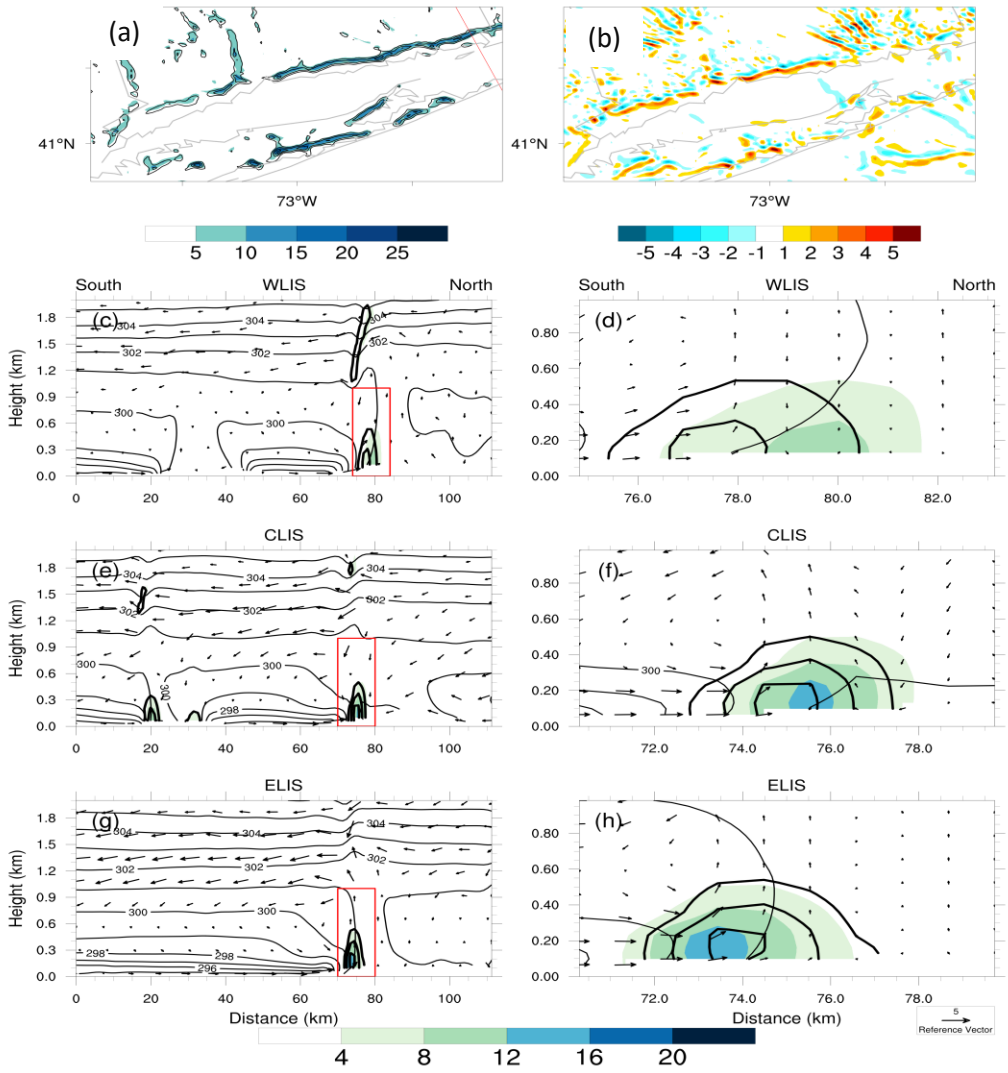

Figure 29. 21 August 2013 1500 UTC Wind Convergence. (a) the uniform wind convergence is color shaded and the G1SST wind convergence is contoured (10^{-4} s^{-1}); (b) G1SST minus uniform wind convergence plots (10^{-4} s^{-1}); (c-h) Vertical Cross sections of uniform wind convergence (10^{-4} s^{-1}; color shaded), G1SST wind convergence (10^{-4} s^{-1}; boldly contoured), virtual potential temperature (K; contoured) and wind parallel to the plane of the cross section (m s^{-1}; vectors). (c) WLIS, (e) CLIS, and (g) ELIS, whose locations are denoted by the red lines in (a). (d) is zoomed into the sea breeze front over WLIS, whose location is denoted by the box in (c); (f) is zoomed into the sea breeze front over CLIS, whose location is denoted by the box in (e), and (h) is zoomed into the sea breeze front over ELIS whose location is denoted by the red box in (g). The uniform wind convergence (color shaded) and the G1SST wind convergence (contoured) in (a), (c-h) are plotted at the same interval. The length of the vector below (h) denotes a 5 m s^{-1} 10-m wind.

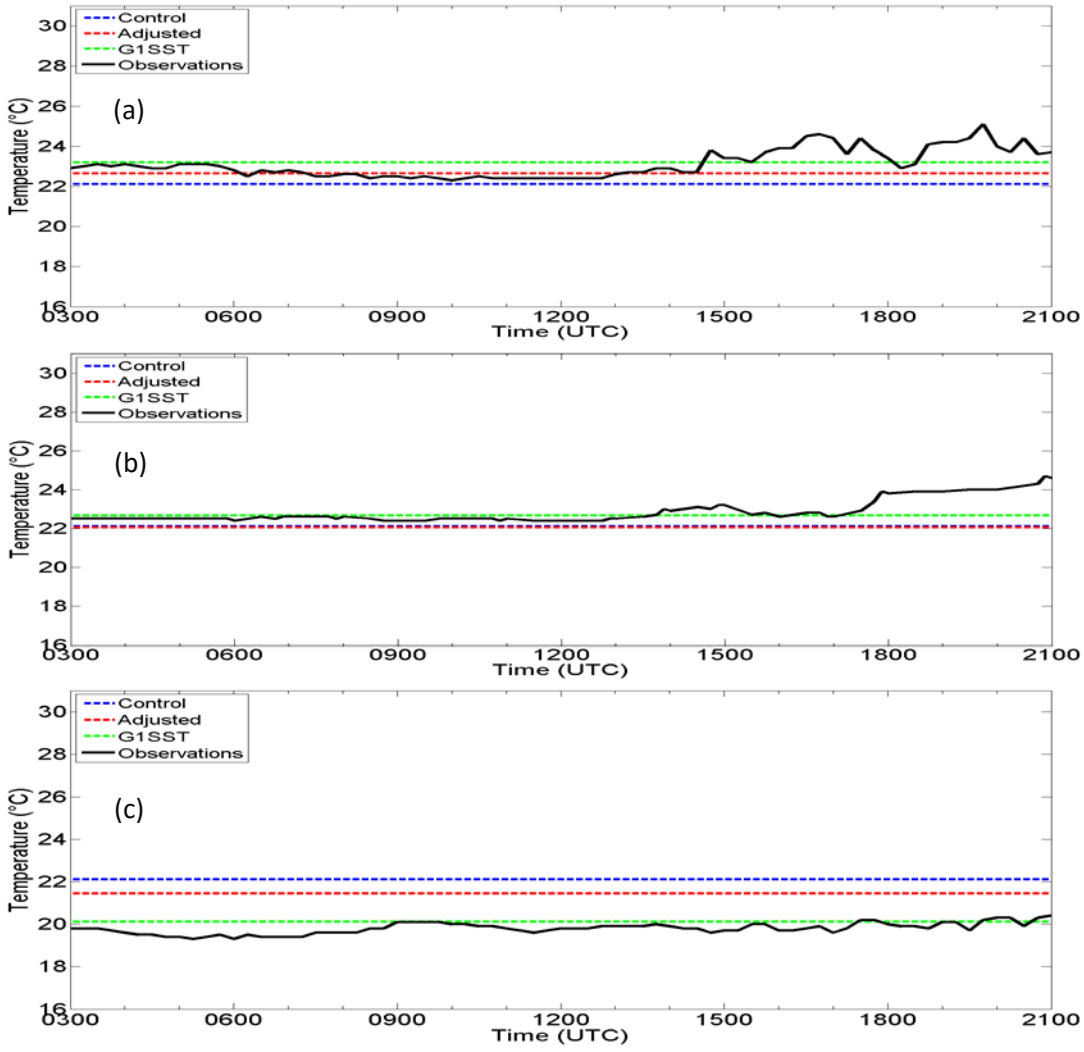

Figure 30. 08 July 2013 Sea Temperature: (a) WLIS, (b) CLIS, (c) ELIS; blue dashed line: Control; red dashed line: Adjusted; green dashed line: G1SST.

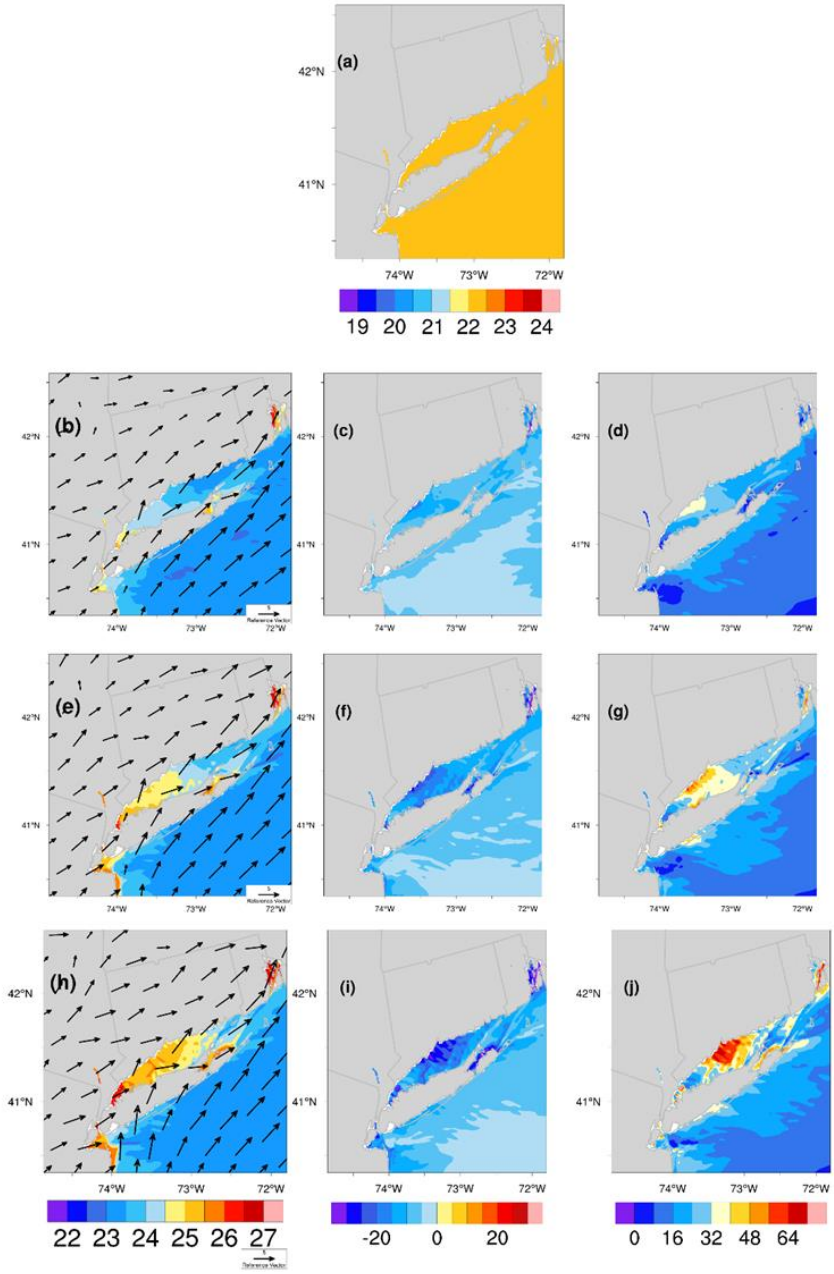

Figure 31. 08 July 2013 Uniform Results. (a) Sea Temperature (˚C); (b,e,h) 2-m temperature (˚C) with 10-m wind (m s^{-1}); (c,f,i) Surface Sensible Heat Flux (W m^{-2}); (d,g,j) Surface Latent Heat Flux (W m^{-2}). (b,c,d) is at 1500 UTC, (e,f,g) is at 1600 UTC, and (h,i,j) is at 1700 UTC. The length of the vector below (h) denotes a 5 m s^{-1} 10-m wind.

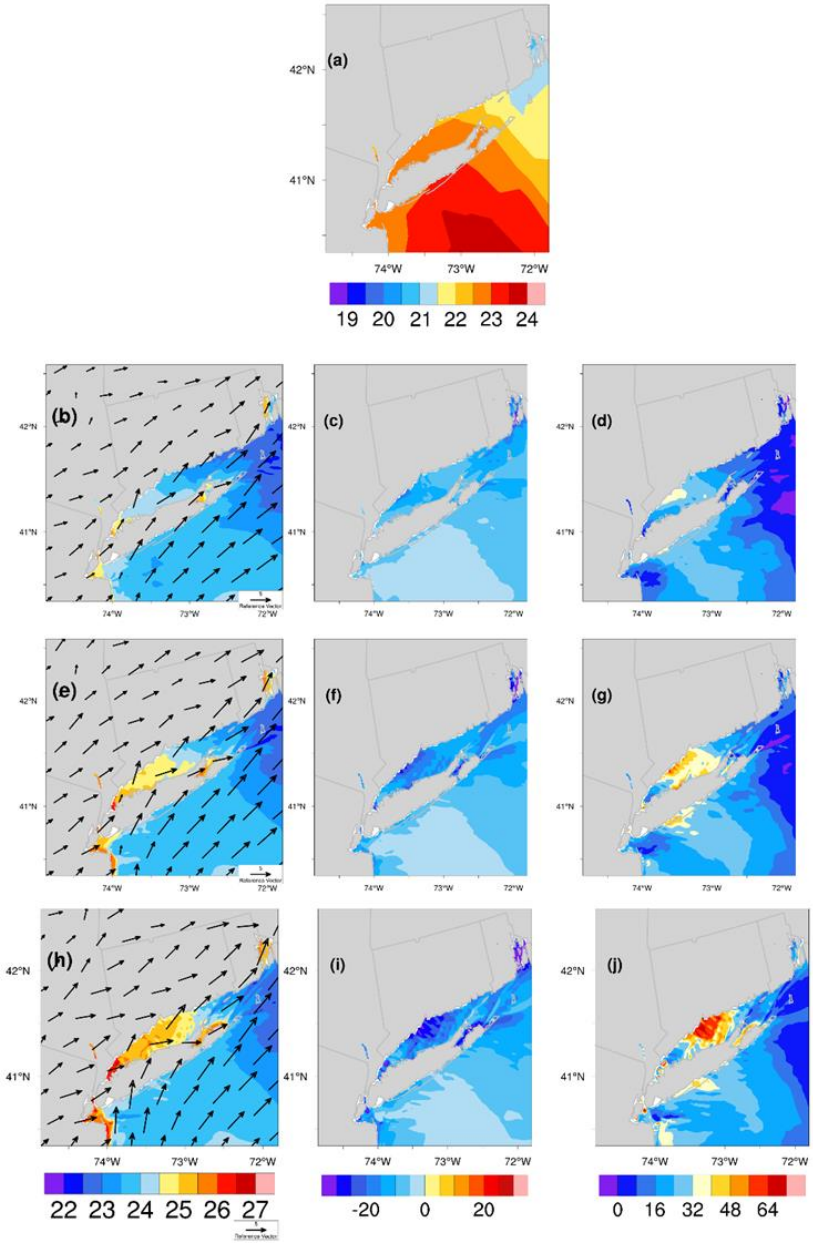

Figure 32. 08 July 2013 NARR Results. (a) Sea Temperature (˚C); (b,e,h) 2-m temperature (˚C) with 10-m wind (m s^{-1}); (c,f,i) Surface Sensible Heat Flux (W m^{-2}); (d,g,j) Surface Latent Heat Flux (W m^{-2}). (b,c,d) is at 1500 UTC, (e,f,g) is at 1600 UTC, and (h,i,j) is at 1700 UTC. The length of the vector below (h) denotes a 5 m s^{-1} 10-m wind.

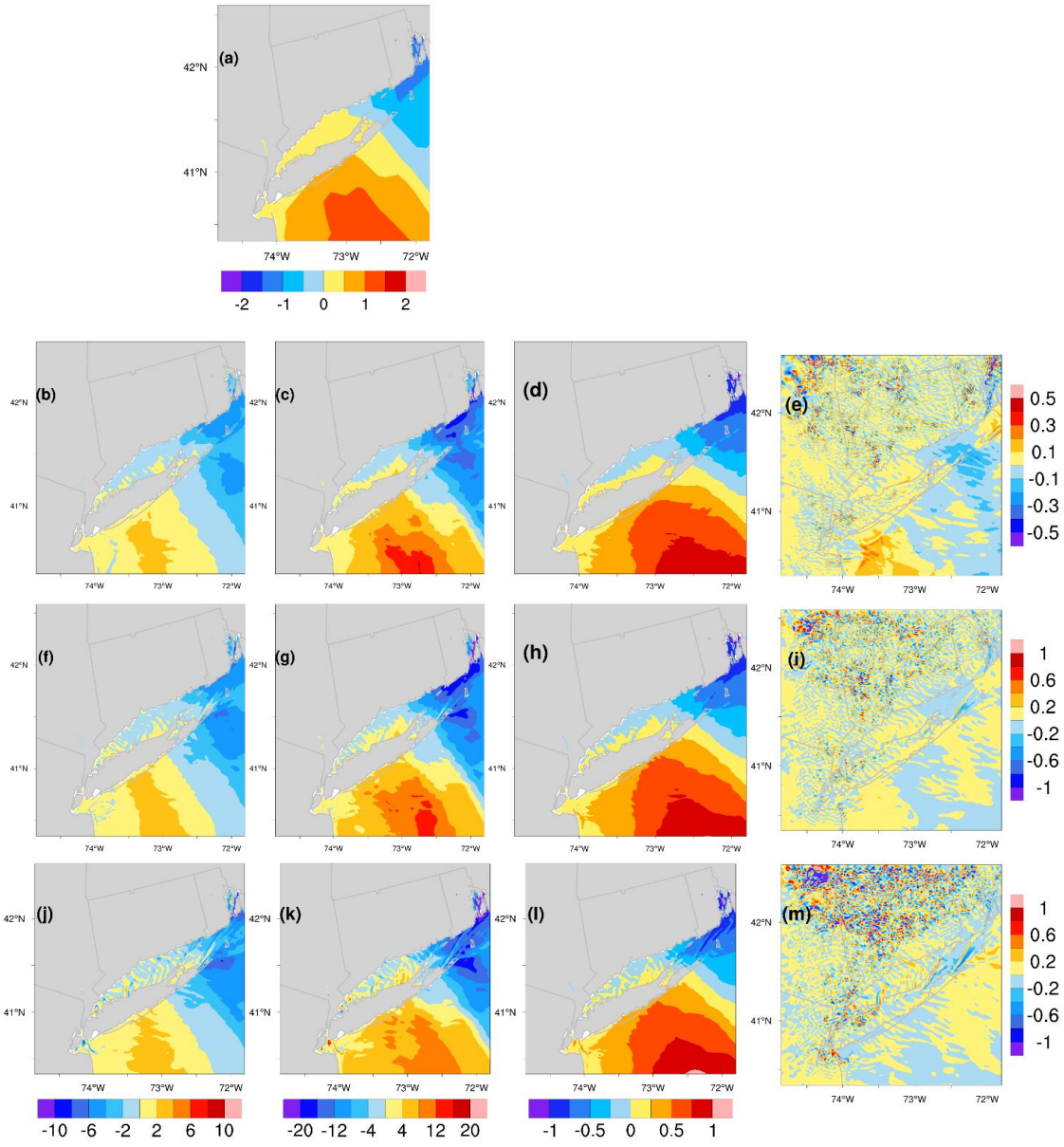

Figure 33. 08 July 2013 NARR minus Uniform plots. (a) Sea Temperature Differences (˚C); (b,f,j) Surface Sensible Heat Flux Differences (W m^{-2}); (c,g,k) Surface Latent Heat Flux Differences (W m^{-2}); (d,h,l) 2-m Temperature Differences (˚C); (e,i,m) 10-m Wind Speed Differences (m s^{-1}). (b,c,d,e) is at 1500 UTC, (f,g,h,i) is at 1600 UTC and (j,k,l,m) is at 1700 UTC.

Table 8. 08 July 2013 1500 UTC. NARR and Uniform Sensible Heat Flux (SHF) and the value of the term in eq. 3 that drives the SHF difference. For SHF, the driver term is $(\theta_g-\theta_a)$. Equation 3 is repeated here for convenience with the driver term highlighted in blue: SHF = $\rho c_p C_h U(\theta_g-\theta_a)$.

1500 UTC	**Uniform**	**NARR**	**NARR minus uniform (% change)**
WLIS			
SHF (W m^{-2})	-5.1	-5.4	-0.3 (-6%)
$\theta_g-\theta_a$ (˚C)	-4.68	-4.65	0.03 (1%)
CLIS			
SHF (W m^{-2})	-7.8	-7.8	0 (0%)
$\theta_g-\theta_a$ (˚C)	-1.40	-1.34	0.06 (4%)
ELIS			
SHF (W m^{-2})	-8.6	-12.3	-3.7 (-43%)
$\theta_g-\theta_a$ (˚C)	-1.12	-1.74	-0.62 (-55%)

Table 9. 08 July 2013 1500 UTC. NARR and Uniform Latent Heat Flux (LHF) and the value of the term in eq. 4 that drives the LHF difference. For LHF, the driver term is (q_g-q_a). Equation 4 is repeated here for convenience with the driver term highlighted in blue: LHF = $L_e\rho MC_q U(q_g-q_a)$.

1500 UTC	**Uniform**	**NARR**	**NARR minus Uniform (% change)**
WLIS			
LHF (W m^{-2})	11.5	10.9	-0.6 (-5%)
q_g-q_a (g kg^{-1})	3.53	3.56	0.03 (1%)
CLIS			
LHF (W m^{-2})	23.6	23.8	0.2 (1%)
q_g-q_a (g kg^{-1})	1.50	1.46	-0.04 (-3%)
ELIS			
LHF (W m^{-2})	21.6	9.2	-12.4 (-57%)
q_g-q_a (g kg^{-1})	0.93	0.36	-0.57 (-61%)

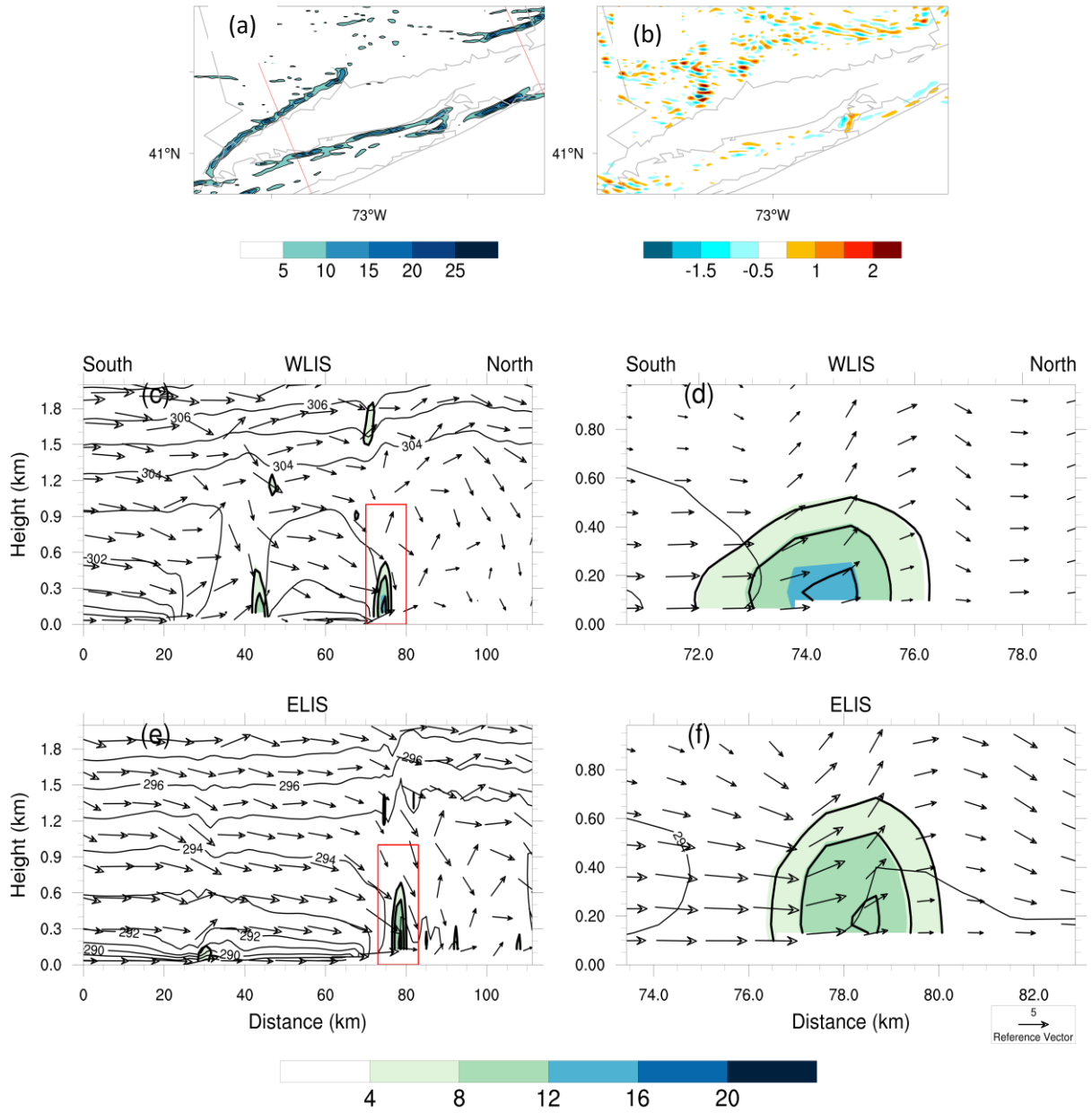

Figure 34. 08 July 2013 1500 UTC Wind Convergence. (a) the uniform wind convergence is color shaded and the NARR wind convergence is contoured (10^{-4} s^{-1}); (b) NARR minus uniform wind convergence plots (10^{-4} s^{-1}); (c-f) Vertical Cross sections of uniform wind convergence (10^{-4} s^{-1}; color shaded), NARR wind convergence (10^{-4} s^{-1}; boldly contoured), virtual potential temperature (K; contoured) and wind parallel to the plane of the cross section (m s^{-1}; vectors). (c) WLIS, (e) ELIS, whose locations are denoted by the red lines in (a). (d) is zoomed into the sea breeze front over WLIS, whose location is denoted by the box in (c); (f) is zoomed into the sea breeze front over ELIS, whose location is denoted by the box in (e). The uniform wind convergence (color shaded) and the NARR wind convergence (contoured) in (a), (c-f) are plotted at the same interval. The length of the vector below (f) denotes a 5 m s^{-1} 10-m wind.

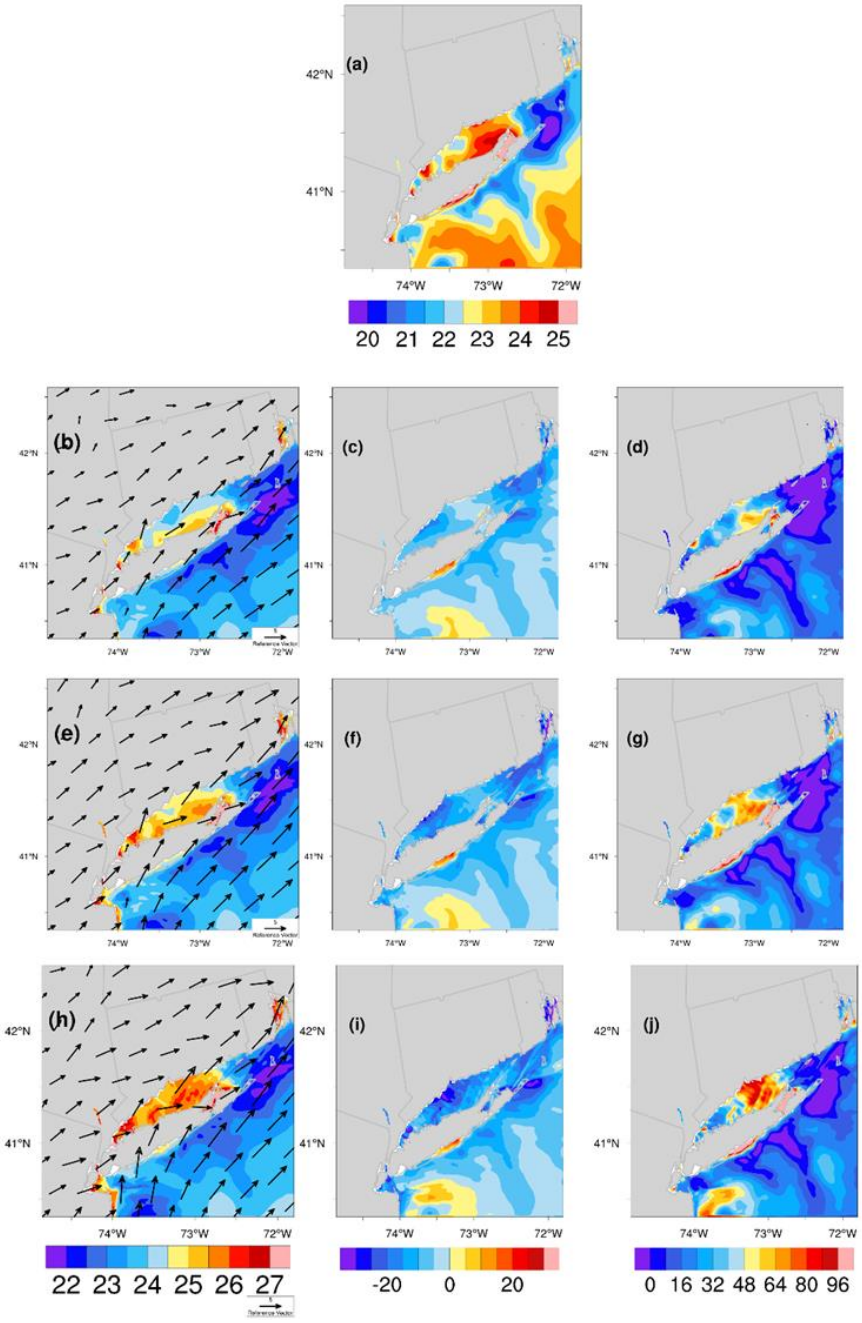

Figure 35. 08 July 2013 G1SST Results. (a) Sea Temperature (˚C); (b,e,h) 2-m temperature (˚C) with 10-m wind (m s^{-1}); (c,f,i) Surface Sensible Heat Flux (W m^{-2}); (d,g,j) Surface Latent Heat Flux (W m^{-2}). (b,c,d) is at 1500 UTC, (e,f,g) is at 1600 UTC, and (h,i,j) is at 1700 UTC. The length of the vector below (h) denotes a 5 m s^{-1} 10-m wind.

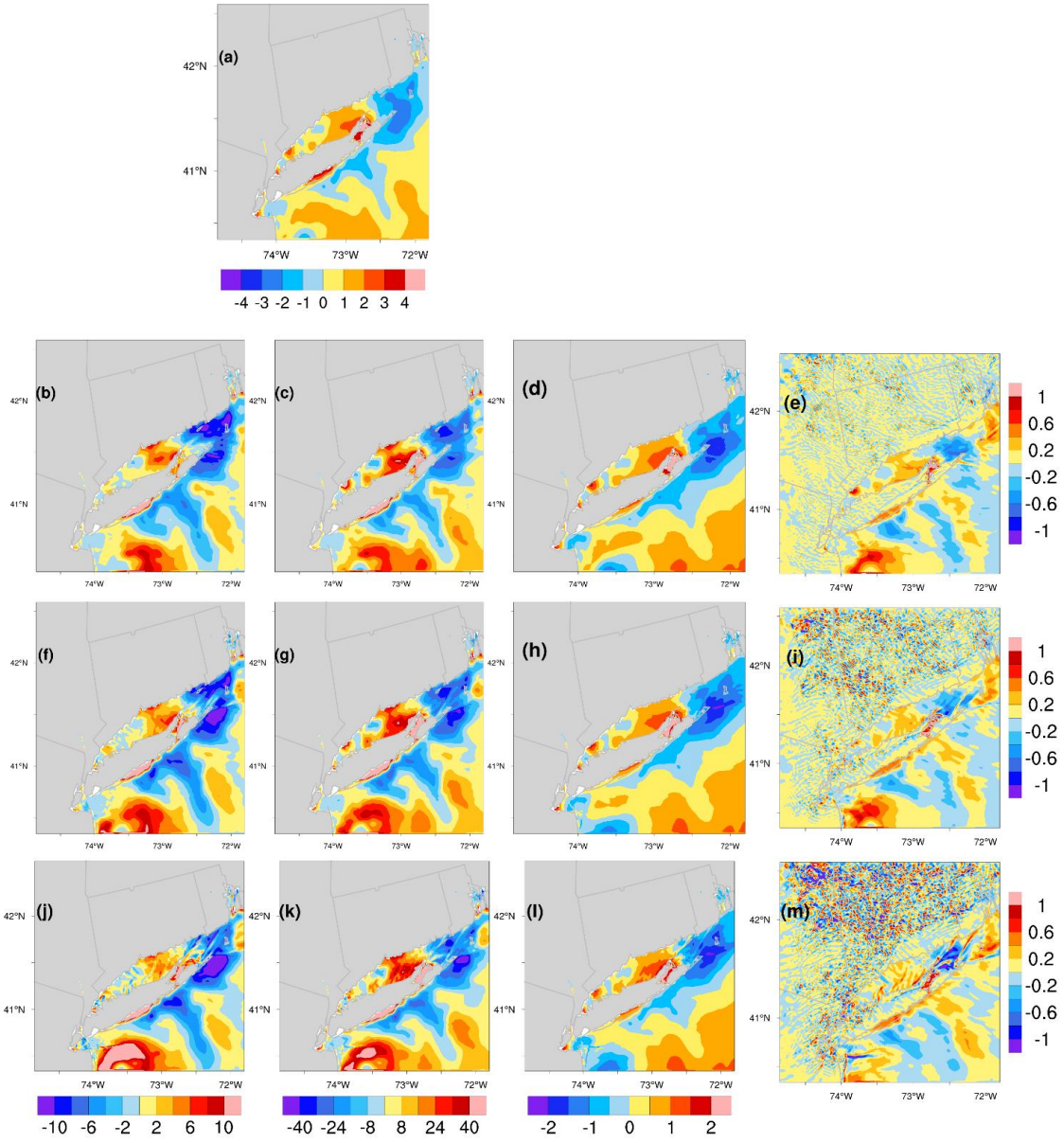

Figure 36. 08 July 2013 G1SST minus Uniform plots. (a) Sea Temperature Differences (˚C); (b,f,j) Surface Sensible Heat Flux Differences (W m^{-2}); (c,g,k) Surface Latent Heat Flux Differences (W m^{-2}); (d,h,l) 2-m Temperature Differences (˚C); (e,i,m) 10-m Wind Speed Differences (m s^{-1}). (b,c,d,e) is at 1500 UTC, (f,g,h,i) is at 1600 UTC and (j,k,l,m) is at 1700 UTC.

Table 10. 08 July 2013 1500 UTC. G1SST and Uniform Sensible Heat Flux (SHF) and the value of the term in eq. 3 that drives the SHF difference. For SHF, the driver term is $(\theta_g-\theta_a)$. Equation 3 is repeated here for convenience with the driver term highlighted in blue: $SHF = \rho c_p C_h U(\theta_g-\theta_a)$.

1500 UTC	**Uniform**	**G1SST**	**G1SST minus uniform (% change)**
WLIS			
SHF (W m^{-2})	-5.1	-6.1	-1.0 (-20%)
$\theta_g-\theta_a$ (˚C)	-4.68	-5.28	-0.6 (-13%)
CLIS			
SHF (W m^{-2})	-7.8	-3.1	4.7 (60%)
$\theta_g-\theta_a$ (˚C)	-1.40	-0.48	0.92 (66%)
ELIS			
SHF (W m^{-2})	-8.6	-17.6	-9.0 (-105%)
$\theta_g-\theta_a$ (˚C)	-1.12	-2.82	-1.7 (-152%)

Table 11. 08 July 2013 1500 UTC. G1SST and Uniform Latent Heat Flux (LHF) and the value of the term in eq. 4 that drives the LHF difference. For LHF, the driver term is (q_g-q_a). Equation 4 is repeated here for convenience with the driver term highlighted in blue: $LHF = L_e \rho M C_q U(q_g-q_a)$.

1500 UTC	**Uniform**	**G1SST**	**G1SST minus Uniform (% change)**
WLIS			
LHF (W m^{-2})	11.5	9.1	-2.4 (-21%)
q_g-q_a (g kg^{-1})	3.53	2.98	-0.55 (-16%)
CLIS			
LHF (W m^{-2})	23.6	43.0	19.4 (82%)
q_g-q_a (g kg^{-1})	1.50	2.36	0.86 (57%)
ELIS			
LHF (W m^{-2})	21.6	-2.8	-24.4 (-113%)
q_g-q_a (g kg^{-1})	0.93	-0.367	-1.30 (-139%)

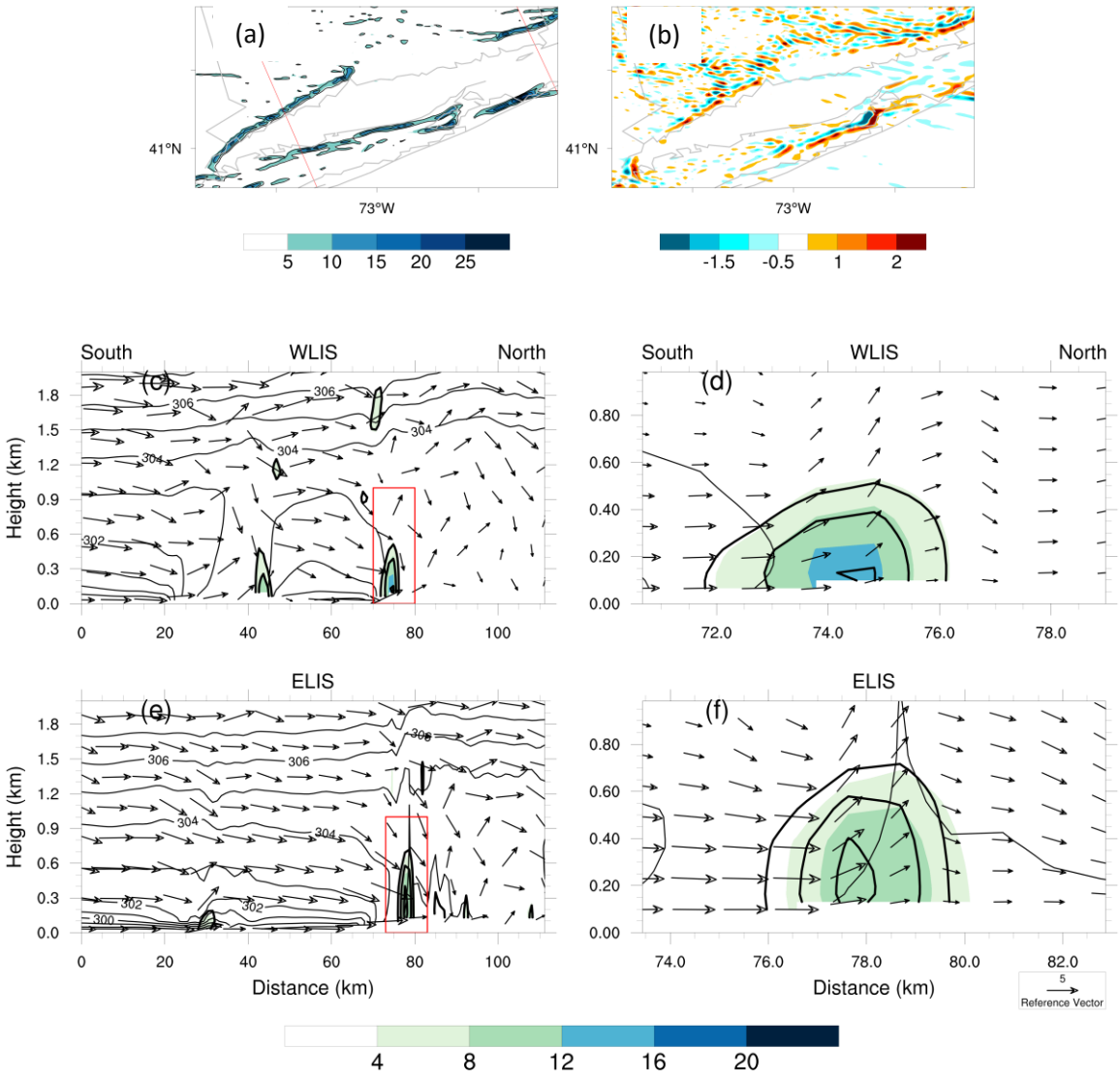

Figure 37. 08 July 2013 1500 UTC Wind Convergence. (a) the uniform wind convergence is color shaded and the G1SST wind convergence is contoured (10^{-4} s^{-1}); (b) G1SST minus uniform wind convergence plots (10^{-4} s^{-1}); (c-f) Vertical Cross sections of uniform wind convergence (10^{-4} s^{-1}; color shaded), G1SST wind convergence (10^{-4} s^{-1}; boldly contoured), virtual potential temperature (K; contoured) and wind parallel to the plane of the cross section (m s^{-1}; vectors). (c) WLIS, (e) ELIS, whose locations are denoted by the red lines in (a). (d) is zoomed into the sea breeze front over WLIS, whose location is denoted by the box in (c); (f) is zoomed into the sea breeze front over ELIS, whose location is denoted by the box in (e). The uniform wind convergence (color shaded) and the G1SST wind convergence (contoured) in (a), (c-f) are plotted at the same interval. The length of the vector below (f) denotes a 5 m s^{-1} 10-m wind.

4. Discussion and Conclusions

4.1 Introduction to Discussion

For the 21 August 2013 sea breeze, it has been shown that increasing the SST resolution has an impact on the inland progression of the sea breeze front, and therefore potentially sea breeze speed. By increasing the SST resolution, the sea breeze front is closer to the coastline over western CT and further inland over eastern CT and RI compared to the uniform simulation (fig.26 and fig.28). These differences, however, are relatively small. In the following discussion, the sea breeze speed will be quantified to confirm the impacts that the high resolution SST product has on the sea breeze front position. Once these impacts are quantified, the influence of boundary layer stability on sea breeze progression speed will be discussed. Impacts of SST resolution on surface heat fluxes will be explored on relatively long term timescales (1.5 days).

4.2 Sea Breeze Speed and Contributing Factors

Sea breeze progression speed, primarily determined by the buoyancy force resulting from the land-sea temperature gradient, can be influenced by a number of different factors, including the regional scale synoptic wind, slope of terrain, friction, and insolation (Crosman and Horel 2010; Miller et al. 2003). In the absence of these other factors, the coastal thermal gradient dominates the sea breeze propagation speed. To quantify the mechanisms controlling the propagation speed of the sea breezes examined in this study, the influence of several of those factors will be explored, beginning with the buoyancy force using a theoretical framework. The theoretical sea breeze speed will be compared to the numerical sea breeze speed, which is calculated directly from the model results.

For this discussion, the model and theoretical sea breeze speed distance is calculated in ELIS, CLIS and WLIS for the 21 August 2013 sea breeze event. For each of these regions, an

average sea breeze propagation speed and theoretical sea breeze progression speed is calculated by averaging values obtained using 17 meridional transects through the sea breeze front, spaced 1.5 km apart. The 17 transects stacked parallel to one another are 26 km wide (fig. 38).

To calculate the model sea breeze speed, the model sea breeze propagation distance is first obtained. The model propagation distance is based on the distance between the coastline and the location of the maximum wind convergence associated with the sea breeze front (fig. 38). The model sea breeze speed is calculated by taking the difference between the distance of the sea breeze front from the coastline at two consecutive model output times which are in 15 minute intervals and dividing this distance by the change in time (15 minutes). A temporal average is calculated over the mature life of the sea breeze, 1500-1800 UTC, to obtain a representative average propagation speed.

The sea breeze speed over eastern CT and RI derived from the numerical output for the uniform, NARR, and G1SST are 1.64 m s^{-1}, 1.73 m s^{-1} and 1.73 m s^{-1}, respectively (table 12). In eastern CT, these results indicate that the model sea breeze speed increases by increasing the SST resolution. By increasing the land-sea temperature gradient, cooler sea temperature values are introduced in ELIS, by 0.6˚C in the NARR (fig. 25a) and 1.9˚C in the G1SST (fig. 27a). As a result, the NARR and G1SST model sea breeze speed is 0.09 m s^{-1} larger than the uniform, though there is a minimal difference between the NARR and G1SST sea breeze speeds. Reasons for this will be addressed later in the discussion.

In CLIS, the NARR numerical sea breeze speed is the same as the uniform, while the G1SST is only 0.1 m s^{-1} higher (table 12). In WLIS, the NARR numerical sea breeze speed is 0.09 m s^{-1} higher than the uniform and the G1SST is the same as the uniform (table 12). Recall that in CLIS and WLIS, the sea temperature is higher in the NARR and G1SST products, which

produces a weaker land-sea temperature gradient, thus a slower sea breeze. The numerical model results do not support this hypothesis in WLIS and CLIS since the model speed is not decreasing with increasing SST resolution.

The theoretical sea breeze speed for each of the sensitivity experiments is calculated based on the theoretical behavior of a density current. In previous studies, a sea breeze front has been shown to act similarly to a density current (Miller et al. 2003; Robertson et al. 2013). A density current forms when a cool dense fluid interacts with a surrounding less dense warm fluid. When a cool fluid interacts with a warm fluid, a buoyancy force is established resulting in a density current, which progresses as an internal gravity wave. The internal gravity wave phase speed equation can be used to quantify the sea breeze density current speed solely due to the effects of buoyancy (eq. 5; Stull 1988).

(5) Sea breeze speed = $$\sqrt{\left(\frac{\overline{\theta_v}(sea\ breeze) - \overline{\theta_v}\ (ambient)}{\overline{\theta_v}\ (ambient)} g\right) * H}$$

In this equation, g represents Earth's gravity (9.8 m s^{-2}), θ_v(sea breeze) is the column-averaged virtual potential temperature of the sea breeze air over the vertical depth of the sea breeze, θ_v(ambient) is the column-averaged virtual potential temperature of the ambient air over the vertical depth of the sea breeze, and H is the sea breeze height. The virtual potential temperature is used so that the impact of moisture on air density is included when calculating the phase speed. Virtual potential temperature is the temperature a completely dry air parcel of air would need to be for its density to equal the density of a moist air parcel with a given specific humidity. Virtual potential temperature is used so that temperatures at multiple pressure levels throughout the depth of the sea breeze can be adiabatically brought down to a common, reference pressure level (1000 hPa). The column-averaged virtual potential temperatures are averaged from

the surface to the sea breeze height, H. Although studies have derived several different scaling mechanisms for sea breeze height (Crosman and Horel 2010), the sea breeze height in this study will be calculated graphically from the virtual potential temperature contours (virtual adiabats) from the vertical cross sections (e.g. fig. 39). The sea breeze height calculation is based on the virtual potential temperature value at the sea breeze front for each model time, since the sea breeze front changes position for each model time. This virtual adiabat at the sea breeze front is then traced to the core of the sea breeze, where the adiabat transitions from a vertical to horizontal orientation. The height of this virtual adiabat at the core of the sea breeze is considered the height of the sea breeze.

The theoretical sea breeze speed is sensitive to the location at which the virtual potential temperature associated with the sea breeze and the virtual potential temperature associated with the ambient air are column-averaged. In this study, the theoretical sea breeze speed was calculated in two scenarios. In the first scenario, the sea breeze speed is calculated with the ambient air 6.4-12.8 km north, and the sea breeze air 6.4-12.8 km south of the sea breeze front relative to the plane of the cross section (fig. 39a). In the second scenario, the column-averaged ambient air and the sea breeze air is calculated 0-6.4 km north and south from the sea breeze front, respectively (fig. 39b). These 6.4 km segments in the plane of the cross section are averaged over a 26 km width perpendicular to the cross section (as described above; fig. 38), creating a 166.4 km^2 area over which to calculate the column-averaged virtual potential temperature through the depth of the sea breeze.

The theoretical ELIS sea breeze speed was temporally averaged between 1500 UTC and 1800 UTC, as for the numerical sea breeze speed (table 12). For the uniform SST model run in ELIS, the theoretical sea breeze speed is 7.34 m s^{-1} when the sea breeze and ambient averaging

boxes are 6.4-12.8 km from the sea breeze front. In the NARR, the sea breeze speed is 7.48 m s^{-1}, and 7.50 m s^{-1} for G1SST. The NARR theoretical speed is 0.14 m s^{-1} greater than the uniform, while the G1SST is 0.16 m s^{-1} greater than the uniform. The sea breeze speed increases as the SST resolution is increased because of the larger difference the temperature between the sea breeze air and the ambient air resulting from a larger land-sea temperature gradient. A larger land-sea temperature gradient exists because of the cooler ELIS sea temperature in the NARR and G1SST relative to the uniform (fig. 25a and fig. 28a). The magnitudes of the theoretical sea breeze speed are much larger than the numerical sea breeze speed (table 12). The model sea breeze speed and the theoretical speed for the uniform, NARR and G1SST are 1.64 m s^{-1} and 7.34 m s^{-1}, 1.74 m s^{-1} and 7.48 m s^{-1}, and 1.74 m s^{-1} and 7.50 m s^{-1}, respectively. The large differences between theoretical and model sea breeze speed can be due to opposing wind, friction and terrain.

When the sea breeze and ambient averaging boxes are 0-6.4 km from the sea breeze front, the theoretical sea breeze speed is smaller, 5.22 m s^{-1} for the uniform, 5.38 m s^{-1} for the NARR, and 5.41 m s^{-1} for the G1SST. Like the first scenario, the theoretical sea breeze increases with increasing SST resolution. The NARR theoretical speed is 0.14 m s^{-1} greater than the uniform, while the G1SST is 0.17 m s^{-1} greater than the uniform. More notably, the magnitudes of the sea breeze speed have decreased substantially by moving the ambient and sea breeze averaging boxes closer to the sea breeze front. The uniform sea breeze speed has decreased 2.10 m s^{-1} (29% change), the NARR has decreased 2.10 m s^{-1} (28% change) and the G1SST has decreased 2.08 m s^{-1} (28% change).

According to the theoretical sea breeze speed results in CLIS of scenario 1, the speed decreases 0.12 m s^{-1} with increasing SST resolution (table 12). This is consistent with the

hypothesis stating a slower sea breeze results from a weaker land-sea temperature gradient, but inconsistent with the numerical model speed results which show increasing speed with SST resolution. The theoretical sea breeze speed results of scenario 2 show an 0.05 m s^{-1} increase in sea breeze speed between the uniform and NARR, and a 0.03 m s^{-1} decrease in sea breeze speed between the uniform and G1SST. The scenario 2 results suggest that the theoretical sea breeze differences are very small and thus inconsistent with the hypothesis that a warmer SST results in a weaker land-sea temperature gradient and slower sea breeze speed.

In WLIS, the theoretical sea breeze speed of scenario 1 shows an increase in speed with respect to SST resolution (table 12). The theoretical sea breeze speed increases 0.83 m s^{-1} between the uniform and NARR, and 1.00 m s^{-1} between the uniform and G1SST. Even though the SST is warmer in WLIS with respect to SST resolution creating a weaker land-sea temperature gradient, the sea breeze speed increases. In scenario 2, the sea breeze speed also generally increases with respect to SST resolution 1.89 m s^{-1} between the uniform and NARR, and increases 1.71 m s^{-1} between the G1SST and NARR (table 12).

There are two reasons that contribute to why the model and theoretical sea breeze speed increases with SST resolution in WLIS and CLIS. The numerical and theoretical sea breeze speed increases with SST resolution even when the SST increases in WLIS and CLIS because of the temporal averaging. At 1700 UTC and later, the sea breeze front position differences become noisy due to the influences of terrain and friction, which causes the sea breeze front in the uniform, NARR and G1SST to progress in directions no longer perpendicular to the coastline. Secondly, the reason why the theoretical sea breeze speed increases with SST resolution in WLIS and CLIS is because of the position of the sea breeze front relative to the vertical virtual adiabats. For example, in WLIS, the G1SST sea breeze air mass box (box outlined in blue) is in

contact with more of the cool sea breeze air than the uniform sea breeze air mass box at 1500 UTC for scenario 2 (fig. 40). This causes the G1SST sea breeze air mass box to be cooler than the uniform sea breeze air mass box. Since the wind convergence-defined G1SST sea breeze front has not progressed as far inland as the uniform sea breeze front, the G1SST sea breeze air has not been as much affected by the impacts of land surface solar heating. Consequently, the G1SST sea breeze air mass box is slightly cooler than the uniform sea breeze air mass box, which results in a larger temperature difference between the sea breeze air mass box and the ambient air mass box in the G1SST, causing a deceptively faster theoretical sea breeze speed in the G1SST than the uniform.

Although the theoretical and numerical sea breeze speed generally increase with SST resolution in CLIS and WLIS, the theoretical sea breeze speed substantially decreases when using the sea breeze and ambient air masses within 0-6.4 km of the sea breeze front. In WLIS, the sea breeze speed decreases 1.83 m s^{-1} for the uniform, 1.72 m s^{-1} for the NARR and 1.74 m s^{-1} for the G1SST. In WLIS, 2.76 m s^{-1} for the uniform, 1.7 m s^{-1} for the NARR, and 2.05 m s^{-1} for the G1SST. Like with ELIS, CLIS and WLIS theoretical sea breeze speed is closer to the numerical sea breeze speed when the ambient air masses are calculated within 0-6.4 km of the sea breeze front, which indicates that it is likely more correct to calculate theoretical sea breeze speed using scenario 2 (table 12).

The decrease in theoretical sea breeze speed from scenario 2 to scenario 1 in WLIS, CLIS and ELIS has allowed the theoretical sea breeze speed to become more comparable to the numerical sea breeze speed. By averaging the sea breeze and ambient virtual potential temperature closer to the sea breeze front, the theoretical sea breeze speed in ELIS has become 36.8% closer to the model sea breeze speed for the uniform run, 36.6% for the NARR run, and

36.1% for the G1SST run. In CLIS, the theoretical sea breeze speed has become 32% closer to the model sea breeze speed for the uniform run, 31% for the NARR run, and 31% for the G1SST run. In WLIS, the theoretical sea breeze speed has become 61% closer to the model sea breeze speed for the uniform run, 33% for the NARR run, and 38% for the G1SST run. Although theoretical sea breeze speed has substantially decreased by adjusting the air masses within 0-6.4 km of the sea breeze front, the numerical sea breeze speed is still considerably lower in WLIS, CLIS and ELIS (tables 12).

The theoretical sea breeze speed is ~30% closer to the numerical sea breeze speed when using the air masses within 0-6.4 km of the sea breeze front (scenario 2) due to surface heating of the land. A portion of the sea breeze air overlies the land during the majority the sea breeze. The land heats up due to solar heating, which increases the sea breeze air temperature through land surface heat fluxes. When the sea breeze air temperature increases due to the upward surface heat fluxes from the land surface, the difference in temperature between the sea breeze air and the ambient air decreases, which decreases the theoretical sea breeze speed. When the sea breeze averaging box representative of the sea breeze air is 6.4-12.8 km from the sea breeze front, the sea breeze air does not make as much contact with the land surface compared to when the sea breeze averaging box is only 0-6.4 km from the sea breeze front. Robinson et al. (2013) has performed a similar analysis studying effects of surface heating on the sea breeze density current using an idealized numerical modeling framework. In this study, they calculated the sea breeze density current speed from the model output. Using WRF, they performed numerical sensitivity experiments for a sea breeze event including and excluding solar heating. Transitioning from no solar heating to $5x10^5 J\ m^{-2}$ solar heating, the sea breeze speed dropped from 2.5 m s^{-1} to 1.9 m s^{-1} with a 1.7 km sea breeze height (Robinson et al. 2013).

In some cases, synoptic wind, which can oppose propagation direction of the sea breeze front, can have a substantial effect on the speed of the sea breeze density current (Porson et al. 2007; Miller et al. 2003; Crosman and Horel 2010). Porson et al. (2007) explored the sensitivity of sea breeze to opposing wind using the topographic vorticity mesoscale model (TVM). When a relatively weak 2.5 m s^{-1} opposing wind was included, the sea breeze front moved 22.5 km inland. The inland progression of the sea breeze decreased for increasing wind speed, moving 7.5 km inland with a 5 m s^{-1} opposing wind and 2.5 km inland with a 6 m s^{-1} opposing wind.

When the theoretical sea breeze speed is calculated, synoptic wind is not considered. Given the effects synoptic wind can have on sea breeze speed (Porson et al. 2007), it is important to determine the impact of the synoptic wind in the 21 August 2013 sea breeze simulation, which may be contributing to the smaller numerical sea breeze speed numerical sea breeze speed compared to theory. To quantify the effects of synoptic wind, an average of the geostrophic wind north of the sea breeze front parallel to the plane of the previous cross sections is computed. The synoptic wind will also be averaged over the 26 km width shown in fig. 38, column-averaged from the surface to the depth of the sea breeze and temporally averaged from 1500 UTC and 1800 UTC. Positive synoptic wind speeds are the same direction and negative speeds are the opposite direction of the sea breeze front propagation. The synoptic wind speed is small during the 21 August 2013 sea breeze event for the uniform, NARR and G1SST simulations in WLIS, CLIS and ELIS (table 12). Furthermore, the synoptic winds in WLIS, CLIS and ELIS are the same direction of the sea breeze front progression. The column-averaged synoptic winds range from 0.7 to 0.84 m s^{-1} in WLIS, 0.09 to 0.2 m s^{-1} in CLIS and 1.03 to 1.05 m s^{-1} in ELIS. Therefore, synoptic wind does not have a large effect on the sea breeze front speed.

The relatively large differences between the theoretical sea breeze speed and model sea

breeze speed for the uniform, NARR and G1SST, and for WLIS, CLIS and ELIS indicate that the sea breeze density current does not resemble a pure density current. These differences can be quantified using the Froude number, which is the ratio of the model sea breeze speed and the theoretical sea breeze speed (eq. 6; Robinson et al. 2013; Carbone et al. 2000). A Froude number close to 1 would indicate the model sea breeze speed closely resembles a pure density current, which is quantified by the theoretical sea breeze speed. The farther the Froude number deviates from 1, the less the model sea breeze speed resembles a pure density current. The Froude numbers of the first scenario are relatively low, ranging from 0.15 to 0.25 (table 12). The Froude numbers of the second scenario, however, are larger, ranging from 0.21 to 0.32, which is a 35% to 43% increase from the first scenario. These results indicate that when we define our theoretical sea breeze density current based on the sea breeze and ambient air 0 to 6.4 km from the sea breeze front, the model sea breeze density current more closely resembles a pure density current.

$$\text{(6) Froude Number} = \frac{\text{Model Sea Breeze Speed}}{\text{Theoretical Sea Breeze Speed}}$$

It is also important to consider a comparison between the land-sea temperature gradient and the horizontal SST gradient between WLIS and ELIS. The WLIS land-sea temperature gradient is calculated based on the difference between the WLIS model buoy location and the HPN model land site. The CLIS and ELIS land-sea temperature gradients are respectively based from the CLIS model buoy location and HVN model land site, and the ELIS model buoy location and the GON model land site. Table 13 shows that the land-sea temperature gradients are larger than the horizontal SST gradients during the sea breeze developing state (1500 UTC), and these differences between the gradients grow as the sea breeze matures. For example, for the

G1SST simulation, where the horizontal gradient is largest relative to the NARR and uniform SST, the horizontal SST gradient is 3.1˚C, while the land-sea temperature gradient ranges from 10.6˚C to 15.4˚C at 1500 UTC and 13.9˚C to 17.2˚C at 1700 UTC (table 13). The land-sea temperature gradient ranges from 242% to 397% larger than the horizontal G1SST gradient at 1500 UTC, and 348% to 455% greater at 1700 UTC. The percentage changes increase as the sea breeze matures because of the land temperature's response to solar insolation. These results indicate that the land-sea temperature gradients are more important than the horizontal SST gradients, and this importance grows as the sea breeze matures. Furthermore, values from table 13 indicate that by increasing the horizontal SST gradient, the land-sea temperature gradient doesn't change nearly as much. For example, when adjusting the horizontal SST gradient from 0˚C (uniform SST) to 3.1˚C (G1SST SST), the land-sea temperature gradient between the G1SST and uniform sensitivity experiments only changes 0.9 ˚C in WLIS, 0.1˚C in CLIS and -1.2˚C in ELIS for 1500 UTC. For 1700 UTC, the land-sea temperature gradient between the G1SST and uniform changes 1.0 ˚C in WLIS, 0.5˚C in CLIS and -1.4˚C in ELIS, which does not far exceed the changes at 1500 UTC. Therefore, when we adjust from a uniform to a horizontal SST gradient, the changes in land-sea temperature gradients are relatively small, which contributes to the small changes in sea breeze speed in the SST resolution sensitivity experiments.

4.3 Stability effects on sea breeze

The propagation speed of the sea breeze front was minimally impacted by variations in the SST product. For example, the sea breeze speed in ELIS only increased 0.09 m s^{-1} when using a high resolution SST product. In CLIS and WLIS, the sea breeze speed only increases 0.1 m s^{-1}, which is opposite in sign from what is predicted by the buoyancy force. Since geostrophic

wind appears to have minimal impact on the propagation speed during this event, it is important to explore the influence of other factors, such as the marine atmospheric boundary layer stability on propagation speed.

Figure 41 shows the cross sections perpendicular to the 21 August 2013 sea breeze front over WLIS, CLIS and ELIS, with the cross section location as shown in figure 26a. Since there are small temporal variations in the temperature changes from 1500 to 1700 UTC, only 1500 UTC virtual potential temperature differences will be explored. The virtual potential temperature from the uniform SST simulation is contoured in black, with the virtual potential temperature difference between the G1SST and uniform SST simulations shaded. Figure 41(a,c,e) plot up to 1.6 km into the boundary layer, while figure 41(b,d,f) plot up to only 600 meters of the boundary layer. Within the sea breeze layer, differences in virtual potential temperature between G1SST and uniform are 0.2˚C at 100 m in WLIS, 75 m in CLIS, 300 m in ELIS (fig. 41). Virtual potential temperature differences comparable to the virtual potential temperature differences seen at 2-m (0.5˚C) only are between 50 m in WLIS, 30 m in CLIS and 50 m in ELIS. The largest virtual potential temperature changes occur in ELIS UTC (fig.41f), where the virtual potential temperature changes between 0.2 ˚C and 1.3˚C extend 300 meters (or 30%) into the sea breeze layer. The virtual potential temperature changes in ELIS extend the furthest into the sea breeze layer because of the larger differences in sea temperature between the G1SST and uniform run compared to CLIS and ELIS. In ELIS, G1SST sea temperature is 2.5˚C cooler than the uniform, whereas in CLIS and WLIS, G1SST is respectively 1.5˚C and 1.3˚C warmer than the uniform.

The virtual potential temperature variations due to differing SST products must extend vertically throughout the depth of the sea breeze layer impact the speed of the sea breeze front. Anomalies confined to the lowest levels of the boundary layer will not substantially contribute to

the changes in the overall thermal gradient across the sea breeze front. The internal gravity wave phase speed equation (eq. 5) supports this conceptual understanding. Based on this equation, the sea breeze speed depends on the differences in virtual potential temperature across the sea breeze front through the depth of the sea breeze layer, not just the near-surface layer. Since the largest virtual potential temperature differences between the 2 simulations only occur within 100 meters of the surface with minimal differences throughout the rest of the sea breeze layer, the column-averaged vertical potential temperature will remain relatively unchanged.

Differences in the virtual potential temperature are constrained to the lowest 100 meters, in part, due to the high static stability. Static stability is quantified using buoyancy frequency (N^2; eq. 6), depends on gravity, virtual potential temperature, and the vertical potential temperature gradient. When N^2 is greater than 0, the atmosphere is considered statically stable. When N^2 is less than 0, the atmosphere is considered statically unstable, allowing for mixing through the layer.

$$(7)\ N^2 = \frac{g}{\theta_v}\frac{\partial \theta_v}{\partial z}$$

The buoyancy frequency results show that the sea breeze layer is statically stable (9-10x10^{-4} s^{-2}) below 100 meters over ELIS, CLIS and WLIS for the uniform, NARR and G1SST SST sensitivity experiments (fig. 42 and fig. 43). The buoyancy frequency above 100 meters but within the sea breeze layer is a less statically stable, 0 to 2x10^{-4} s^{-2}, which is an order of magnitude smaller than the buoyancy frequency below 100 meters. Furthermore, increasing the SST resolution to 1 km, contributes to increased static stability over ELIS (1x10^{-4} s^{-2} more stable) and decreased static stability over WLIS and CLIS (0.8x$10^{-4}s^{-2}$ less stable). The larger buoyancy frequency over ELIS is due to the cooler SST in the G1SST compared to the other

SST products, while reduced buoyancy frequency over WLIS and CLIS is due to the warmer SST.

Although large buoyancy frequency values confirm the presence of high static stability in the lower MABL, the effects of wind shear need to be considered when assessing turbulent mixing within the boundary layer. A large static stability does not guarantee minimal turbulent mixing, especially when there is a high wind shear, which is a measure of dynamic stability. For example, if there is a high static stability but a high dynamic stability due to large wind shear, turbulent mixing can still exist. To quantify mixing in the MABL, the gradient Richardson number should be assessed, which is the ratio of the static stability to the dynamic stability (eq. 8). In the numerator is N^2, which is the buoyancy frequency (static stability), whose equation is shown in equation 7. The u and v wind components of the wind shear are each squared in the denominator, which quantifies the dynamic stability. When the Richardson number is greater than 1, vertical turbulent mixing is unlikely (Stull 1988). When the Richardson number is less than 1, vertical turbulent mixing is likely.

$$(8)\quad Ri = \frac{N^2}{(\frac{\partial u}{\partial z})^2+(\frac{\partial v}{\partial z})^2}$$

The Richardson numbers for WLIS, CLIS and ELIS for the uniform and G1SST are overall above 1 over the MABL, indicating vertical turbulent mixing is unlikely (fig. 44 and 45). The relatively lower Richardson numbers at the near-surface of the MABL are due to the relatively high wind shear terms of ~$2x10^{-2}$ s^{-1}, ~$1x10^{-2}$ s^{-1} and ~$1x10^{-2}$ s^{-1} over ELIS, CLIS and WLIS, respectively, resulting from the onshore sea breeze wind. The wind shear term above 100 meters is at most on the order of10^{-3} s^{-1}, which is at least one order of magnitude smaller than wind shear below 100 meters. Nevertheless, the overall high Richardson numbers through the

depth of the sea breeze layer suggest that the sea breeze layer remains unmixed. Therefore, changes made to the ocean surface temperature by increasing the SST resolution remain confined to the lowest levels of the sea breeze layer due to an environment that inhibits turbulent mixing.

In summary, the differences in sea breeze front speed between the SST sensitivity experiments during the 21 August 2013 event are due to relatively small temperature changes, which are constrained to the lowest 100 meters of the MABL. High buoyancy frequency and high Richardson numbers encourage less mixing, which prevents the influence of the surface fluxes on the temperature of the overlying atmosphere from propagating through the rest of the sea breeze layer, thus having little impact on the speed of the sea breeze.

The model surface buoyancy flux (W m^{-2}) can help determine whether the overlying atmosphere is becoming more or less buoyant as a result of surface sensible and latent heat fluxes during the sea breeze event (eq. 9; Stull 1988). In equation 9, $\overline{w'\theta'}$ is the kinematic heat flux (K m s^{-1}), $\overline{w'q'}$ is the kinematic moisture flux (m s^{-1}), q_{2m} is the 2-m mixing ratio and θ_{2m} is the 2-m potential temperature (K). The other terms were introduced in equations 3 and 4. A positive buoyancy flux indicates that the surface is becoming more buoyant, contributing to the production of turbulence in the lower MABL. A negative buoyancy flux indicates that the surface is becoming less buoyant, inhibiting turbulence.

(9) Buoyancy flux = $\rho c_p[\overline{w'\theta'}(1+0.61q_{2m})+0.61\theta_{2m}\overline{w'q'}]$ (Stull 1988)

The buoyancy flux confirms that the ocean is driving an increase in buoyancy to the atmosphere during the developing stage (1500 UTC) of the sea breeze for the uniform and NARR simulations, with values ranging from 4 to 6 W m^{-2} (fig 46a-b). Given that the sea breeze layer is stable as indicated by the high Richardson numbers (fig. 44 and fig. 45), the MABL is

becoming more buoyant and ultimately less stable (fig. 46a-b). For the G1SST simulation, negative buoyancy flux (-1 W m^{-2}) occurs over ELIS, therefore the ocean is driving a decrease in buoyancy to the atmosphere. The negative buoyancy flux over ELIS in the G1SST is occurring fundamentally because of the relatively cool SST. In CLIS and WLIS, the buoyancy flux is considerably larger (6-8 W m^{-2}) relative to the uniform simulation, which indicates that the surface layer is contributing to a less stable sea breeze layer than in the uniform and NARR simulations. The larger buoyancy flux in WLIS and CLIS relative to the uniform and NARR simulations is due to the warm G1SST. In WLIS and CLIS, the positive buoyancy fluxes encourage turbulent mixing, and the negative buoyancy fluxes in ELIS inhibit turbulent mixing. As the sea breeze matures, while the relative differences between the SST resolution experiments remain similar, the buoyancy flux generally decreases for the uniform, NARR and G1SST over WLIS, CLIS and ELIS with respect to time (fig. 46d-i). Therefore, buoyancy production to the atmosphere is decreasing, which ultimately contributes to a decrease in production of turbulence to the atmosphere.

While sea temperature changes due to variations in the SST resolution are relatively small, the sea temperature changes due to variations in the representation of the coastline in the numerical model can be large enough to substantially decrease the stability of the MABL, allowing appreciable virtual potential temperature changes to extend throughout the sea breeze layer. For example, during the 08 July 2013 sea breeze event, large virtual potential temperature differences are seen in the coastline sensitivity experiments between *OrigCoast_day* and *HRCoast_day* over WLIS. In figure 47a, *OrigCoast_day* is 1.0˚C warmer than *HRCoast_day* between 200 m and 500 m over WLIS, where the sea breeze height is 900 m. *OrigCoast_day* is 2.0˚C warmer than *OrigCoast_day* between 100 m and 200 m. Below 100 meters, the virtual

potential temperature exceeds 3.0˚C. These appreciable changes in virtual potential temperature extend through about half the sea breeze layer (300 m) because of the unstable sea breeze layer in *OrigCoast_day* (fig. 47b). The buoyancy frequency is near zero in *OrigCoast_day*. This low stability sea breeze layer allows more mixing of warm air in the *OrigCoast_day* than the *HRCoast_day*. These vertical cross sections of buoyancy frequency further explain why such large changes in the position of the sea breeze front can be seen in the wind convergence maps (fig. 21e).

4.4 Long Term SST Influences

While the large differences in surface heat fluxes between sensitivity experiments had a minimal impact on the sea breeze propagation speed and vertical structure, they could have implications for phenomena on longer time scales. To quantify how the differences in surface heat flux accumulate over longer time scales, the sensible and latent heat fluxes will be time integrated to obtain accumulated latent and sensible heat flux. Figure 48 shows accumulated heat flux over 27 hours from 21 August 2013 1200 UTC to 22 August 2013 1500 UTC (fig. 48). The model initialization time is 0300 UTC 21 August 2013, giving the model a 9-hour spin up. The accumulated heat flux differences increase as time progresses. In WLIS after 27 hours, the accumulated sensible heat flux increases 0.91×10^5 J m^{-2} (17%) by changing from the uniform to NARR SST, and increases 1.47×10^5 J m^{-2} (27%) between the uniform and G1SST. In CLIS, the accumulated sensible heat flux decreases 0.58×10^5 J m^{-2} (37%) for the NARR, and decreases 0.46×10^5 J m^{-2} (29%) for the G1SST. In ELIS, the accumulated sensible heat flux decreases 1.43×10^5 J m^{-2} (64%) for the NARR, and 4.40×10^5 J m^{-2} (200%) for the G1SST. These results indicate that as the resolution of the SST product increases, more sensible heat is transferred from the ocean to the atmosphere over WLIS and less sensible heat is transferred from the ocean

to the atmosphere over ELIS after 27 hours, which is because of the cooler SST in ELIS and the warmer SST in WLIS.

For the accumulated latent heat flux, the differences between the three sensitivity experiments also increase as time progresses. After 27 hours for WLIS, the accumulated latent heat flux increases 0.33×10^6 J m^{-2} (19%) between the uniform and the NARR, and increases 1.21×10^6 J m^{-2} (68%) between uniform and G1SST. For CLIS, the accumulated latent heat flux decreases 0.17×10^6 J m^{-2} (6.7%) for the NARR, and increases 0.45×10^6 J m^{-2} (18%) for the G1SST. For ELIS, the accumulated latent heat flux decreases 1.22×10^6 J m^{-2} (34%) for the NARR, and 2.63×10^6 J m^{-2} (74%) for the G1SST. These results indicate that after 27 hours, there is more latent heat transferred from the ocean to the atmosphere over WLIS and less latent heat transferred from the ocean to the atmosphere over ELIS, by increasing the resolution of the SST. There is a smaller latent heat flux over ELIS because of the relatively cool SST in the G1SST compared to the other sensitivity experiments, and a greater latent heat flux over WLIS because of the relatively warm SST.

With accumulated sensible and latent heat fluxes considered, it is also important to acknowledge other accumulated surface heat fluxes such as longwave and shortwave radiation to further assess the potential impacts of SST resolution on longer time scales. Net surface longwave radiation is defined as the upward minus the downward longwave radiation. Therefore, a positive net longwave radiation indicates surface cooling and a negative net longwave radiation indicates a surface warming. Accumulated net longwave radiation results show substantial differences arise after 27 hours (fig. 49). In WLIS, the net surface accumulated longwave radiation increases 0.29×10^6 J m^{-2} (6.4%) between the uniform and NARR, and 0.59×10^6 J m^{-2} (13%) between the uniform and G1SST. In CLIS, the differences between the uniform and the

NARR are negligible (1.8%), but increases $0.16x10^6$ J m^{-2} (2.8%) between the uniform and G1SST. In ELIS, there are decreases of $0.47x10^6$ J m^{-2} (8.5%) between the uniform and NARR, and $1.16x10^6$ J m^{-2} (21%) between the uniform and G1SST. According to the Stefan-Boltzman law, the longwave radiation emitted from a grey body is proportional to the fourth power of the surface temperature. Therefore, when the sea temperature increases or decreases, the longwave radiation respectively increases or decreases (Simpson and Sharples 2012; Stull 1988). This relationship also applies to accumulated longwave radiation. Thus, the larger accumulated longwave radiation in the NARR and G1SST relative to the uniform in WLIS is due to the warmer sea temperature, and the smaller accumulated longwave radiation in ELIS is due to the cooler sea temperature. While the accumulated sensible, latent and longwave radiation are sensitive to changes in the ocean surface boundary conditions, the accumulated shortwave radiation is much less sensitive to changes in SST resolution at WLIS, CLIS and ELIS (fig. 50). The net shortwave radiation is defined as the reflected shortwave radiation minus the incoming shortwave radiation. Therefore, a positive net shortwave radiation indicates surface cooling and a negative net shortwave radiation indicates surface heating. The surface net shortwave radiation primarily depends on sun angle, cloud cover and albedo (Simpson and Sharples 2012). None of these variables depend on the ocean surface boundary condition. Therefore, adjustments to the ocean surface boundary conditions have minimal impact on the surface net shortwave radiation.

With all the heat fluxes considered, it is important to determine if there are differences in the accumulated net surface heat flux, which is the sum of the net surface shortwave, longwave, sensible and latent heat fluxes. After 27 hours for WLIS, the accumulated net surface heat flux increases $0.045x10^7$ J m^{-2} (2.2%) between the uniform and the NARR, and increases $0.19x10^7$ J m^{-2} (9.1%) between the uniform and G1SST (fig. 51a). In CLIS, accumulated net surface heat

flux differences between the NARR and uniform are negligible (0.8%), but increases 0.06×10^7 J m^{-2} (3.1%) between the uniform and G1SST (fig. 51b). In ELIS, the accumulated net surface heat flux decreases 0.17×10^7 J m^{-2} (10.0%) between the uniform and NARR, and decreases 0.35×10^7 (21.1%) between the uniform and G1SST (fig. 51c). The increases in net surface heat flux in the NARR and G1SST over WLIS are essentially due to a warmer SST, and the decreases over ELIS are due to a cooler SST. Even with the net shortwave radiation included in the accumulated net surface heat fluxes (where shortwave differences are minimal), the differences in the net surface fluxes between the SST resolution experiments are as large at 10% over WLIS and ELIS.

Given the accumulated net heat flux, a theoretical, dynamic SST can be calculated to estimate the impacts of a dynamic SST (eq. 10; Stull 1988). h is the depth of the ocean mixed layer, c_p is the heat capacity of water at constant pressure and ρ is the ocean density (1000 kg m^{-3}) at the mixed layer. SST_0 is the initial ocean temperature, whose values will be prescribed by the static model sea temperature. The $\frac{\text{Accumulated net surface heat flux}}{\rho c_p h}$ term quantifies the SST perturbations. For WLIS, CLIS and ELIS, an ocean mixed layer depth of 20 meters is used. For WLIS, CLIS and ELIS, and for uniform, NARR and G1SST, the dynamic SST deviates very little from the static SST (fig. 52). For WLIS from 21 August 2013 1200 UTC to 22 August 2013 1500 UTC (27 hours), the root mean squared error (RMSE) between the dynamic SST and static SST is 0.0398˚C, 0.0378˚C and 0.0350 ˚C for the uniform, NARR and G1SST, respectively. CLIS and ELIS have comparable RMSE values (table 14). These small RSME values indicate that by using a dynamic SST, the values do not substantially vary from the static SSTs. The lack of temporal variations in the dynamic SST are due to the relatively large depth of the ocean mixed layer. According to equation 10, the larger the mixed layer depth, the smaller the SST

perturbations. If the mixed layer depth were smaller, like it is for a land surface, the temperature perturbations would be considerably larger. With smaller mixed layer depths, temporal temperature variations become more important at time scales of 27 hours and less, hence why a dynamic land temperature is used in the model. Overall, these theoretical SST results suggest that weather phenomena for time scales up to 27 hours will not be largely impacted between a dynamic SST and static SST.

$$(10)\ SST = SST_o + \frac{\text{Accumulated net surface heat flux}}{\rho c_p h}$$

4.5 Practical Broad-Scale Implications and Extrapolations of Results

The large differences in sea breeze circulation in the coastline sensitivity experiments can have large impacts on local utility companies. For example, with the August *OrigCoast_day* sea breeze circulation 8 km less inland than *HRCoast_day*, utility companies will have a difficult time scheduling when to decrease the electrical load on power grids. If a local utility company in New Haven, CT follows a sea breeze forecast initialized with a coarse initial condition product, the utility company will schedule a decrease in their electrical load during the actual sea breeze, which would be too late due to the model underestimation of the sea breeze strength. If a utility company follows a sea breeze forecast initialized with a high resolution initial condition product, the utility company will be able to schedule a decrease in their electrical load closer to the time of the onset of the sea breeze. In this case, if utility companies follow a forecast initialized with a high resolution initial condition product, these companies will be able to schedule a decrease in the electrical load earlier in the day, which can potentially reduce the risk of electrical overload. Overall, understanding the importance of a high resolution initial condition for CT sea breeze simulations through hindcasts in this study will allow meteorologists to be more cautious for forecasting future sea breezes, which will result in optimal preparations by various industries

such as electrical utility companies.

Although there were small changes in the sea breeze circulation in the SST resolution sensitivity experiments over coastal CT due to high stability over the sea breeze layer, SST resolution can have larger impacts on sea breeze circulation in regions with lower MABL stability. SST resolution can have larger impacts in regions such as east coastal Florida (LaCasse et al. 2008). Although this study did not primarily focus on the impacts of SST resolution of sea breeze, they found that there are large changes in the nocturnal MABL height over the Florida Current between the high resolution MODIS and lower resolution RTG SST products. For easterly (onshore) flow, the MABL height over the Florida current is 120 meters deeper in the MODIS compared to the RTG, which is where the MODIS SST is warmer than the RTG SST. Over the Florida–Hatteras shelf, where the MODIS SST is cooler than the RTG SST, the MODIS MABL height is 100 meters shallower than the RTG. According to LaCasse et al. (2008), these changes in MABL height are driven by the SST changes primarily through the large sensible heat flux changes. In this particular region of study, the MABL static stability is relatively low during nocturnal easterly flow as indicated by changes in potential temperature with respect to height. Between the surface and 920 hPa isobars, the potential temperature remains between 294 K and 295 K for the RTG and MODIS simulations over the Florida Current and Florida–Hatteras shelf (LaCasse et al. 2008). These potential temperature changes with respect to height are small relative to the findings of the SST resolution sensitivity experiment results (fig. 26, 29,34,37 light contours), where the potential temperature increases about 5K with respect to height within the sea breeze layer, which indicates a higher static stability. Therefore, when the MABL static stability is relatively low, SST resolution can have large impacts on the boundary layer.

4.6 Concluding Remarks

In the coastline sensitivity experiments, by increasing the resolution of the initial condition product, large changes in the sea breeze circulation across coastal CT resulted. In the July and August sea breeze cases, there are up to 8 km differences in the sea breeze front location between the *OrigCoast_day* and *HRCoast_day* fundamentally because of the large sea temperature differences between ocean and land at 2100 UTC. These large sea temperature differences cause the NARR coastline modification to have substantial effects on the initial sea temperature results, and consequently the land-sea temperature gradient during the sea breeze.

In the SST resolution sensitivity experiments, by increasing the SST resolution on Long Island Sound sea breeze, a cooler SST is prescribed in ELIS, and a warmer SST in WLIS and CLIS. As a result, the land-sea temperature gradient increases in ELIS and decreases in CLIS and WLIS. Consequently, the land-sea temperature differences result in a sea breeze that propagates 1 km farther inland over eastern CT and RI and propagates 2-3 km less inland over central and western CT for the 21 August 2013 sea breeze. The differences in sea breeze front position are relatively small because the sea breeze virtual potential temperature differences are confined to the lowest 100 meters, which is only ~10% of the sea breeze layer, due to the stability of the MABL. The impact of the surface heat fluxes due to the varying SST do not impact the full depth of the sea breeze layer in part due to the high static stability and relatively high Richardson numbers between the surface and 100 m, which prevents the low level virtual potential air temperature changes to mix throughout the depth of sea breeze. In the 08 July 2013 sea breeze, the sea breeze front position differences are also small. In future work, although differences in sea breeze circulation exist by adjusting the SST resolution, it should be

understood that sea breeze circulation is relatively insensitive to SST resolution when the MABL stability is high in estuarine regions.

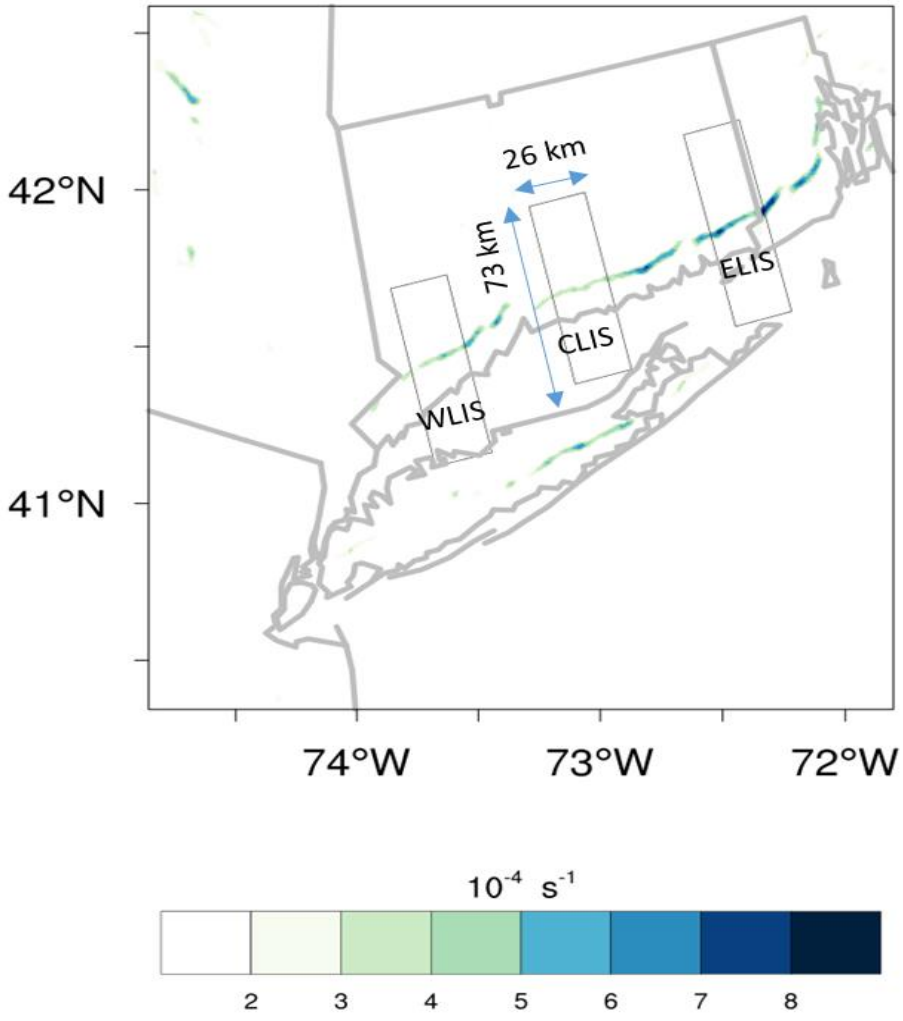

Figure 38. 21 August 2013 1600 UTC wind convergence. Three averaging domains are displayed for WLIS, CLIS and ELIS. Each box has a length of 73 km and a width of 26 km. Each box contains 17 vertical cross sections perpendicular to the Connecticut coast.

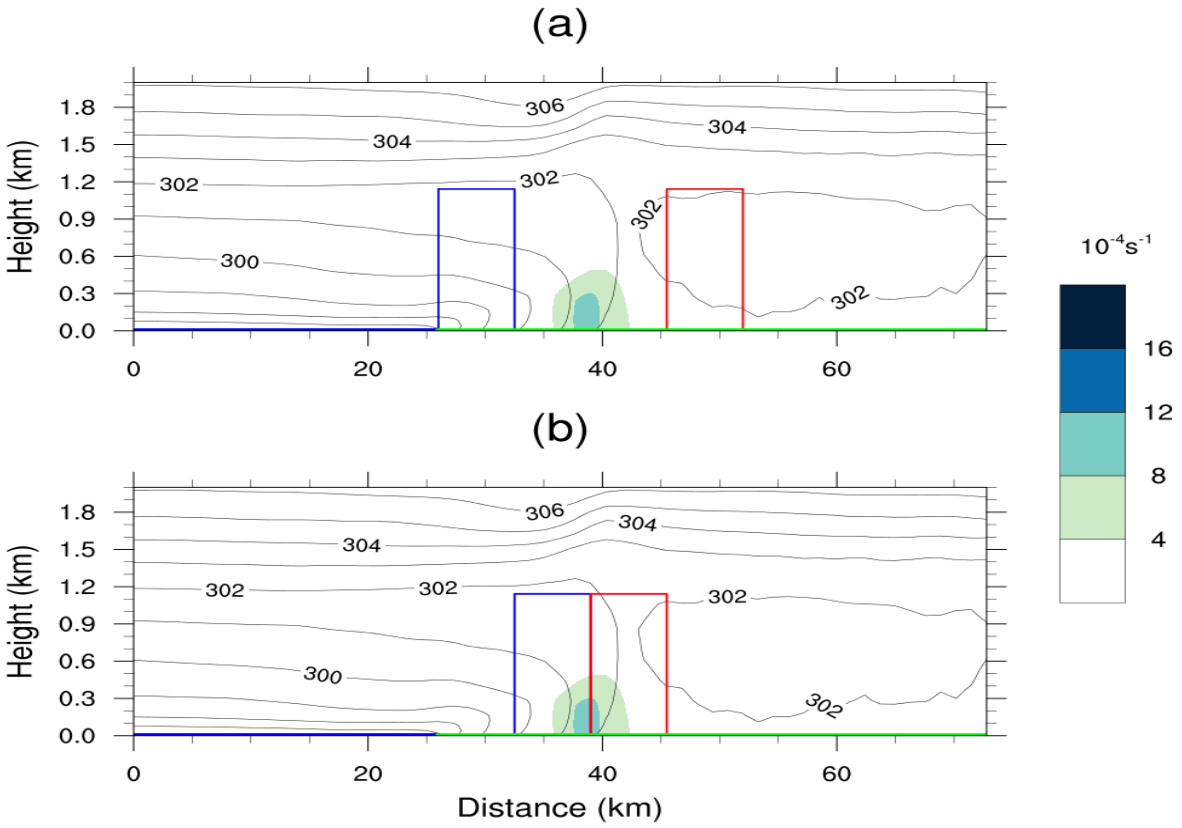

Figure 39. 21 August 2013 1600 UTC ELIS. sea breeze air (blue box) and ambient air (red box) locations for (a) scenario 1 and (b) scenario 2. The color shading is the wind convergence. The contours are the virtual potential temperature (K). The blue surface on the x-axis is the ocean surface and the green surface on the x-axis is the land surface.

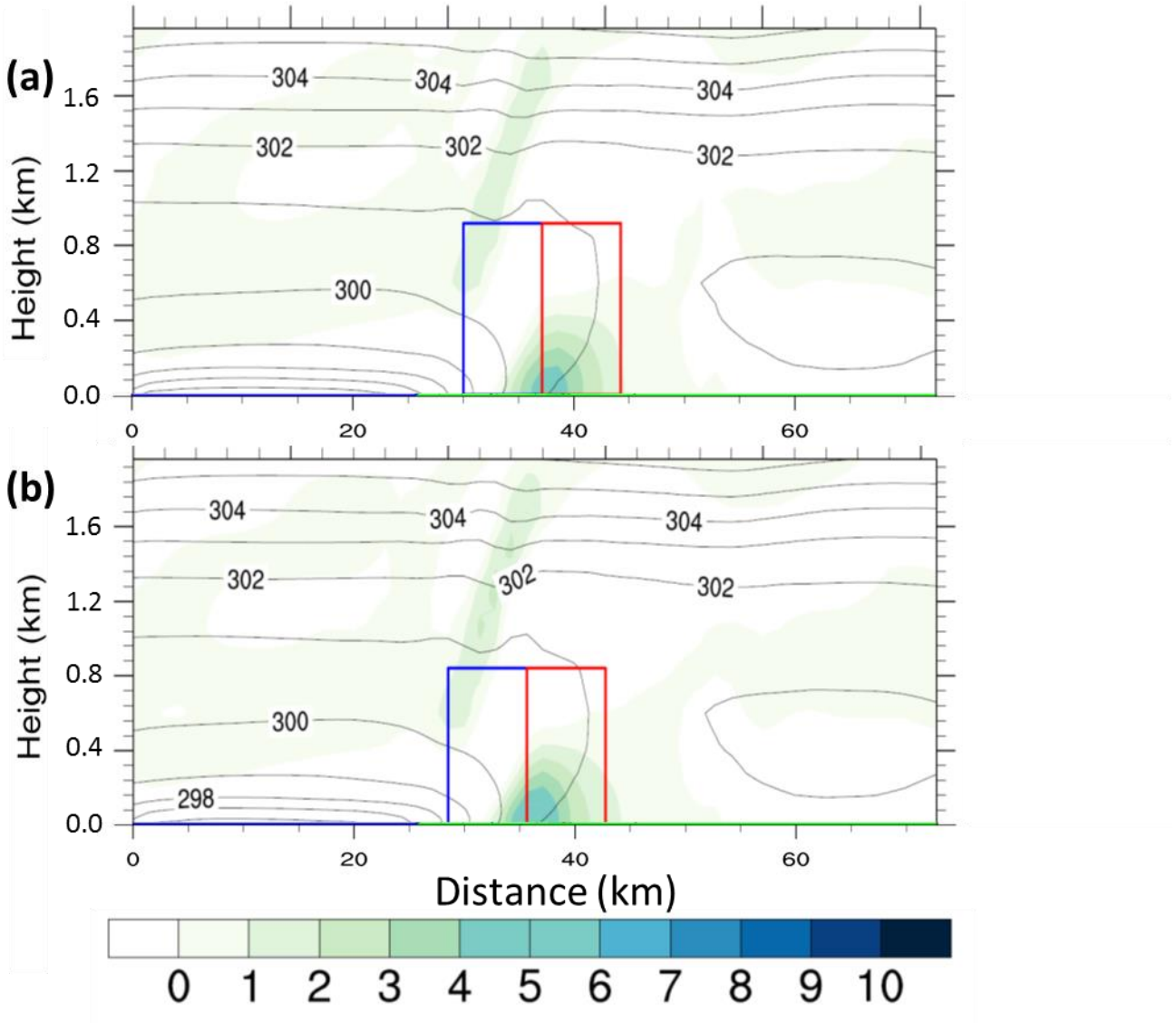

Figure 40. 21 August 2013 WLIS 1500 UTC. (a) Uniform run; (b) G1SST run. The virtual potential temperature (K) is contoured and the wind convergence (10^{-4} s^{-1}) is shaded. The blue outlined box denotes the sea breeze air averaging field and the red outlined box represents the ambient air averaging field used to calculate the theoretical sea breeze speed (eq. 5). Notice that the G1SST sea breeze box is in contact with more sea breeze air than the uniform sea breeze box. Location of WLIS is shown in figure 26a.

Table 12. 21 August 2013 ELIS, CLIS and ELIS numerical and theoretical sea breeze speed. The values in parenthesis are percent change from scenario 1 to scenario 2. Scenario 1 and 2 are specified in the text and Figure 39.

		Numerical sea breeze speed (m s^{-1})	Scenario 1		Scenario 2		Synoptic wind speed (m s^{-1})
			Theoretical sea breeze speed (m s^{-1})	Froude Number	Theoretical sea breeze speed (m s^{-1})	Froude Number	
ELIS	Uniform	1.64	7.34	0.22	5.22 (29%)	0.31 (41%)	1.05
	NARR	1.73	7.48	0.23	5.38 (28%)	0.32 (39%)	1.05
	G1SST	1.73	7.50	0.23	5.41 (28%)	0.32 (39%)	1.03
CLIS	Uniform	1.06	6.84	0.15	5.01 (27%)	0.21 (40%)	0.20
	NARR	1.06	6.78	0.16	5.00 (25%)	0.21 (40%)	0.09
	G1SST	1.16	6.72	0.17	4.98 (26%)	0.23 (35%)	0.09
WLIS	Uniform	1.45	5.91	0.25	4.52 (24%)	0.32 (28%)	0.84
	NARR	1.54	6.74	0.23	5.04 (25%)	0.31 (34%)	0.73
	G1SST	1.45	6.91	0.21	4.86 (30%)	0.30 (43%)	0.70

Table 13. 21 August 2013 1500 UTC (values in red) and 1700 UTC (values in black) surface temperature (˚C) for ELIS, CLIS and WLIS.

1500 UTC Temperature (˚C)		Ocean Surface		Land Surface		Land-ocean surface gradient	
ELIS	Uniform	22.0	22.0	36.2	37.8	14.2	15.8
	NARR	21.4	21.4	36.0	37.5	14.6	16.1
	G1SST	20.1	20.1	35.5	37.3	15.4	17.2
CLIS	Uniform	22.0	22.0	32.6	36.4	10.6	14.4
	NARR	22.0	22.0	32.8	36.4	10.8	14.4
	G1SST	22.6	22.6	33.1	36.5	10.5	13.9
WLIS	Uniform	22.0	22.0	36.4	38.8	14.4	16.8
	NARR	22.6	22.6	36.7	38.4	14.1	15.8
	G1SST	23.2	23.2	36.7	39.0	13.5	15.8
WLIS minus ELIS	Uniform	0.0	0.0				
	NARR	1.2	1.2				
	G1SST	3.1	3.1				

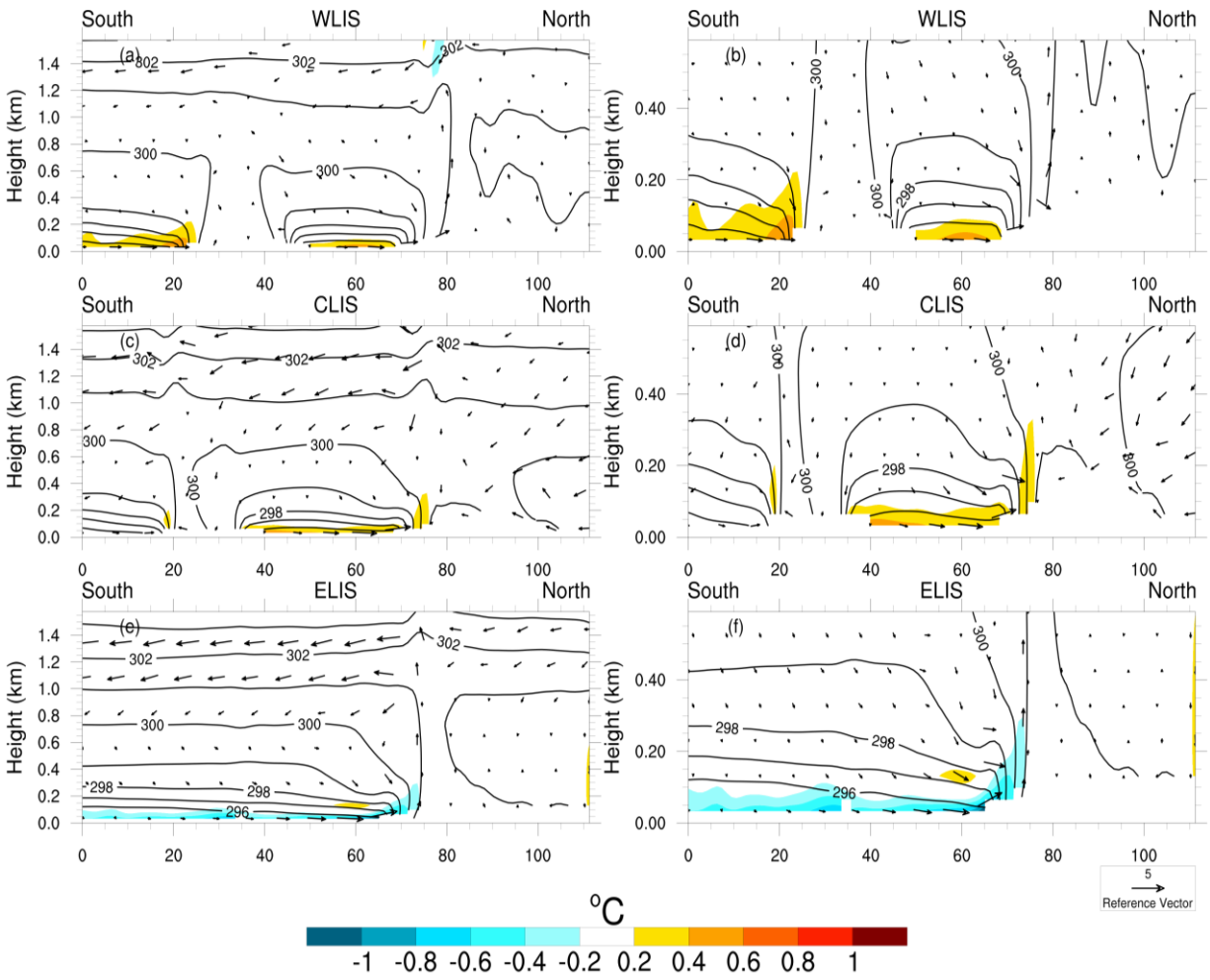

Figure 41. 21 August 2013 virtual potential temperature difference between G1SST and uniform (shaded), virtual potential temperature of uniform (contoured) and wind parallel to the plane of the cross section (vectors). (a,b) is WLIS, (c,d) is CLIS and (e,f) is ELIS. (a,c,e) are plotted to 1.6 km height and (b.d,f) are plotted to 0.6 km height. Location of WLIS, CLIS and ELIS are shown in figure 26a.

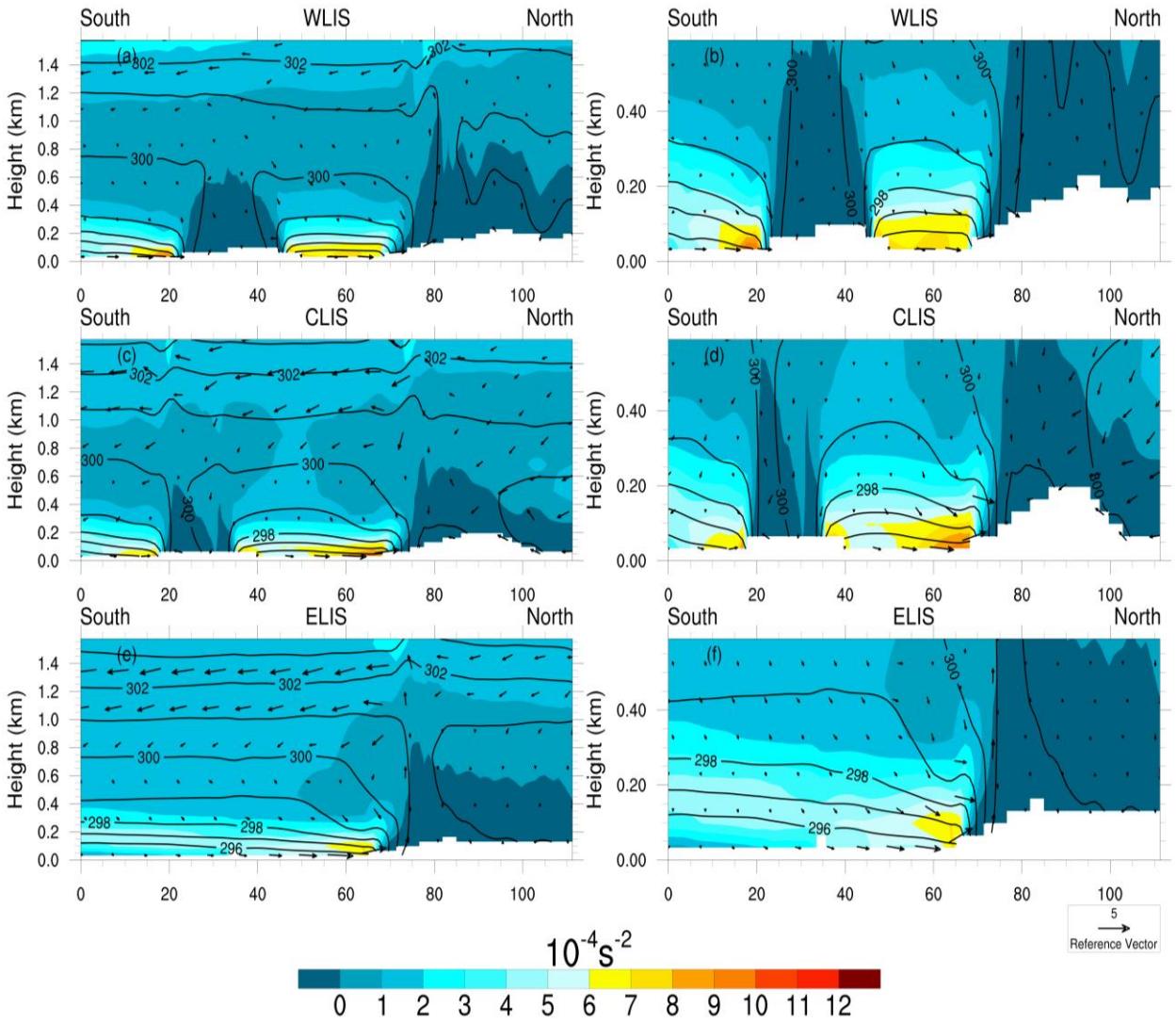

Figure 42. 21 August 2013 Uniform Vertical Cross Sections plotting buoyancy frequency (shaded; N^2; 10^{-4} s^{-2}), virtual potential temperature (contoured; K), wind parallel to the plane of the cross section (vectors; m s^{-1}). (a-b) WLIS; (c-d) is CLIS and (e-f) is ELIS. The location of WLIS, CLIS and ELIS is shown in Figure 26a. (b,d,f) zoom to the lowest 0.6 km of the atmosphere.

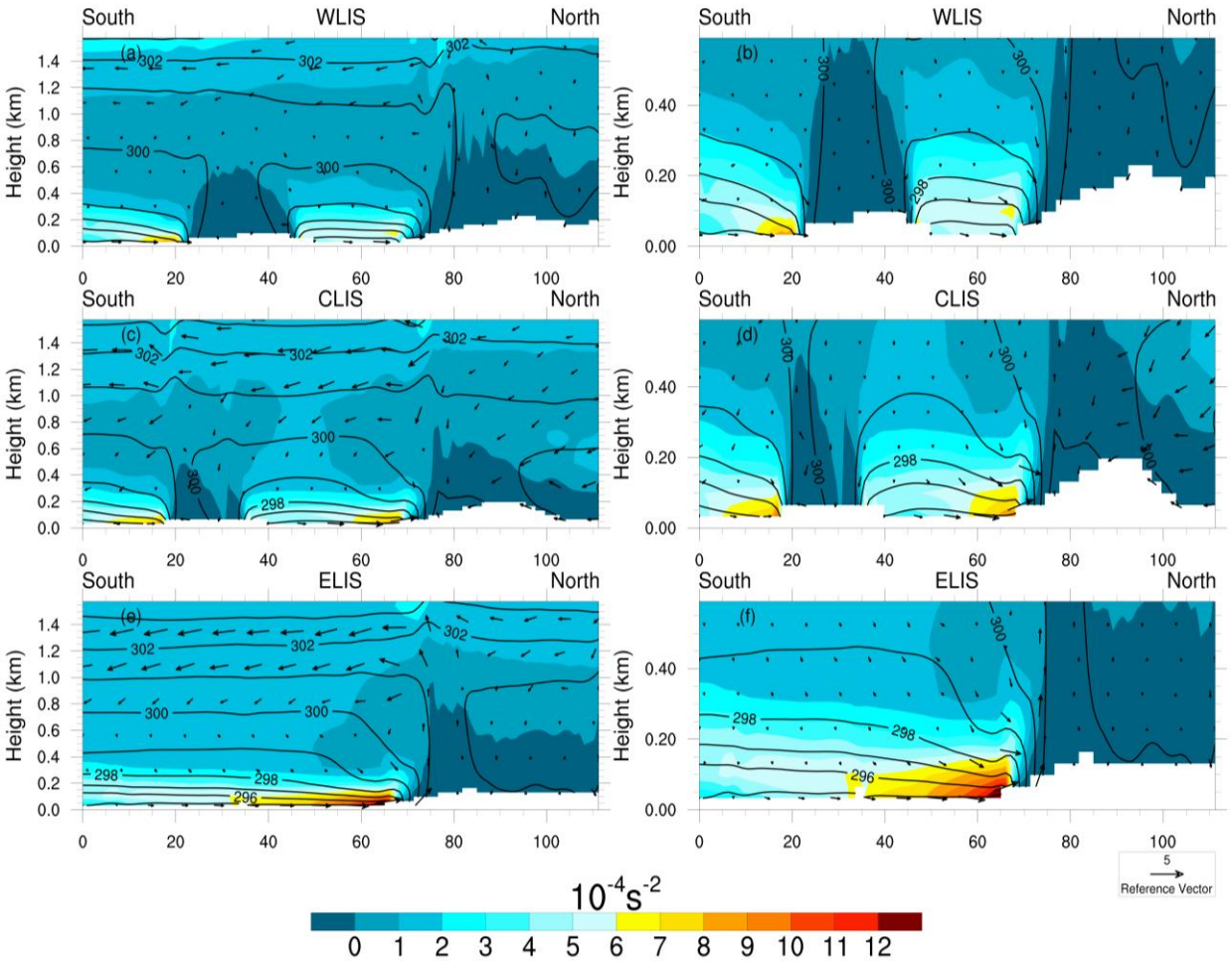

Figure 43. 21 August 2013 G1SST Vertical Cross Sections plotting buoyancy frequency (shaded; N^2; 10^{-4} s^{-2}), virtual potential temperature (contoured; K), wind parallel to the plane of the cross section (vectors; m s^{-1}). (a-b) WLIS; (c-d) is CLIS and (e-f) is ELIS. The location of WLIS, CLIS and ELIS is shown in Figure 26a. (b,d,f) zoom to the lowest 0.6 km of the atmosphere.

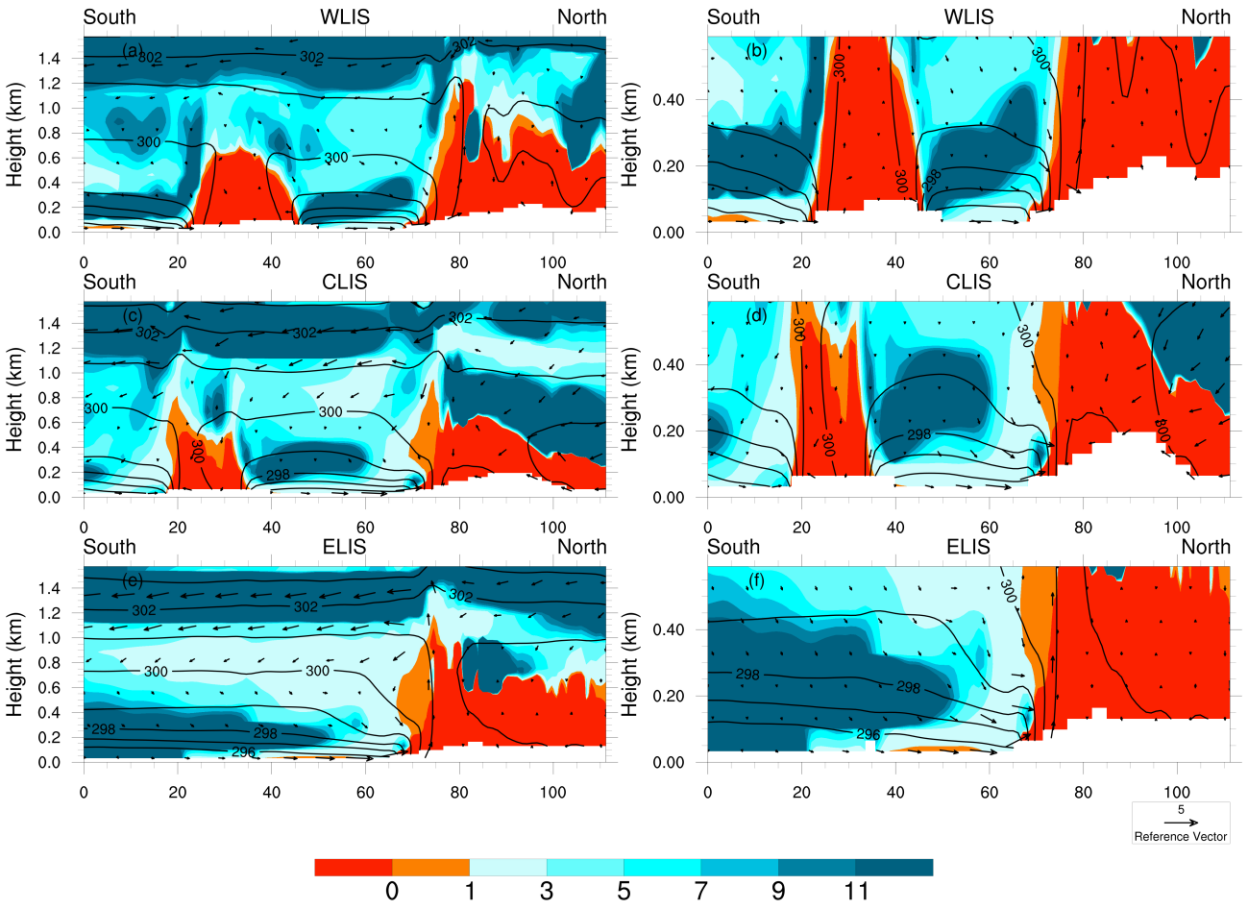

Figure 44. 21 August 2013 Uniform Vertical Cross Sections plotting gradient Richardson number (shaded; Ri; unitless), virtual potential temperature (contoured; K), wind parallel to the plane of the cross section (vectors; m s^{-1}). (a-b) WLIS; (c-d) is CLIS and (e-f) is ELIS. The location of WLIS, CLIS and ELIS is shown in Figure 26a. (b,d,f) zoom to the lowest 0.6 km of the atmosphere.

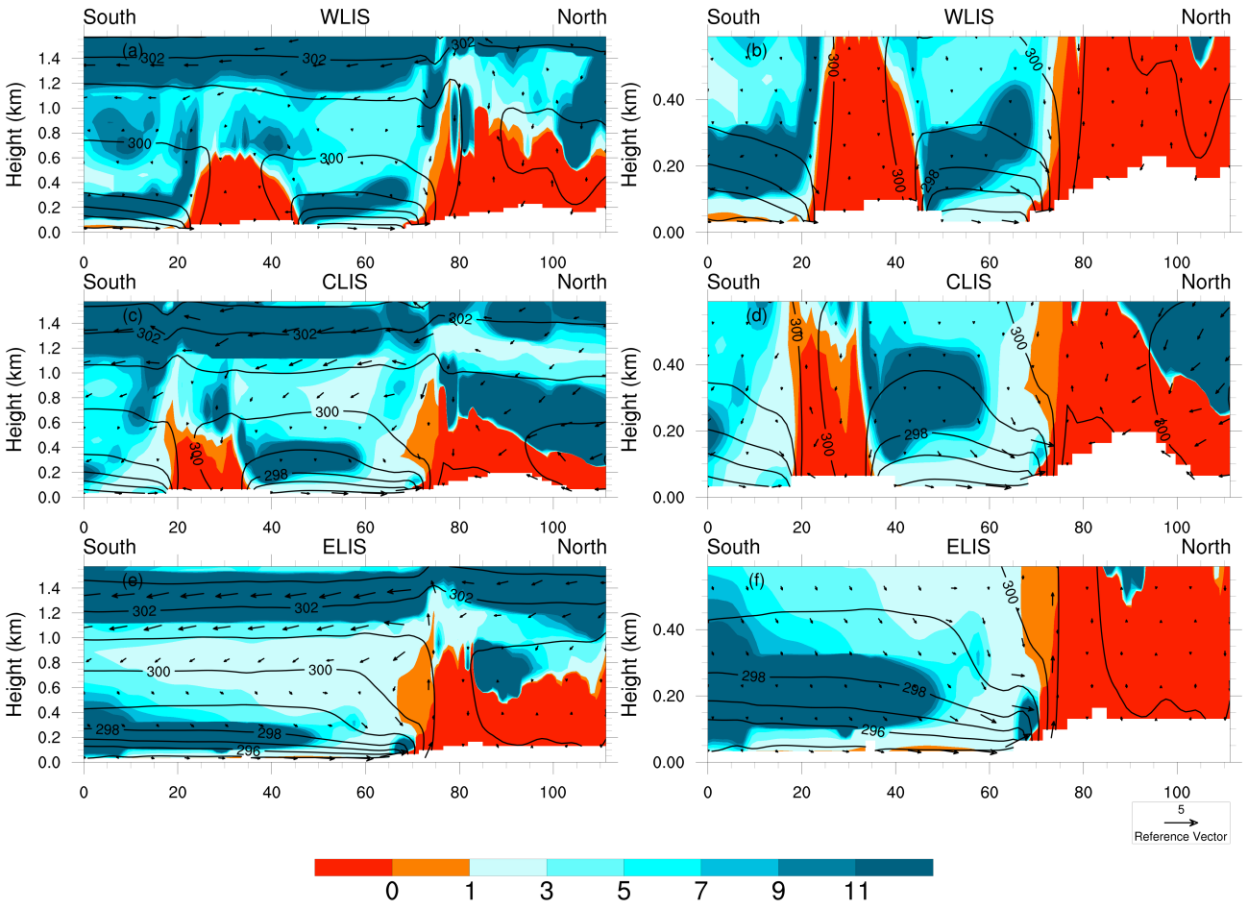

Figure 45. 21 August 2013 G1SST Vertical Cross Sections plotting gradient Richardson number (shaded; Ri; unitless), virtual potential temperature (contoured; K), wind parallel to the plane of the cross section (vectors; m s^{-1}). (a-b) WLIS; (c-d) is CLIS and (e-f) is ELIS. The location of WLIS, CLIS and ELIS is shown in Figure 26a. (b,d,f) zoom to the lowest 0.6 km of the atmosphere.

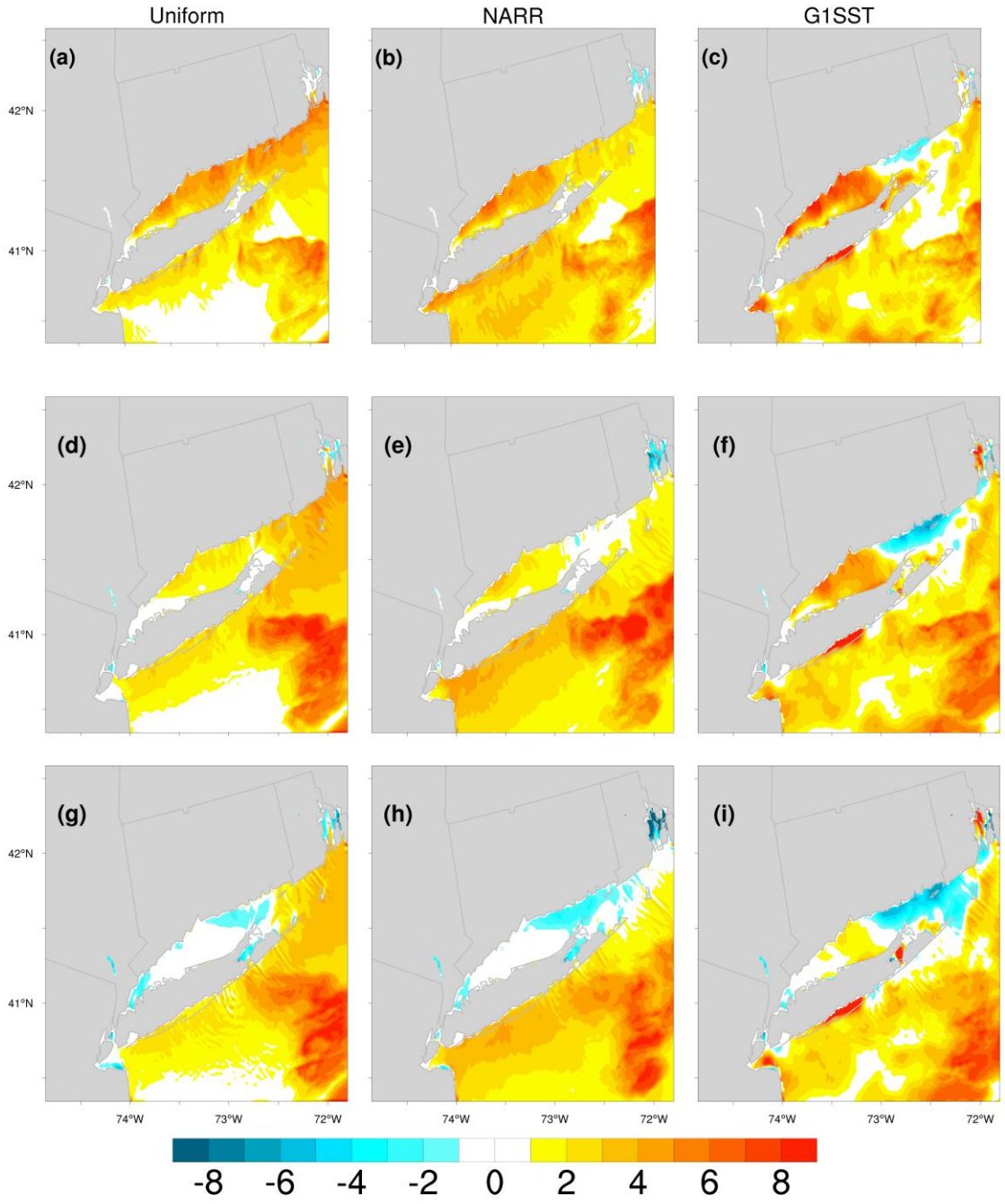

Figure 46. 21 August 2013 Surface buoyancy flux (W m^{-2}) for (a,d,g) uniform, (b,e,h) NARR, and (c,f,i) G1SST where (a-c) is 1500 UTC, (d-f) 1600 UTC and (g-i) 1700 UTC.

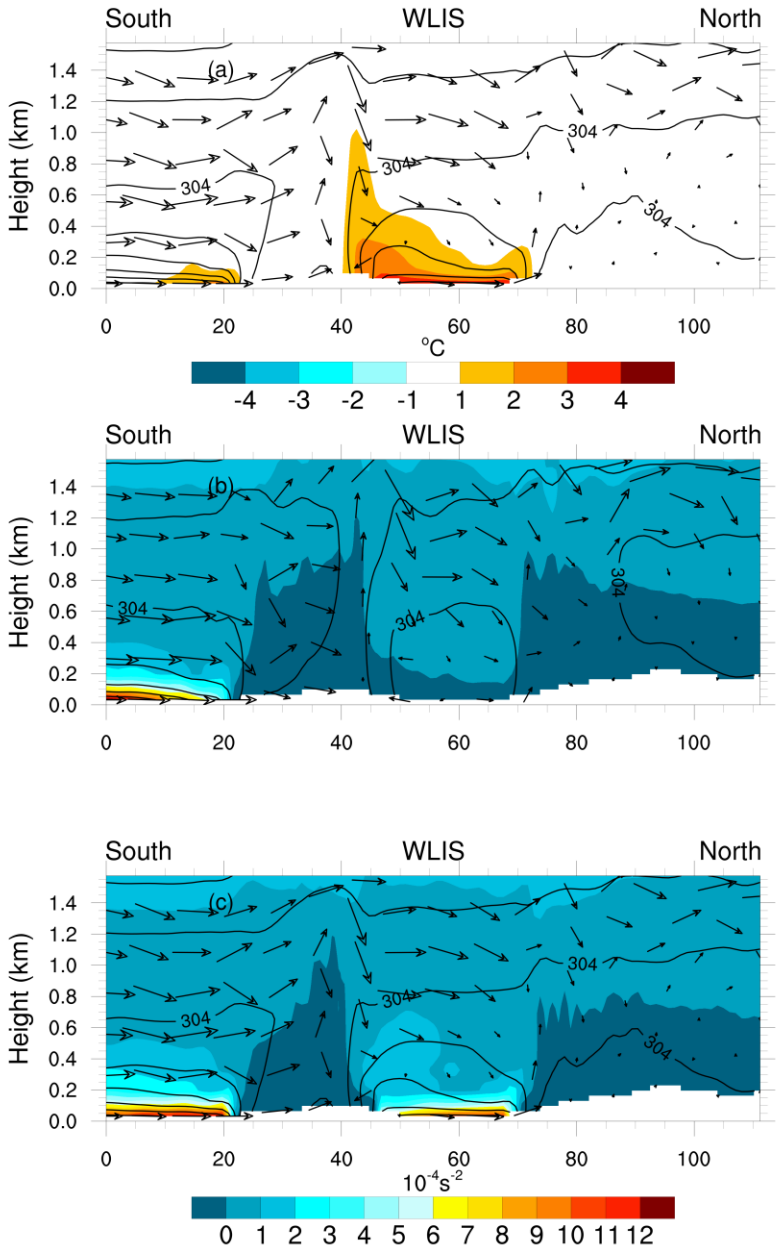

Figure 47. 08 July 2013 WLIS Vertical Cross Sections. (a) *OrigCoast_day* minus *HRCoast_day* virtual potential temperate (shaded; K), *HRCoast_day* virtual potential temperature (contoured; K) and *HRCoast_day* wind parallel to the plane of the cross section (vectors; m s^{-1}); (b) *OrigCoast_day* buoyancy frequency ($N^{2;}$ 10^{-4} s^{-2}; shaded) with *OrigCoast_day* virtual potential temperature (contoured; K) and *OrigCoast_day* wind parallel to the plane of the cross section (vectors; m s^{-1}); (c) plots the same variables as (b) except for *HRCoast_day*. Location of WLIS is shown in figure 26a.

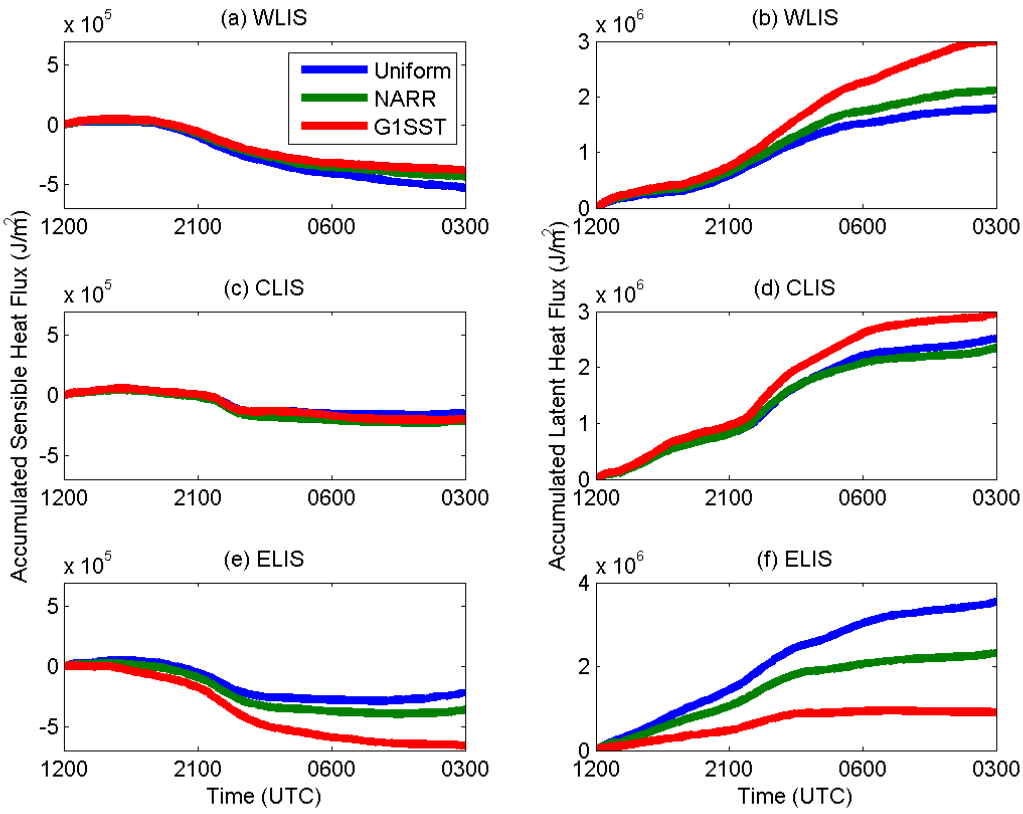

Figure 48. 21-22 August 2013 accumulated surface heat flux. (a,c,e) sensible heat flux; (a) WLIS, (c) CLIS, (e) ELIS. (b,d,f) latent heat flux; (b) WLIS, (d) CLIS, (f) ELIS.

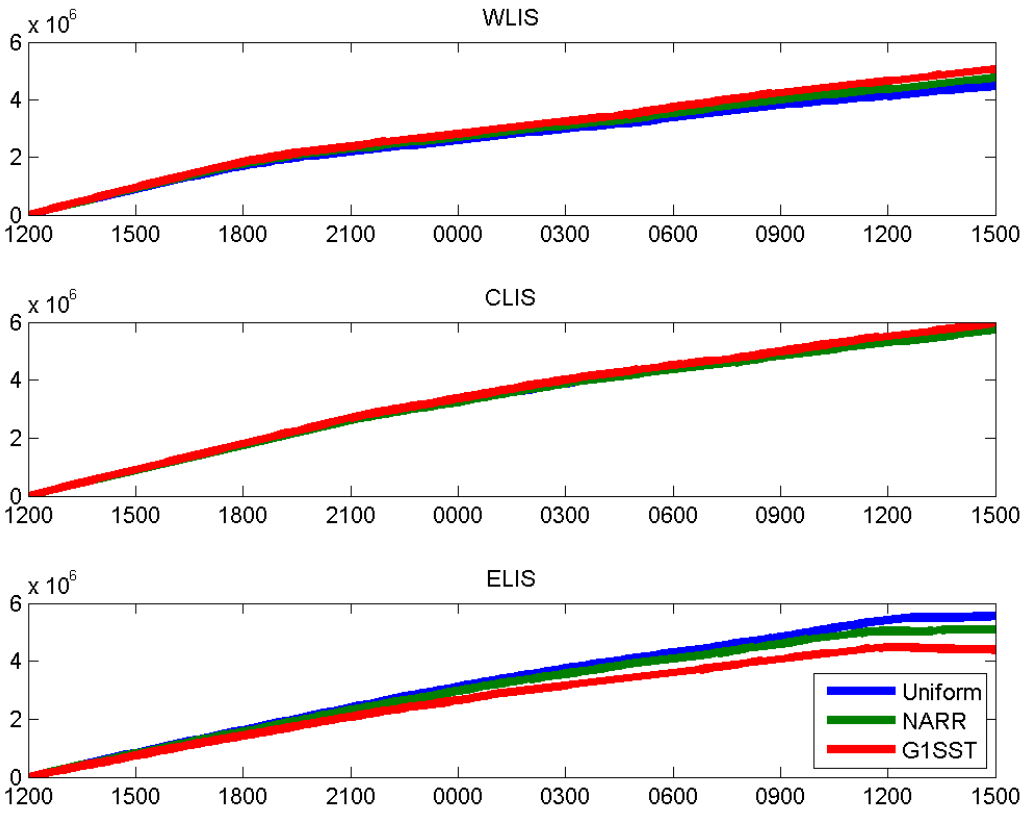

Figure 49. 21-22 August 2013 accumulated net longwave radiation (J m^{-2}) versus time (UTC). (a) WLIS, (b) CLIS, (c) ELIS.

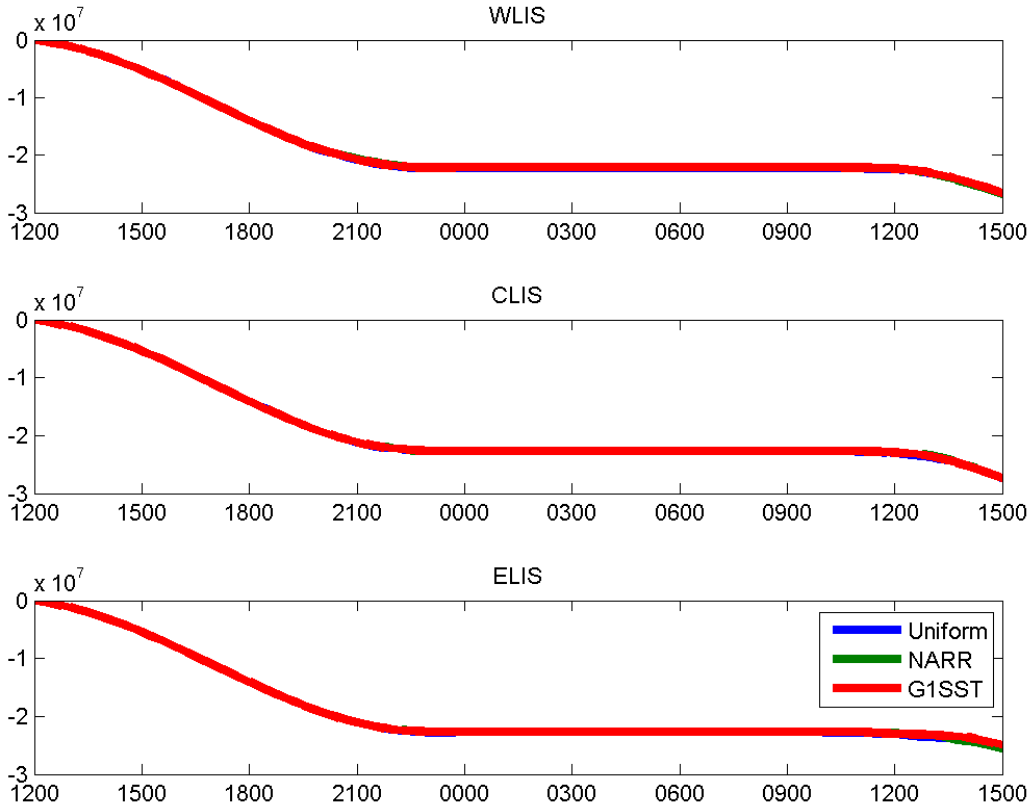

Figure 50. 21-22 August 2013 accumulated net surface heat flux (J m^{-2}) versus time (UTC). (a) WLIS, (b) CLIS, (c) ELIS.

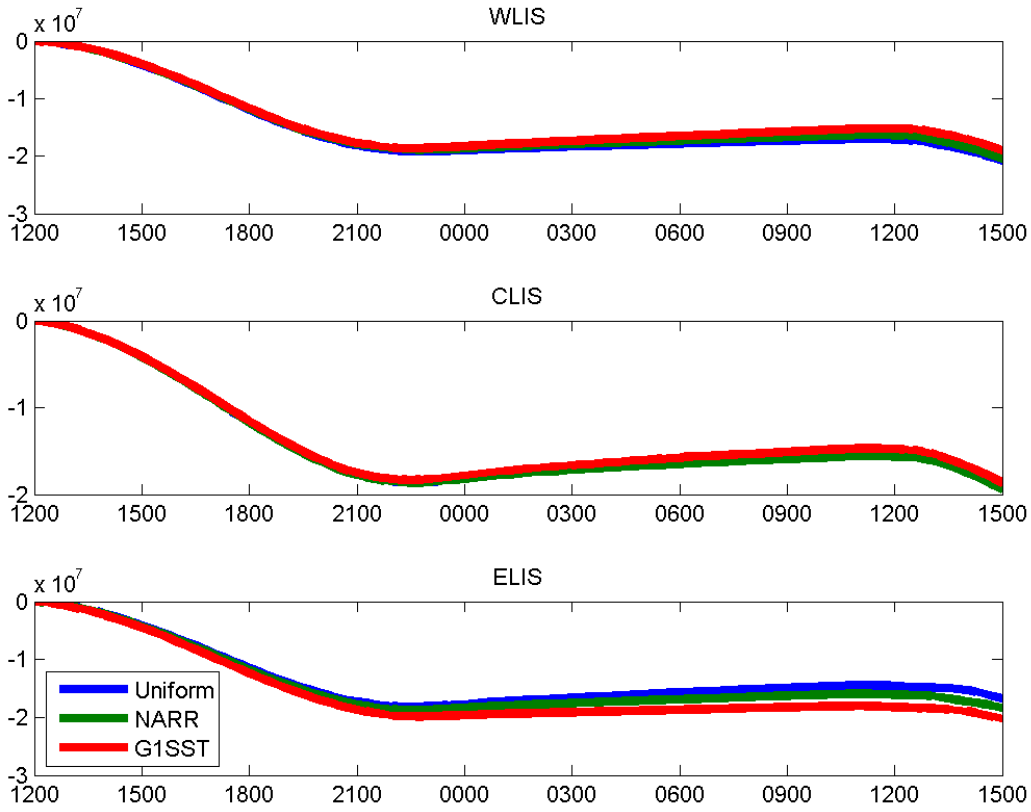

Figure 51. 21-22 August 2013 accumulated net surface heat flux (J m^{-2}) versus time (UTC). (a) WLIS, (b) CLIS, (c) ELIS.

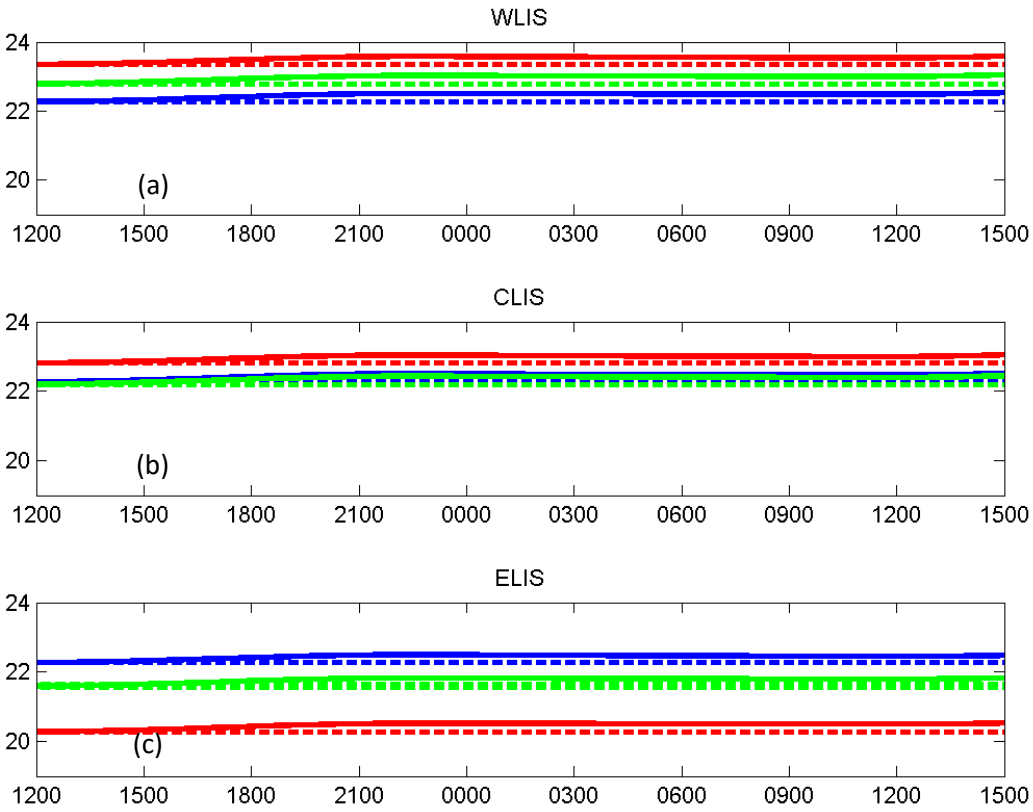

Figure 52. 21-22 August 2013 sea temperature (˚C) versus time (UTC). (a) WLIS, (b) CLIS, (c) ELIS. Blue lines represent uniform, green lines represent NARR, and red lines represent G1SST. Dashed lines represent model sea temperature and solid lines represent theoretical sea temperature (eq. 10).

Table 14. 21 August 2013 ELIS, CLIS and WLIS RMSE between static model SST and theoretical dynamic SST over 27 hours (˚C).

	Uniform	NARR	G1SST
ELIS	0.0320	0.0362	0.0430
CLIS	0.0348	0.0353	0.0329
WLIS	0.0398	0.0378	0.0350

References

Arakawa, A., & Lamb, V. R. (1977). Computational design of the basic dynamical processes of the UCLA general circulation model. *Methods in computational physics*, *17*, 173-265.

Berri, G. J., & Paegle, J. (1990). Sensitivity of local predictions to initial conditions. *Journal of Applied Meteorology*, *29*(3), 256-267.

Blumberg, A. F., & Pritchard, D. W. (1997). Estimates of the transport through the East River, New York. *Oceanographic Literature Review*, *44*(11), 1225-1225.

Bowman, M. J., & Esaias, W. E. (1981). Fronts, stratification, and mixing in Long Island and Block Island sounds. *Journal of Geophysical Research: Oceans (1978–2012)*, *86*(C5), 4260-4264.

Carbone, R. E., Wilson, J. W., Keenan, T. D., & Hacker, J. M. (2000). Tropical island convection in the absence of significant topography. Part I: Life cycle of diurnally forced convection. *Monthly weather review*, *128*(10), 3459-3480.

Chao, Y., Li, Z., Farrara, J. D., & Hung, P. (2009). Blending sea surface temperatures from multiple satellites and in situ observations for coastal oceans. *Journal of Atmospheric and Oceanic Technology*, *26*(7), 1415-1426.

Codiga, D. L., & Rear, L. V. (2004). Observed tidal currents outside Block Island Sound: Offshore decay and effects of estuarine outflow. *Journal of Geophysical Research: Oceans*, *109*(C7).

Colby Jr, F. P. (2004). Simulation of the New England sea breeze: The effect of grid spacing. *Weather and forecasting*, *19*(2), 277-285.

Colle, B. A., Olson, J. B., & Tongue, J. S. (2003). Multiseason verification of the MM5. Part I: Comparison with the Eta model over the central and eastern United States and impact of MM5 resolution. *Weather and Forecasting*,*18*(3), 431-457.

Crosman, E. T., & Horel, J. D. (2010). Sea and lake breezes: a review of numerical studies. *Boundary-layer meteorology*, *137*(1), 1-29.

Cutnell, J. D., & Johnson, K. W. (2009). *Physics*. Hoboken, NJ: Wiley

Done, J., Davis, C. A., & Weisman, M. (2004). The next generation of NWP: Explicit forecasts of convection using the Weather Research and Forecasting (WRF) model. *Atmospheric Science Letters*, *5*(6), 110-117.

Ek, M. B., Mitchell, K. E., Lin, Y., Rogers, E., Grunmann, P., Koren, V., ... & Tarpley, J. D. (2003). Implementation of Noah land surface model advances in the National Centers for Environmental Prediction operational mesoscale Eta model. *Journal of Geophysical Research: Atmospheres (1984–2012)*, *108*(D22).

Fribance, D. B., O'Donnell, J., & Houk, A. (2013). Residual circulation in western Long Island Sound. *Journal of Geophysical Research: Oceans*,*118*(9), 4727-4745.

Geyer, W. R. (1997). Influence of wind on dynamics and flushing of shallow estuaries. *Estuarine, Coastal and Shelf Science*, *44*(6), 713-722.

Haurwitz, B. (1947). Comments on the sea-breeze circulation. *Journal of Meteorology*, *4*(1), 1-8.

Holton, J. R., & Hakim, G. J. (2012). *An Introduction to Dynamic Meteorology* (Vol. 88). Academic press.

Hong, S. Y., Noh, Y., & Dudhia, J. (2006). A new vertical diffusion package with an explicit treatment of entrainment processes. *Monthly Weather Review*, *134*(9), 2318-2341.

Janjic, Z. I. (1994). The step-mountain eta coordinate model: Further developments of the convection, viscous sublayer, and turbulence closure schemes. *Monthly Weather Review*, *122*(5), 927-945.

Jiménez, P. A., Dudhia, J., González-Rouco, J. F., Navarro, J., Montávez, J. P., & García-Bustamante, E. (2012). A revised scheme for the WRF surface layer formulation. *Monthly Weather Review*, *140*(3), 898-918.

Kain, J. S., & Fritsch, J. M. (1990). A one-dimensional entraining/detraining plume model and its application in convective parameterization. *Journal of the Atmospheric Sciences*, *47*(23), 2784-2802.

Kain, J. S. (2004). The Kain-Fritsch convective parameterization: an update. *Journal of Applied Meteorology*, *43*(1), 170-181.

Kingsmill, D. E. (1995). Convection initiation associated with a sea-breeze front, a gust front, and their collision. *Monthly weather review*, *123*(10), 2913-2933.

Klemp, J. B., Skamarock, W. C., & Dudhia, J. (2007). Conservative split-explicit time integration methods for the compressible nonhydrostatic equations. *Monthly Weather Review*, *135*(8), 2897-2913.

Krogsæter, O., Reuder, J., & Hauge, G. (2011). WRF and the marine planetary boundary layer. In *12th Annual WRF users workshop*.

LaCasse, K. M., Splitt, M. E., Lazarus, S. M., & Lapenta, W. M. (2008). The impact of high-resolution sea surface temperatures on the simulated nocturnal Florida marine boundary layer. *Monthly Weather Review*, *136*(4), 1349-1372.

Laprise, R. (1992). The Euler equations of motion with hydrostatic pressure as an independent variable. *Monthly weather review*, *120*(1), 197-207.

Latimer, J. S., Tedesco, M. A., Swanson, R. L., Yarish, C., Stacey, P. E., & Garza, C. (Eds.). (2013). *Long Island sound: prospects for the urban sea*. Springer Science & Business Media.

Lazarus, S. M., Calvert, C. G., Splitt, M. E., Santos, P., Sharp, D. W., Blottman, P. F., & Spratt, S. M. (2007). Real-time, high-resolution, space-time analysis of sea surface temperatures from multiple platforms. *Monthly Weather Review*, *135*(9), 3158-3173.

Liu, G., Liu, Y., & Endo, S. (2013). Evaluation of surface flux parameterizations with long-term ARM observations. *Monthly Weather Review*, *141*(2), 773-797.

Lombardo, K., Sinsky, E., Jia, Y., Whitney, M. M., & Edson, J. (2016). Sensitivity of Simulated Sea Breezes to Initial Conditions in Complex Coastal Regions. *Monthly Weather Review*, 144(4).

Martin, J. E. (2013). *Mid-latitude atmospheric dynamics: a first course*. John Wiley & Sons.

Mass, C. F., Ovens, D., Westrick, K., & Colle, B. A. (2002). Does increasing horizontal resolution produce more skillful forecasts? *Bulletin of the American Meteorological Society*, *83*(3), 407-430.

Mesinger, F., DiMego, G., Kalnay, E., Mitchell, K., Shafran, P. C., Ebisuzaki, W., ... & Ek, M. B. (2006). North American regional reanalysis. *Bulletin of the American Meteorological Society*, *87*(3), 343-360.

Monin, A. S., & Obukhov, A. (1954). Basic laws of turbulent mixing in the surface layer of the atmosphere. *Contrib. Geophys. Inst. Acad. Sci. USSR*,*151*, 163-187.

Miller, S. T. K., Keim, B. D., Talbot, R. W., & Mao, H. (2003). Sea breeze: Structure, forecasting, and impacts. *Reviews of geophysics*, *41*(3).

Morrison, H., G. Thompson, V. Tatarskii. (2009). Impact of Cloud Microphysics on the Development of Trailing Stratiform Precipitation in a Simulated Squall Line: Comparison of One– and Two–Moment Schemes.*Mon. Wea. Rev.*, **137**, 991–1007.

Nakanishi, M., & Niino, H. (2006). An improved Mellor–Yamada level-3 model: Its numerical stability and application to a regional prediction of advection fog. *Boundary-Layer Meteorology*, *119*(2), 397-407.

Nakanishi, M., & Niino, H. (2009). Development of an improved turbulence closure model for the atmospheric boundary layer. *J. Meteor. Soc. Japan*, **87**, 895–912.

Novak, D. R., & Colle, B. A. (2006). Observations of multiple sea breeze boundaries during an unseasonably warm day in metropolitan New York City. *Bulletin of the American Meteorological Society*, *87*(2), 169-174.

Orton, P. M., McGillis, W. R., & Zappa, C. J. (2010). Sea breeze forcing of estuary turbulence and air-water CO2 exchange. *Geophysical Research Letters*, *37*(13).

Ries, H., & Schlünzen, K. H. (2009). Evaluation of a mesoscale model with different surface parameterizations and vertical resolutions for the Bay of Valencia. *Monthly Weather Review*, *137*(8), 2646-2661.

Robinson, F. J., Patterson, M. D., & Sherwood, S. C. (2013). A Numerical Modeling Study of the Propagation of Idealized Sea-Breeze Density Currents*. *Journal of the Atmospheric Sciences*, *70*(2), 653-668.

Rouault, M., White, S. A., Reason, C. J. C., Lutjeharms, J. R. E., & Jobard, I. (2002). Ocean-atmosphere interaction in the Agulhas Current region and a South African extreme weather event. *Weather and Forecasting*, *17*(4), 655-669.

Simpson, J. E. (1994). *Sea breeze and local winds*. Cambridge University Press.

Simpson, J. H., & Sharples, J. (2012). *Introduction to the Physical and Biological Oceanography of Shelf Seas*. Cambridge University Press.

Skamarock, W. C., Klemp, J. B., Dudhia, J., Gill, D. O., Barker, D. M., Wang, W., & Powers, J. G. (2008). *A description of the advanced research WRF version 3*. National Center for Atmospheric Research Boulder Co Mesoscale and Microscale Meteorology Div.

Stewart, R. H. (2008). *Introduction to Physical Oceanography*. Texas: Texas A & M University.

Stull, R. B. (1988). *An Introduction to Boundary Layer Meteorology*. Kluwer Academic Publishers.

Steele, C. J., Dorling, S. R., Von Glasow, R., & Bacon, J. (2013). Idealized WRF model sensitivity simulations of sea breeze types and their effects on offshore windfields. *Atmos. Chem. Phys*, *13*, 443-461.

Tong, D., Lee, P., Ngan, F., & Pan, L. (2013). Investigation of surface layer parameterization of the WRF model and its impact on the observed nocturnal wind speed bias: Period of investigation focuses on the Second Texas Air Quality Study (TexAQS II) in 2006.

Ullman, D. S., & Codiga, D. L. (2004). Seasonal variation of a coastal jet in the Long Island Sound outflow region based on HF radar and Doppler current observations. *Journal of Geophysical Research: Oceans*, *109*(C7).

Weisman, M. L., Skamarock, W. C., & Klemp, J. B. (1997). The resolution dependence of explicitly modeled convective systems. *Monthly Weather Review*, *125*(4), 527-548.

Whitney, M. M., & Garvine, R. W. (2008). Estimating tidal current amplitudes outside estuaries and characterizing the zone of estuarine tidal influence. *Continental Shelf Research*, *28*(3), 380-390.

Wicker, L. J., & Skamarock, W. C. (2002). Time-splitting methods for elastic models using forward time schemes. *Monthly Weather Review*, *130*(8), 2088-2097.

Wilson, R. E. (1976), Gravitational circulation in Long Island Sound, *Estuarine Coastal Mar. Sci.*, **4**, 443–453.

Yang, Y., Chen, Y. L., & Fujioka, F. M. (2005). Numerical simulations of the island-induced circulations over the island of Hawaii during HaRP. *Monthly weather review*, *133*(12), 3693-3713.

Zhang, Y., Chen, Y. L., Schroeder, T. A., & Kodama, K. (2005). Numerical Simulations of Sea-Breeze Circulations over Northwest Hawaii. *Weather and forecasting*, *20*(6), 827-846.